Novel Methods for Analyzing Problematic Geodetic Data: Applications to Coseismic Slip Modeling and Surface Deformation Mapping

by

Eric D. Szymanski

A dissertation submitted in partial fulfillment
of the requirements for the degree of
Doctor of Philosophy
(Earth and Environmental Sciences)
in the University of Michigan
2025

Doctoral Committee:

Associate Professor Eric Hetland, Chair
Associate Professor Yihe Huang
Associate Professor Raj Rao Nadakuditi
Professor Nathan Niemi

Eric D. Szymanski
szymaner@umich.edu
ORCID iD: 0009-0008-8971-1437

© Eric D. Szymanski 2025

DEDICATION

"*Live as if you were to die tomorrow. Learn as if you were to live forever.*" - Mahatma Gandhi

For my wife, Elisha, and our two sons Asa and Leif: you are my guiding light.

ACKNOWLEDGEMENTS

I would like to express my deepest gratitude to my advisor, Eric Hetland, without his guidance, mentorship, and support this body of work would not have been possible. I would be remiss if I did not also mention his patience with my constant exploration, which resulted in many false starts and a collection of unfinished work. His understanding during my personal struggles here has truly made a lasting impression on me. I would also like to thank my committee members, Nathan Niemi, Yihe Huang, and Raj Nadakuditi, for providing their time and support throughout this process. My one regret is not taking more advantage of your knowledge while it was available to me. I am also indebted to the phenomenal administrative staff of the Department of Earth and Environmental Sciences, including Nathan Sadowsky, Anne Hudon, Paula Frank, Chrissy Zigulis, Nico Spraggins, Carla Huhn, Courtney Hooper, and Craig Delap. I should also highlight the essential funding I received from the Rackham Merit Fellowship and the National Defense Science and Engineering Fellowship through the University of Michigan and the Army Research Office, which was crucial for completing this dissertation.

I am deeply grateful to my friends, family, and faculty members at both North Carolina State University and the University of Michigan for their invaluable support and inspiration. I especially want to thank Del Bohnenstiehl for bringing me on as a research assistant while I was still taking classes at Wake Technical Community College, igniting my passion for geophysics. Alongside Del, the mentorship of Karl Wegman and Ron Fodor provided crucial guidance, helping me build the ambition and confidence to pursue graduate school. I was fortunate to continue collaborating with Karl and to forge new relationships with Paula Figueiredo and others while working on the Sparta, North Carolina earthquake. This project ultimately became the first chapter of my dissertation and significantly shaped my research interests. Conversations with my brother, Luke Szymanski, sparked insights that formed the foundation for the material in Chapter 4 of this dissertation. I was also blessed with many friendships, both in and outside that department. Fellow graduate students, Billy Medwedeff, Madelyn Cook, Sarah Katz, Olivia Walbert, Prithvi Thakur, Madeline Hille, Sam Haughland, and many others provided endless sources of stimulating conversation and support in areas ranging from everyday life to academics. Other friends around Ann Arbor, Adam and

Cynthia Wellman, Calum McNamara, Maria Rosala, Buddy and Michelle Naber, Taylor and Sammy Brost, Jason Lerch, and many more helped me maintain my sanity throughout my time in the program. Finally, I am deeply grateful to my wife, Elisha Szymanski, without whom none of this would have been possible. My two sons, Asa and Leif, always helped me keep things in perspective and brought joy to my life, even during challenging times. I also want to thank my wonderful parents, Lisa Wolf and Chris Szymanski, who nurtured my curiosity from a young age and continue to offer unwavering love and support.

TABLE OF CONTENTS

DEDICATION ii

ACKNOWLEDGEMENTS iii

LIST OF FIGURES vii

LIST OF TABLES xiv

LIST OF APPENDICES xv

ABSTRACT xvi

CHAPTER

1 Introduction 1

1.1 Historical Context 1
1.2 Extending Our Reach 3
1.3 Estimation method for coseismic slip models (Chapters 2 and 3) 6
1.4 Geodetic Data Fusion (Chapter 4) 7

2 Imaging Left-Lateral and Reverse Near-Surface Slip of the 2020 M5.1 Sparta, North Carolina, Earthquake 8

2.1 Introduction 9
2.2 Data 12
2.2.1 Impacts of the built environment on the interferograms 15
2.2.2 LiDAR 15
2.3 Inverse Methods 17
2.4 Results 20
2.5 Discussion 22
2.5.1 Preferred model 22
2.5.2 Comparison to coseismic model model of Wicks and Chiu (2022) . . 25
2.5.3 Consistency of coseismic slip model with tectonic stress 26
2.6 Conclusions 28
2.7 Data and Resources 28
2.8 Acknowledgements 29

3 Revisiting the 2010 Jiashian and 2016 MeiNong Earthquakes in Taiwan: Geodetic Evidence for Shared Westerly Dipping Thrust Fault 30

3.1 Introduction . . . 31
3.2 Integrated estimation of coseismic slip models . . . 35
3.3 Results . . . 42
3.3.1 Initial uniform slip search . . . 42
3.3.2 Integrated search: fault geometries . . . 42
3.3.3 Integrated search: best fit models . . . 45
3.4 Discussion . . . 48
3.4.1 Geodetic support of a shallower, more north striking, and largely thrust MeiNong coseismic model . . . 51
3.4.2 Connecting the 2010 Jiashian and 2016 MeiNong earthquakes . . . 54
3.5 Conclusions . . . 56

4 Geodetic Data Fusion using Multi-Output Gaussian Processes . . . 58

4.1 Introduction . . . 58
4.2 Fusion Architecture . . . 62
4.2.1 Gaussian processes regression . . . 64
4.2.2 Construction of the prior covariance . . . 67
4.2.3 Construction of the observational covariance . . . 70
4.3 Demonstrations . . . 70
4.3.1 Coseismic deformation of the 2016 Meinong earthquake . . . 71
4.3.2 Coseismic deformation of the 2020 Sparta earthquake . . . 74
4.4 Discussion . . . 78
4.4.1 Impact of Gentoo on signal clarity . . . 78
4.4.2 Extensions and thoughts . . . 79
4.4.3 Covariance models . . . 79
4.4.4 scalability of the Gaussian process regression-based fusion . . . 80
4.5 Conclusions . . . 81

5 Conclusions . . . 82

5.1 Evaluation of Contributions . . . 82
5.1.1 Estimation Method for Coseismic Slip Modeling . . . 82
5.1.2 Geodetic Data Fusion . . . 84
5.2 Future Work . . . 85

APPENDICES . . . 86

BIBLIOGRAPHY . . . 115

LIST OF FIGURES

FIGURE

1.1 A simplified graphical representation of the interconnection between theory, observation, mathematical modeling, and how they are utilized in conjunction with estimation methods to produce scientific results for geophysical and geodetic studies. The red dashed box indicates areas in this work flow that this dissertation provides contributions. 5

2.1 Map showing earthquake epicenters from 1970–2023 (see Data and Resources), along with the double-couple focal mechanisms of the 2011 Mineral, VA (USGS; blue star indicates the hypocenter), and 2020 Sparta, NC (Saint Louis University Earthquake Center; black star), earthquakes. Ellipses indicate the approximate locations of seismic zones: Middleton Place-Summerville Seismic Zone (MPSSZ), the Eastern Tennessee Seismic Zone (ETSZ), the Giles Creek Seismic Zone (GCSZ), and the Central Virginia Seismic Zone (CVSZ). 10

2.2 ALOS-2 (A) and S-1 (D) interferograms, and LiDAR ICP X (G), Y (J), and Z (M) components. Panel (A) and (B) contain a cross indicating the centroid, blue polygons outlining prominent industrial parks in the interferogram footprint, and line indicating the field mapped surface rupture (A) (Figueiredo *et al.*, 2022) or a black rectangle indicating the surface projection of the modeled fault edges (B). Black arrows indicate the satellite azimuth and red arrow indicates the average look vector, with number indicating the average look angle from vertical. Synthetic interferograms for ALOS-2 (B) and S-1 (E), and LiDAR components X (H), Y (K), and Z (N), and the residuals (C), (F), (L), (I), and (O) respectively. The colorbar in panel (A) is common to all images. 14

2.3 Slip distributions for CSM-S1 (A), CSM-FULL (B), CSM-DAR (C), CSM-LiDAR (D) and CSM-JOINT (E), with black arrows indicating the slip vector on each subfault, and colors indicating the magnitude of slip. The color bar and along-strike distance is common to all panels. 21

2.4 (A) The Saint Louis University focal mechanisms (P quadrant shaded light purple and nodal planes depicted with blue lines), with the nodal planes associated with our preferred coseismic slip model CSM-JOINT (cyan lines, thin gray lines depict ensemble of models with misfit up to 1.5% higher than CSM-JOINT) and those associated with the coseismic slip model estimated from the LiDAR data alone (red lines). (B) Perspective view of the fault in CSM-JOINT from the SSW (thin black line with finial sphere is pointing North, and thin black line with no finial is pointing East), and the average slip vector in CSM-JOINT (orange arrow). The most, intermediate, and least compressive stresses (purple, tan, and blue lines, respectively), assuming that the most compressive stress is aligned with Sh_{max} from the World Stress Map (Heidbach *et al.*, 2016, 2018) and that least compressive stress is vertically oriented. Also shown is the direction of the maximum fault shear stress (plum colored arrow) for this orientation of principal stresses. 24

3.1 Focal mechanisms of several notable earthquakes in western Taiwan (double couple solutions from the Global Centroid Moment Tensor Catalog, GCMT), along with coseismic slip models (CSMs) of those earthquakes; thick lines indicate the top edge of the fault in the CSMs, and filled areas are the approximate regions of sizable fault slip in those CSMs (regions are approximated from figures in the associated publications, with filled polygons roughly correspond to the regions where slip was larger than about 20% of the maximum slip and are just for illustration purposes, readers should see references for details of their CSMS; Yoshioka (2001; ChiChi), Hsu *et al.* (2011; Jiashian), Lee *et al.* (2015; Nantou events), Chiang *et al.* (2016; Wutai), Huang *et al.* (2016; MeiNong), Qu *et al.* (2017; MeiNong), and Rau *et al.* (2022; MeiNong). 32

3.2 GNSS coseismic offsets for the Jiashian (**a** and **b**; Hsu *et al.*, 2011) and MeiNong (**c** and **d**; Huang *et al.*, 2016) earthquakes. Panels (**a**) and (**c**) are the horizontal deformation, while (**b**) and (**d**) are vertical deformation. Purple and red stars indicate the GCMT centroid locations for the Jiashian and MeiNong earthquakes, respectively. Shaded regions are generalized geological regions of Taiwan: Western Foothills (tan); Hsueshan Range, Backbone Range, and Eastern Central Valley Range (yellow); and Coastal Range (green) 36

3.3 Ascending interferograms capturing the coseismic displacements of the MeiNong earthquake (**a** and **b**), that are either inverted (training; **a**) or used to calculate the χ^2 of the resulting model (testing; **b**). Burgundy line indicates swath of LOS offsets in Fig. 3.11. Synthetic LOS offsets resulting from slip in the best fit MeiNong coseismic model (**c**; with best-fit double-couple of the model shown), and residual interferograms (**d** and **e**). 38

3.4 Descending interferograms capturing the coseismic displacements of the MeiNong earthquake (**a** and **b**), that are either inverted (training; **a**) or used to calculate the χ^2 of the resulting model (testing; **b**). Burgundy line indicates swath of LOS offsets in Fig. 3.11. Synthetic LOS offsets resulting from slip in the best fit MeiNong coseismic model (**c**; with best-fit double-couple of the model shown), and residual interferograms (**d** and **e**). 39

3.5 Location of the faults in the 20,000 best fitting coseismic slip models found in the initial search for the Jiashian (**a**) or MeiNong (**b**) earthquakes. Plotted point is the location of the center of the top of the fault plane, colored by the dip of the fault. Model fit *vs.* fault dip in the top 20,000 initial Jiashian (**c**) or MeiNong (**d**) coseismic slip models. Purple points depict the top 10,000 best fitting models and blue are the next 10,000; orange lines are the lowest χ^2 in 1° bins. Strike and dip of the fault planes in these 20,000 models for the Jiashian (**e**) or MeiNong (**f**) earthquakes, shown in a Lambert projection and colored according to the fit of the coseismic slip model. Values along the outer circumference indicate the strike of the fault plane, and numbers in the interior circles indicate either dip (green text) or codip (blue text); stars and asterisks depict the two nodal planes in the GCMT or USGS focal mechanisms, respectively. 43

3.6 Model fit *vs.* fault dip in the 10,000 trial faults in the integrated search for the Jiashian (**a**) or MeiNong (**b**) coseismic slip models; orange lines in panels (**c**) and (**d**) are from Figs. 3.5a and 5b, respectively. Strike and dip of the fault planes in the trial models for the Jiashian (**c**) or MeiNong (**d**) earthquakes in the integrated search. Strike and dip are shown in a Lambert projection and colored according to the fit of the coseismic slip model. Values along the outer circumference indicate the strike of the fault plane, and numbers in the interior circles indicate either dip (green text) or codip (blue text); stars and asterisks depict the two nodal planes in the GCMT or USGS focal mechanisms, respectively. 46

3.7 **a** Surface projections of the fault planes in the Jiashian (blue) and MeiNong (red) coseismic slip models with χ^2 within 10% of the best fitting model (38 and 107 models for Jiashian and MeiNong coseismic models, respectively; line thickness scales with χ^2). Also shown are the centroid locations of all 10,000 of the models in the integrated search, colored by χ^2 (coloring of Jiashian and MeiNong centroids as in Fig. 3.6a and 3.6b, respectively). Model fit *vs.* burial depths of all 10,000 trial models in the integrated search for the Jiashian (**b**) and MeiNong (**c**) earthquakes. 47

3.8 The slip distributions of the best fitting Jiashian (**a**) and MeiNong (**c**) coseismic slip models. To assess the degree to which the features of the slip are resolved, we plot the variance of the subfault slip in the coseismic models with χ^2 within 10% of the lowest χ^2 for the Jiashian (**b**; 38 models) and MeiNong (**d**; 107 models) earthquakes (all models used to compute the variance have strikes and dips similar to the best fit models; Fig. 3.7). Beachballs depict the double-couple focal mechanisms derived from the fault strike and dip, along with the weighted average slip rake, for each earthquake. Green and purple lines on the beachballs are the nodal planes from the USGS and GCMT focal mechanisms, respectively. 49

3.9 Predicted horizontal (**a** and **c**) and vertical (**b** and **d**) displacements for the best coseismic slip models determined of the Jiashian (**a** and **b**) and MeiNong (**c** and **d**) earthquakes. Vectors showing the model vertical displacements are slightly offset from the observed for clarity. The observed GNSS solutions are shown in black and are from Hsu *et al.*, 2011 (Jiashian; **a** and **b**) or Huang *et al.*, 2016 (MeiNong; **c** and **d**). Green rectangle is the surface projection of the fault planes and green dashed line is the projection of the top of the fault along the constant fault dip. 50
3.10 The GCMT focal mechanism of the MeiNong earthquake compared to the focal mechanisms for the best model found from the initial search assuming uniform slip and from the integrated search (the slip surface is highlighted). 52
3.11 Line of sight (los) coseismic offsets for the MeiNong earthquake along the swath shown in Figs. 3.3 and 3.4, from southwest to northeast: profiles in (**a**) and (**b**) are from the training interferograms, either ascending or descending, respectively, while (**d**) and (**d**) are from the testing interferograms. Solid lines shows the median los offset within the swath, and shaded regions depict the range in which 90% of the los is along the swath (defined by the 5^{th} to 95^{th} percentiles). 52
3.12 (**a**) Main slip patch of the Jiashian (blue) and MeiNong (red) coseismic slip models (defined as subfaults with slip $\geq 20\%$ of the maximum slip in each model, excluding subfaults at the edges of the fault domain, *cf.*, Figs. 3.8a and c); arrows are the weighted average slip direction of each coseismic slip model. (**b**) Map view of slip patches with epicenters of aftershocks determined by *Huang* et al. (2011; green squares, Jiashian aftershocks), *Wen* et al. (2017; dark red circles, MeiNong aftershocks), and *Hsu* et al. (2020; purple, orange, and gold circles, MeiNong aftershocks); pink triangles are locations where ground fissures were observed by *Yi* et al. (2023). (**c**–**h**) Cross sections indicated in **b**, symbols are aftershocks as in **b**, and blue or red lines are the main slip patch of the Jiashian or Meinong coseismic models, respectively. 55

4.1 Geodetic data used in the MeiNong coseismic example: GNSS offsets from Haung *et al.*, 2016 (**a** and **b**) and interferograms from 3 (**c** and **d**). Red star in (**a**) and (**b**) is the GCMT centroid and GCMT focal mechanism is indicated. Figure after 3. 72
4.2 Fusion results for MeiNong 2016, earthquake. Colors show vertical deformation, the vector field is horizontal deformation, and the yellow triangles are the locations of GPS stations used in the fusion. The number of plotted horizontal samples from the posterior has been reduced to improve figure clarity. 73
4.3 Fusion results for Sparta, 2020 earthquake. The red line is a transect across the surface rupture, the associated profiles are shown in fig #. The swath indicates the region of data to be projected onto the transect profiles. 75
4.4 3-D differential LiDAR observations for comparison to the fusion results for Sparta. 76

4.5 Fusion results with LiDAR and InSAR observations for transect shown in fig. #: profiles (A), (B), and (C) show 3-D differential LiDAR observations X, Y, and Z components, respectively, while (D) shows the S-1 and ALOS-2 observations. For profiles (A), (B), and (C) the scatter plots are the observation values with their associated uncertainties, the red line is the fusion result for each component, and the red shade is the 98% confidence interval for the fusion results. In profile (D) the black and brown scatter plots are the S-1 and ALOS-2 observations, respectively, and the purple and green lines are the S-1 and ALOS-2 fusion results as seen from the respective satellites. 77

A.1 Google Earth view of the region around the Sparta earthquake (Google, ©2020 CNES / Astrium, Maxar Technologies), with the mapped surface rupture (yellow line) and outlines of prominent industrial parks (blue polygons). 87

A.2 Samples of the ALOS-2 (A) and S-1 (B) interferograms, and LiDAR verticals (C) and horizontals (D) selected for inversion, with cross indicating the hypocenter, and dashed line indicating the field mapped surface rupture (Figueiredo et al., 2022). 88

A.3 Total mistfit to the ALOS-2 and S-1 interferograms, and LiDAR, with the data corresponding to the industrial parks masked, as a function of the fault dip. Dips $> 90°$ are northeast dipping faults. 89

A.4 (A) Slip distribution in CSM-S1, with black arrows indicating the slip vector on each subfault, and colors indicating the magnitude of slip. Synthetics and residuals from CSM-FULL for S-1 (B & C), ALOS-2 (D & E), and LiDAR components X, Y, and Z (F)-(K), respectively. Colors in panels (C)-(K) follow colorbar in panel (B). Cross indicates the hypocenter, blue polygons outline prominent industrial parks, and black rectangle is the surface projection of the fault. 90

A.5 (A) Slip distribution in CSM-FULL, with synthetics and residuals from CSM-S1 for S-1 (B & C), ALOS-2 (D & E), and LiDAR components X, Y, and Z (F)-(K), respectively. Colors in panels (C)-(K) follow colorbar in panel (B), all other symbols are as in Fig. S4. 91

A.6 (A) Slip distribution in CSM-DAR, with synthetics and residuals from CSM-DAR for S-1 (B & C), ALOS-2 (D & E), and LiDAR components X, Y, and Z (F)-(K), respectively. Colors in panels (C)-(K) follow colorbar in panel (B), all other symbols are as in Fig. S4. 92

A.7 (A) Slip distribution determined from the LiDAR ICP differencing, with black arrows indicating the slip vector on each subfault, and colors indicating the magnitude of slip. Synthetics and residuals from CSM-LiDAR for S-1 (B & C), ALOS-2 (D & E), and LiDAR components X, Y, and Z (F)-(K), respectively. Colors in panels (C)-(K) follow colorbar in panel (B), all other symbols are as in Fig. S4. 93

A.8 GNSS time series from station NCSR, from the Nevada Geodetic Laboratory (Blewitt *et al.*, 2018), with the best fit model used to estimate the Sparta coseismic offsets (panels A and B are the east and north components, respectively). . 94

A.9 (A) von Mises PDF used as the likelihood function in the stress estimation. (B) Marginal posterior PDF of σ_{M}, assuming that $\tau_{\max}$ is greater than 8 MPa (pink) or 10 MPa (orange). Brown field indicates a range of lithostatic stress at 1 km, corresponding to densities from 2600–2800 kg/m^3. (C) Posterior PDF of ρ and δ assuming $\tau_{\max} \geq 6$ or 10 MPa. 96

B.1 Histograms of the horizontal (**a** and **d**) or vertical (**b** and **e**) coseismic offsets in the Jiashian (Hsu *et al.*, 2011) and MeiNong (Huang *et al.*, 2016) data. Panels **c** and **f** show the histograms of the ratio of the horizontal to vertical deformation inferred at each station. 99

B.2 The fault dimension ($L \times W$; **a** and **d**), slip magnitude (**b** and **e**, and associated moment magnitude (assuming shear modulus of 30 GPa; **c** and **f**) of the best fitting 20,000 models determined in the initial search for the Jiashian (**a**–**c**) and MeiNong (**d**–**f**) earthquakes. 100

B.3 Centroid depth inferred for all 10,000 trial fault planes in the integrated search of the Jiashian (**a**) or MeiNong (**b**) coseismic slip models. Whiskers indicate the range of centroid depths of the models with χ^2 within the best fit of each coseismic slip model (38 and 107 models for the Jiashian and MeiNong coseismic slip models, respectively). 101

B.4 Residuals between observed and predicted horizontal (**a** and **c**) and vertical (**b** and **d**) for the best coseismic slip model determined of the Jiashian (**a** and **b**) and MeiNong (**c** and **d**) earthquakes. The observed GNSS solutions are shown in black and are from Hsu *et al.*, 2011 (Jiashian; **a** and **b**) or Huang *et al.*, 2016 (MeiNong; **c** and **d**). Green rectangle is the surface projection of the fault planes and green dashed line is the projection of the top of the fault along the constant fault dip. 102

B.5 Observed and predicted LOS offsets at the quadtree sample points for the four interferograms capturing coseismic deformation of the MeiNong earthquake. The predicted LOS offsets are from the coseismic model with the lowest χ^2, where the interferograms in panels (**a**) and (**c**) were inverted to determine the model while the interferograms in panels (**b**) and (**d**) were only used to calculate the χ^2 of that model. Green rectangles indicate the surface projection of the fault plane, and green dashed line is the projection of the top of the fault plane to the surface. 103

B.6 The GCMT focal mechanism of the Jiashian earthquake compared to the focal mechanisms for the best model found from the initial search assuming uniform slip and from the integrated search (the slip surface is highlighted). 104

B.7 Observed GNSS offsets of MeiNong coseismic deformation (black) along with the offsets predicted by either the best fit coseismic model (green, as in Fig. 9 of the main text) or an alternative model (pink). Panels (**a**) and (**b**) are the horizontal predictions and residuals, respectively, while panels (**c**) and (**d**) are the vertical predictions and residuals, respectively. Vectors showing the model vertical displacements are slightly offset from the observed for clarity. The alternative model has a strike, dip, and average weighted rake of -83°, 20° 20° and has a centroid depth of 16.3 km (depth to the top of the fault plane is 10.2 km). Rectangle is the surface projection of the fault plane in the best fit (green) or alternative (pink) model, and dashed lines are the updip projection of the top of the fault plane. 105
B.8 Observed and predicted LOS offsets at the quadtree sample points for the four interferograms capturing coseismic deformation of the MeiNong earthquake. The predicted LOS offsets are from Fig. B.6 and caption is as in Fig. B.4. 106
B.9 The number of aftershocks per day following the MeiNong earthquake (data from Hsu *et al.*, 2020), for aftershocks in either one of the groups defined in Fig. 3.12, or in both of the groups associated with the main slip patch we infer in the MeiNong earthquake. The dashed lines are reference Omori-Utsu aftershock decays (*e.g.,* Utsu *et al.*, 1995; Davidson *et al.*, 2015). 107

S1 Correlation of random sample locations with near-surface rupture location, the red line is the mapped surface rupture, and the color bar is shared. Panel (A) shows correlation between locations calculated using an unmodified squared-exponential kernel. Panel (B) shows correlation between locations calculated using the modified squared-exponential designed to accommodate the discontinuity created by the surface rupture. 113
S2 Uniform random sampling used for Sparta 2020, earthquake data fusion. Panel (A) shows samples from Sentinel-1 interferogram, panel (B) shows samples from the ALOS-2 interferogram, and panels (C) and (D) shows samples from 3-D differential LiDAR vertical and horizontal components, respectively. All 3-D differential LiDAR samples are collocated. 113
S3 Histograms of Sparta data uncertainties (blue) prior to fusion by Gentoo and uncertainties for the posterior samples (orange) at the same locations. Panels: (A) S-1 (B) ALOS-2 (C) LiDAR-x (D) LiDAR-y (E) LiDAR-z 114
S4 Histograms of MeiNong data uncertainties (blue) prior to fusion by Gentoo and uncertainties for the posterior samples (orange) at the same locations. Panels: (A) GNSS-x (B) GNSS-y (C) GNSS-z 114

LIST OF TABLES

TABLE

2.1 Optimal penalty parameters, λ_1 and λ_2, used in the inversion for the three coseismic slip models, fault dip, the average rake weighted by the slip magnitude, RMSE associated with the InSAR, LiDAR, and full data sets, and estimated stress drop, $\overline{\Delta\sigma}$ (see Electronic Supplement for calculation of $\overline{\Delta\sigma}$) for each of the coseismic slip models. 22

3.1 Orbits and dates of SAR acquisitions (year-month-day) used to produce interferograms of the MeiNong coseismic deformation. The time span of each interferogram is indicated, along with number of days prior to ("pre-eq") and following ("post-eq") the earthquakes. The role of the interferograms in the inversion process, either being inverted to determine the coseismic slip model ("training") or unseen data used to test the resulting cosiemsic slip model ("testing"), is indicated. 37

3.2 Nodal plane orientations of the GCMT and USGS focal mechanisms most closely associated with the slip surfaces resolved here, along with location and depth of the centroid (1: USGS location is the epicenter); parameters of the fault plane and centroid location for the model with lowest χ^2 in the initial search with uniform fault slip, and the best model from the integrated search. Also given are the standard deviation of the parameters from an ensemble of all models within 10% of the best-fit χ^2, for each earthquake (38 and 107 models for Jiashian and MeiNong coseismic models, respectively). Depth is to the top of the fault plane; λ is either slip rake or the average slip rake in the subfaults, weighted by the slip magnitude in that subfault, for the uniform or the integrated best/ensemble, respectively. For the uniform model, centroid depth is the depth of the center of the fault plane. 44

LIST OF APPENDICES

A Supplementary Material for Chapter 2 . . . . . **86**
Additional InSAR figures and coseismic slip models 86
Estimating coseismic offset at GNSS site NCSR 86
Stress drop 89
Comparison of CSM-JOINT to World Stress Map 95
B Supplementary Material for Chapter 3 . . . . . **98**
Additional Figures 98
C Supplementary Material for Chapter 4 . . . . . **108**
Covariance Analysis 108
Additional Figures 112

ABSTRACT

In geophysics, geodesy plays a critical observational role, focusing on measuring and understanding the Earth's shape, orientation in space, and gravitational field, as well as their temporal changes. The observations from various geodetic techniques are utilized to constrain geophysical models through statistical estimation methods. However, conventional approaches may struggle with noisy or sparse data, leading to invalid models. This dissertation presents two innovative approaches for effectively managing challenging data sets in the context of modeling sources and mapping deformation associated with geophysical processes. These methods aim to enhance model reliability and accuracy, even in the presence of data limitations. We apply both methods to analyze coseismic surface deformation observations from earthquakes in Sparta, North Carolina, and Jiashian and Meinong, Taiwan. These case studies demonstrate the effectiveness of our approaches in handling noisy and sparse data, improving the accuracy of the resulting geophysical models and deformation mappings.

In chapter 2 we describe a novel estimation methodology for estimating coseismic slip models from geodetic observations of coseismic surface deformation. We apply our method to observations from the August 9, 2020, M_w 5.1 Sparta, North Carolina earthquake captured by ALOS-2 and Sentinel 1A/B interferograms, along with differential LiDAR. Due to the relatively moderate surface deformation and the inherent uncertainties in the interferometric data, the interferograms displayed low signal-to-noise ratios. This issue was exacerbated by resolution discrepancies between the interferograms and the DEM used in processing, leading to the introduction of spurious signals related to local structures. Despite these challenges, coseismic slip was effectively modeled using our proposed method. Five coseismic slip models were developed: one based solely on the Sentinel 1A/B interferogram, another using both interferograms, a third that included all InSAR data while masking spurious signals from industrial areas, one based only on LiDAR displacements, and a final model that combined masked InSAR and LiDAR data. Our method produced a coseismic slip model for the Sparta earthquake that better aligns with existing ancillary information. This application highlighted the methodology's effectiveness in managing noisy and incomplete data, demonstrating its robustness and reliability in generating accurate models under challenging conditions.

Chapter 3 applies the same estimation strategy to coseismic surface deformation from the 2010 M 6.3 Jiashian and the 2016 M 6.4 MeiNong earthquakes in southern Taiwan recorded by GNSS and InSAR. Notably, neither earthquake produced surface rupture, leading to uncertainty about the associated nodal planes from seismological focal mechanisms. For the Jiashian event, the new coseismic model aligns well with existing focal mechanisms and models. However, for the MeiNong event, geodetic data suggested a shallower and more northerly slip surface than previous models indicated. This discrepancy highlights potential biases in earlier models due to constraints on fault geometry, particularly depth. The similarity in fault strikes and the proximity of inferred slip regions suggest both earthquakes likely occurred on a single fault structure that dips eastward and steepens with depth. This application underscored our methodology's effectiveness in producing more accurate models by integrating the estimation of distributed slip with the search for fault geometry. This holistic approach enhances the reliability of the results, allowing for better representation of the underlying fault structure.

In chapter 4 we outline a novel method for fusing geodectic data and demonstrate it's effectiveness on observations of coseismic surface deformation. Our fusion approach utilizes a semi-parametric latent factor model framework, which combines a parametric mapping of relationships between various geodetic observational modalities with a non-parametric representation of both observations and the latent deformation field. Our method provides a single, three component deformation field determined through multi-output Gaussian processes regression. This technique leverages the complementary features of different data types to filter out spurious signals, leading to a more accurate estimate of ground deformation. We applied this method to analyze coseismic deformation from the 2020 Sparta, NC, USA, and the 2016 MeiNong, Taiwan, earthquakes, fusing InSAR data with LiDAR for Sparta and GNSS data for MeiNong. The results demonstrated significant improvements in the precision and coherence of the deformation field.

CHAPTER 1

Introduction

1.1 Historical Context

"*Mathematicians deal with possible worlds, with an infinite number of logically consistent systems. Observers explore the one particular world we inhabit. Between the two stands the theorist. He studies possible worlds but only those which are compatible with the information furnished by observers. In other words, theory attempts to segregate the minimum number of possible worlds which must include the actual world we inhabit. Then the observer, with new factual information, attempts to reduce the list further. And so it goes, observation and theory advancing together toward the common goal of science, knowledge of the structure and observation of the universe.*"

- Edwin Powell Hubble

Within the context of geophysics, the field of geodesy most often takes on the role of the observer in the relationship described by Hubble. Geodesy as a scientific discipline focuses on measuring and understanding the Earth's shape, orientation in space, gravitational field, and how they change with time. By employing advanced techniques and technologies, geodesists analyze the planet's physical characteristics, such as its size, shape, and the subtle variations in its gravitational pull. The field is crucial for numerous applications, from mapping and navigation to satellite positioning and geophysical studies. Geodesy integrates principles from mathematics, physics, and engineering to provide accurate data that supports a wide range of scientific and practical endeavors, ensuring our ability to navigate and understand our world with precision.

Geodesy has the honor of being one of the oldest scientific disciplines (Torge *et al.*, 2023). Thales of Miletus (c. 624–546 BC) pioneered early concepts of geometry, including the measurement of the Earth, which he imagined as a disk floating on the oceans. In contrast, Pythagoras of Samos (c. 580–500 BC) envisioned the Earth as an ideal sphere suspended

in space. Aristotle (384–322 BC) described geodesy as the practical use of geometry, while Eratosthenes of Cyrene (c. 276–195 BC) became the first to estimate the Earth's radius using astronomical and geodetic observations. From observations of so-called vertical deflection, which was ultimately determined to be a measure of how far the direction of gravitational pull at a given point of interest is rotated by local mass anomalies, Carl Friedrich Gauss (1777-1855) concluded that Earth's gravity varied geographically and the true figure of the Earth is given by the surface of the ocean absent of tides, currents, etc. This ideal surface was later dubbed the "geoid" by one of Gauss' students Johann Benedict Listing (1808-1882). The determination of the geoid became a fundamental challenge of geodesy and still is to this day. The 1838 publication of Friedrich Wilhelm Bessel's *Gradmessung in Ostpreußen* (Bessel and Baeyer, 1838) marked a significant advancement in the field of geodesy. In this work, Bessel introduced the application of the method of least squares to the calculation of a network of triangles and the overall reduction of observations, heralding a new era in geodetic science. The majority of the relevant theories were subsequently developed by the German geodesist Friedrich Robert Helmert in his renowned works, *Die mathematischen und physikalischen Theorien der höheren Geodäsie*, Volumes 1 and 2 (Helmert, 1880 & 1884) in 1880 and 1884, respectively. In 1906, Helmert was recognized for deriving the first global ellipsoid, and just a few years later, in 1909, US geodesist John Fillmore Hayford developed a global ellipsoid based on intercontinental isostasy. Hayford's ellipsoid was later adopted as the "International Ellipsoid 1924" by the International Union of Geodesy and Geophysics (Hayford, 1909).

As geodesy was prospering at the turn of the 20th century, the rest of geophysics was entering a revolutionary age of it's own. In 1905 Ernest Masson Anderson introduced his theory of faulting (Anderson, 1905), Alfred Wegener was formulating his theory of continental drift (Wegener, 1912) which would evolve into the theory of plate tectonics, and in 1910 Harry Fielding Reid proposed his theory of elastic rebound (Reid, 1910). He compared triangulation surveys from before and after the great 1906 San Francisco earthquake (Lawson, 1906) and concluded that the earthquake was the result of released strain energy that had accumulated through elastic deformation in the crust on either side of the San Andreas fault. His theory laid the foundation for much of our current understanding of earthquakes and effectively demonstrates how theory and observations drive each other, advancing our scientific knowledge. Today, technology used for making geodetic observations has advanced significantly, enhancing both the coverage and accuracy of measured ground positions. Modern geodetic techniques such as very long baseline interferometry (VLBI), global navigation satellite system (GNSS), interferometric synthetic aperturre radar (InSAR), structure-from-motion (SfM) photogrammetry, and the latest addition, light Detection and ranging (LiDAR), each

offer unique perspectives and capabilities. Observations from these methods are essential for exploring and understanding a range of geophysical phenomena that cause surface deformation, including earthquakes, fault creep, landslides, volcanic activity, and groundwater fluctuations. Our understanding of these phenomena is advanced either through the direct analysis of those observations or by developing and constraining mathematical models — numerical or analytical — that represent our current knowledge of the phenomena being studied. Examples of mathematical models for ground deformation resulting from some of the geophysical processes mentioned include Volterra's model of dislocation (Steketee, 1958), point and finite rectangular sources in a homogeneous elastic half-space (Okada 1985, 1992), spherical sources in a homogeneous elastic half-space (Mogi, 1958), and sources in a heterogeneous elastic half-space (Singh, 1970). These and other models are refined using our observations of surface deformation to deduce various properties of the Earth related to specific events or regions.

1.2 Extending Our Reach

"*Too often we forget that genius, too, depends upon the data within its reach, that even Archimedes could not have devised Edison's inventions.*"

– Ernest Dimnet

To paraphrase Ernest Dimnet, our ability to innovate and solve problems is directly tied to the quality of the observations we collect and, more crucially, how we use them. Without data and the proper tools to analyze it, our potential for success is limited. So, how do we transform observations into meaningful interpretations and broaden our understanding of the Earth? As discussed at the end of the previous section - albeit simplified - we can trace a path from a general theory to a representative mathematical model of that theory. Building on that, the successful application of a mathematical model requires the use of estimation methods and inverse theory to infer the most probable model parameters for a given set of observations. Once the most accurate model is determined, it can offer valuable insights capable of guiding future research, support beneficial societal changes, and contribute to scientific advancements (Fig. 1.1). For example, researchers deployed an extensive GNSS network for the plate boundary observatory (PBO; Silver *et al.*, 1999) in California, USA and used it to track motion across the plate boundary between the Pacific and North American plates. Observations from the PBO provided crucial data for countless studies and contributed to a better understanding of plate boundary processes within the greater context of the theory of plate tectonics. Our improved understanding of plate boundary

processes aided in the development of earthquake forecast models (Field *et al.*, 2014) which provide useful information for scientists and citizens alike.

Assuming we have a mathematical model that faithfully characterizes theory, the accuracy of our estimated models and the reliability of our interpretations depend on two factors: 1. The quality of our observations. 2. The suitability of the chosen estimation method. It is important to note that as the former decreases, the importance of the later increases.

First, when collecting high-quality observations, several challenges can arise: (1) the inherent precision limitations of the sensors, (2) inadequate sensor coverage that results in incomplete data sets, (3) sources located at the edges of the sensors' effective range, and (4) noise that is comparable to the desired signal. These issues can make it difficult to extract useful information and accurately estimate models, impeding our ability to correctly interpret them within the greater context of our problem. While sensor precision limitations (1) are an engineering issue beyond the scope of scientific inquiry, the other challenges are significant concerns for practicing scientists. When faced with incomplete or inaccurate observations, researchers often resort to interpolation, using one data set to correct another, or a combination of these methods. Another approach is to use "data integration" or "data fusion." Data fusion involves combining multiple sources to improve the quality of information, with enhancements often resulting in greater accuracy or relevance.

Second, regarding the choice of estimation method, let me briefly clarify what "suitability" means in this context. When we pair a mathematical model with an estimation method, it results in a statistical model that characterizes the system being analyzed with respect to our observations. The key difference between a mathematical model and a statistical model is that the latter accounts for uncertainties in our observations, whereas the former does not. A useful way to conceptualize the difference is that a statistical model adds a stochastic component to the deterministic description of our observations provided by a mathematical model, or,

Observations = Deterministic (Mathematical Model) + Stochastic (Estimation Method)

Essentially, the choice of estimation method dictates how measurement errors are addressed and frequently incorporates additional prior information through regularization or constraints. In many instances, selecting an inappropriate method can lead to a poor representation of the system under study and yield misleading results.

My dissertation aims to enhance our capability to develop informative models and improve the interpretability of observations in situations involving (2) insufficient sensor coverage, (3) sources at the edge of sensor range, and/or (4) significant noise. To achieve these goals, I

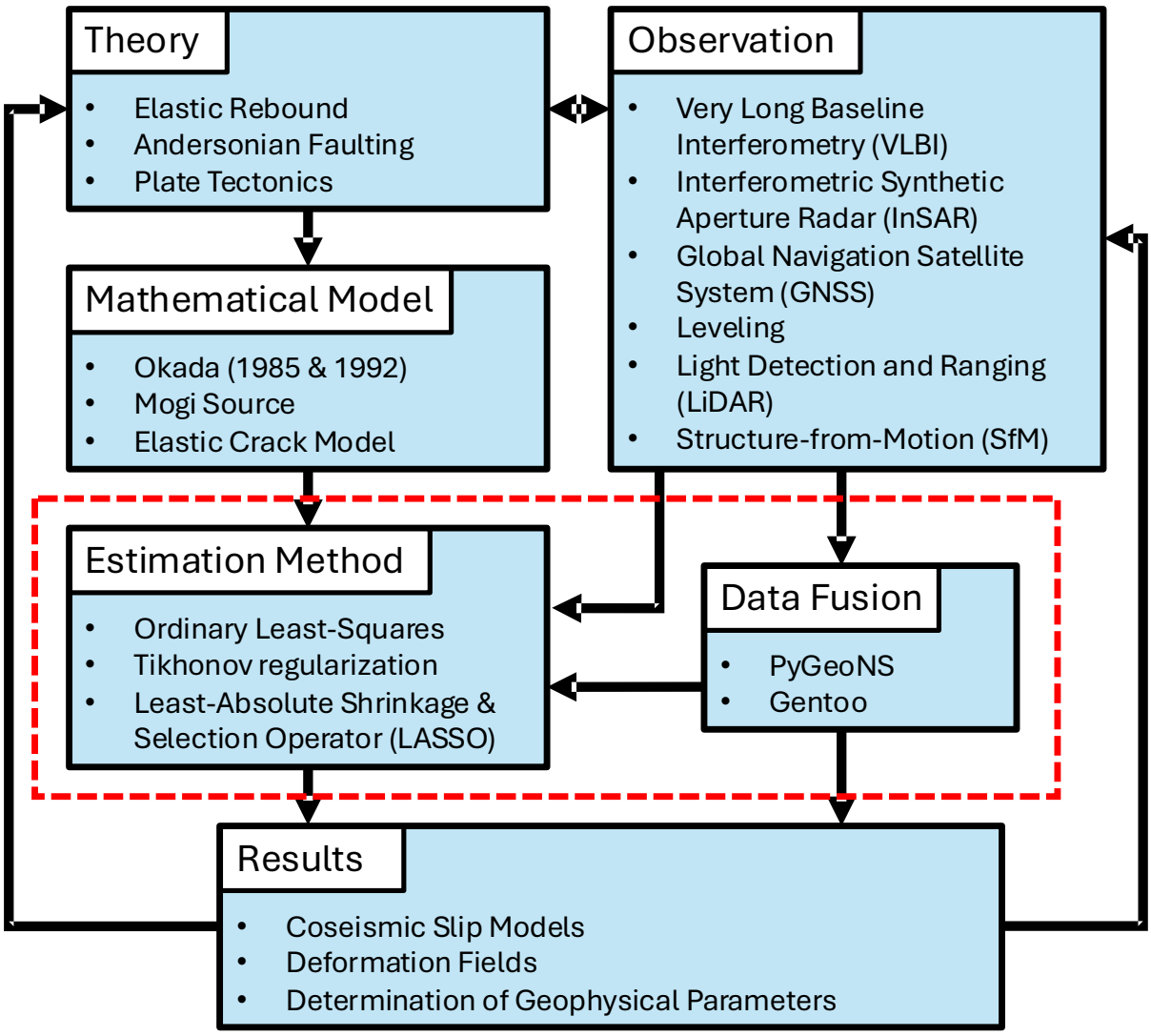


Figure 1.1: A simplified graphical representation of the interconnection between theory, observation, mathematical modeling, and how they are utilized in conjunction with estimation methods to produce scientific results for geophysical and geodetic studies. The red dashed box indicates areas in this work flow that this dissertation provides contributions.

propose a novel approach that combines an estimation method from compressed sensing with an enhanced optimization scheme for determining coseismic slip models and introduce a new method for fusing geodetic data. Chapters 2 and 3 focus on the application of the improved estimation method, while Chapter 4 discusses the methodology for geodetic data fusion. Quick summaries are provided below:

1.3 Estimation method for coseismic slip models (Chapters 2 and 3)

Effectively designing geophysical inverse problems is essential. The success of this design largely hinges on our ability to utilize statistical concepts to integrate prior information and manage measurement errors (Tarantola, 2005). Additionally, geophysical problems are notoriously under-determined (Belot, 2015) and typically require regularization or prior constraints to ensure physically realistic results. The estimation of coseismic slip models is no exception. Here, the procedure adopted by most researchers is to first assume uniform slip on a planar fault and use a Monte Carlo search algorithm to estimate the various geometric parameters of that fault. After an optimal geometry as been found for the fault, it is fixed in that position, divided into sub-faults, and a slip distribution is determined using a linear least-squares inversion using Tikhonov regularization (Tikhonov *et al.*, 1995) with Laplacian smoothing. However, He *et al.* (2017) demonstrated that assuming uniform slip may not provide the most accurate orientation for the modeled fault. The use of Tikhonov regularization with Laplacian smoothing is also debatable, especially in cases where data is sparse or significantly affected by noise. This approach is questioned not only because its selection is somewhat ad hoc but more importantly because of its sensitivity to noise, given its assumption of Gaussianity for both data error and model parameter distributions. To address these issues, we propose two modifications: 1. Integrate the estimation of distributed slip into the search for optimal fault geometry, where slip distributions are determined and assessed for each potential fault configuration. 2. Employ a more robust estimation method that better accounts for data errors and incorporates physical information from an earthquake.

As a demonstration, we estimate coseismic slip models for the 2020 M_w 5.1 Sparta, North Carolina, USA earthquake (Chapter 2), as well as for the 2010 M_w 6.3 Jiashian and 2016 M_w 6.4 MeiNong earthquakes in Taiwan (Chapter 3). The Sparta earthquake had relatively little data available, only two interferograms with similar viewing geometries and 3-D differential LiDAR produced useful estimations of surface deformation. The small size, limited data, and significant noise present in the Sparta earthquake data made it an ideal candidate

for testing the performance of our new estimation methods ability to handle problematic data. Additionally, this was only the second coseismic slip model to incorporate LiDAR observations into the slip inversion. The Jiashian and MeiNong earthquakes posed a different challenge. The data quality for both Jiashian and MeiNong was significantly better than for Sparta, with sufficient GNSS coverage for both events and additional InSAR observations available for MeiNong. However, the data was still somewhat ambiguous as to which nodal plane was responsible. This was particularly true for the MeiNong earthquake, where determination of the nodal plane responsible for the earthquake was still difficult even with the additional InSAR observations. Again, we were presented with a great opportunity to test our method, specifically our integrated approach to the search for fault geometry and estimation of distributed slip.

1.4 Geodetic Data Fusion (Chapter 4)

Chapter 4 introduces our proposed method for fusing geodetic observations of surface deformation. Our objectives with this fusion include achieving a more accurate and consistent view of surface deformation, creating a differentiable field for deriving strain maps, and eliminating any spurious signals. To meet these goals, we employ semi-parametric latent factor modeling (SLFM), which integrates non-parametric Gaussian processes with parametric linear mixing. The SLFM framework can simultaneously process multiple data sources from different sensors to produce a single, three-component deformation field. This approach offers several advantages over existing methods. Primarily data-driven, it makes minimal assumptions about the underlying signal or its origin, does not require that observations from different sensors be collocated, and facilitates information sharing between different data sources, allowing the strengths of one data type to bolster up the weaknesses in others. We apply our fusion method to the same coseismic deformation observations from the 2020 Sparta, 2010 Jiashian, and 2016 MeiNong earthquakes discussed in the previous section.

CHAPTER 2

Imaging Left-Lateral and Reverse Near-Surface Slip of the 2020 M5.1 Sparta, North Carolina, Earthquake

Abstract

Coseismic deformation of the 09 Aug 2020 M_w 5.1 Sparta, North Carolina earthquake was captured by an ALOS-2 interferogram, a Sentinel 1A/B interferogram, and differential LiDAR. Owing to the moderate surface deformation compared to the inherent uncertainties of interferometric data, the interferograms suffered from low signal-to-noise ratios, exacerbated by spurious signal arising from the discrepancy in resolution between the interferograms and DEM used during processing. Nevertheless, coseismic slip can be imaged using graph-guided fused LASSO, an inverse method that combines sparsity constraints and smoothness regularization, to infer signal from noisy and/or incomplete data. We develop five coseismic slip models, one determined only from the Sentinel 1A/B interferogram, one determined from both interferograms, one determined from all InSAR data masking potentially spurious data corresponding to industrial parks, one from LiDAR 3-D displacements only, and one constrained by the masked InSAR and the LiDAR data. All five models are of coseismic slip on a single fault plane, trending northwest-southeast with dips ranging from 41–60° to the southwest. Coseismic slip is imaged to be shallow, with predominantly oblique reverse slip extending to about 2 km depth. We find that masking the interferometric data corresponding to the industrial parks yields a coseismic slip model in better concordance with ancillary information about the Sparta earthquake, and that the LiDAR data yield additional constraints on near-surface coseismic slip. We show that our preferred coseismic slip model is consistent with a stress regime that does not depart from an Andersonian thrust regime to a large degree, constraining that the background stress is larger than 20–30 MPa.

2.1 Introduction

[1]The M_w 5.1 Sparta, North Carolina earthquake occurred on 09 Aug 2020 and involved slip on a fault now known as the Little River fault (Hill *et al.*, 2020). The Sparta earthquake resulted in 60 houses left uninhabitable and an additional 465 houses damaged, yet fortunately there were no reported fatalities or significant injuries (NGDC/WDS, 2023). The earthquake was the largest to occur in North Carolina since 1926, and was the largest in the eastern United States since the 2011 M_w 5.8 Mineral earthquake in Virginia, approximately 330 kilometers to the northeast (Fig. 2.1). Notably, the Sparta earthquake is the only recorded earthquake in the southeastern United States to produce surface rupture. The epicentral area sits in proximity to several zones of intraplate seismicity in the southeastern United States (Fig. 2.1). The Sparta earthquake is just to the south of the Giles County seismic zone in northwest Virginia (GCSZ; Fig. 2.1). The GCSZ is a narrow lineation of microseismicity which was defined based on the probable location of the m_b 5.8 earthquake in 1897 (*e.g.*, Bollinger and Wheeler, 1983; Powell *et al.*, 1994), and is likely be a long-lived aftershock sequence similar to as argued for the New Madrid Seismic Zone (Stein and Liu, 2009). The Sparta earthquake occurred within a region of diffuse seismicity extending along the Appalachian Mountains from the GCSZ, to the south through VA and NC (Fig. 2.1), a broad region that might be referred to as the Blue Ridge seismic province. The 1916 magnitude 5.2 Skyland and the 1926 magnitude 5.2 Mitchell County earthquakes also occurred within this region (*e.g.*, Figueiredo *et al.*, 2022).

Wicks and Chiu (2022) used a single interferometric synthetic aperture radar (InSAR) interferogram to argue that the Sparta earthquake involved slip on two fault planes: a southeast-northwest striking normal fault with a dip of about 45° to southwest, corresponding to the observed surface rupture on the Little Creek fault, and an approximately north-south striking reverse fault with a dip of about 30° to the east. Since all reported focal mechanism solutions of the Sparta earthquake show that fault slip was oblique reverse, Wicks and Chiu (2022) posited that the normal fault slipped aseismically with a M_w of 5.14. Wicks and Chiu (2022) further posited that the aseismic slip was likely induced by seismic reverse slip on the north-south striking fault, with M_w of 5.16. However, their coseismic model is at odds with two observations. First, the stress field over the eastern US is generally consistent with oblique-reverse slip (*e.g.*, Snee and Zoback, 2020; Levandowski *et al.*, 2018, and not active normal faulting. Second, and more importantly, coseismic offsets observed both at the surface and in trenches across the rupture trace indicate that slip on the Little Creek

[1]Chapter 2 is published in *Bulletin of the Seismological Society of America* as Szymanski, E. D., Hetland, E. A., and Figueiredo, P. M. (2024). Imaging left-lateral and reverse near-surface slip of the 2020 M_w 5.1 Sparta, North Carolina, earthquake. *Bull. Seismol. Soc. Am.*, 114(4):1870–1883

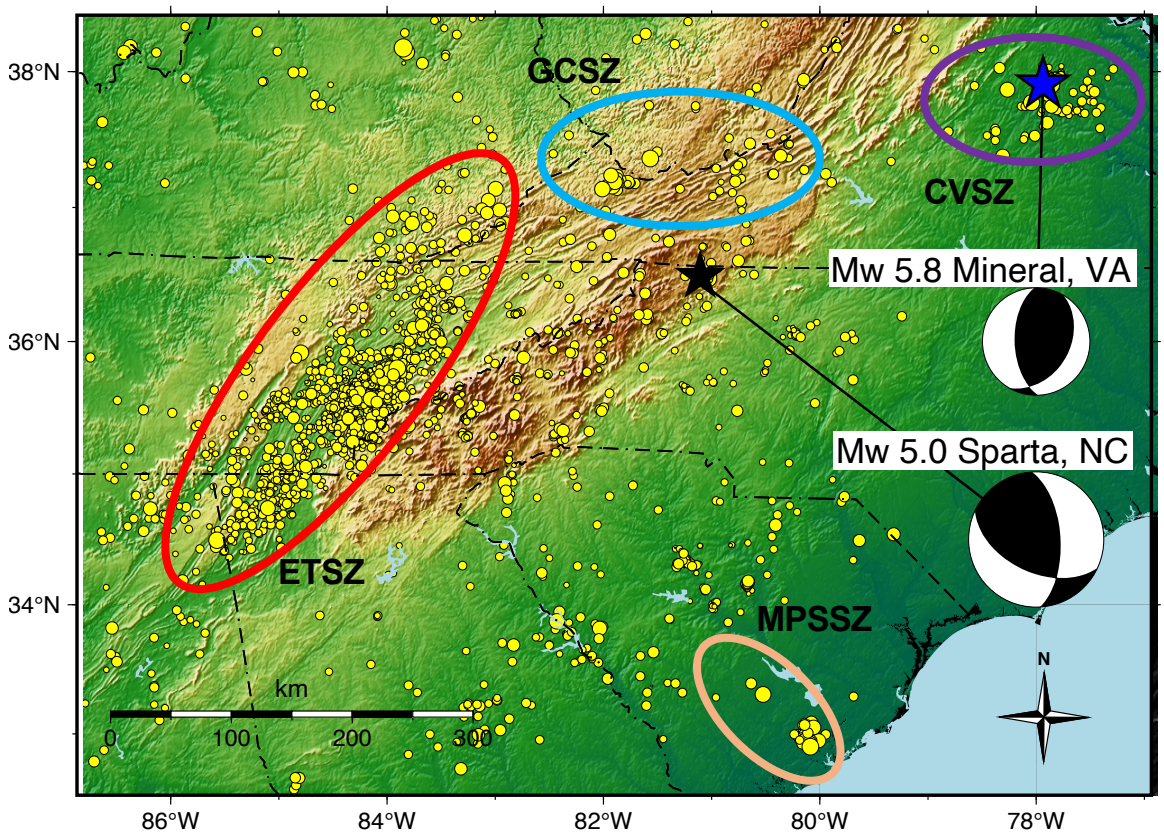


Figure 2.1: Map showing earthquake epicenters from 1970–2023 (see Data and Resources), along with the double-couple focal mechanisms of the 2011 Mineral, VA (USGS; blue star indicates the hypocenter), and 2020 Sparta, NC (Saint Louis University Earthquake Center; black star), earthquakes. Ellipses indicate the approximate locations of seismic zones: Middleton Place-Summerville Seismic Zone (MPSSZ), the Eastern Tennessee Seismic Zone (ETSZ), the Giles Creek Seismic Zone (GCSZ), and the Central Virginia Seismic Zone (CVSZ).

fault was reverse-oblique (Figueiredo *et al.*, 2022), and not normal as would be predicted by the Wicks and Chiu (2022) coseismic model.

We use both InSAR and Light Detection and Ranging (LiDAR) data to investigate the coseismic surface deformation. There is limited GNSS coverage in the area surrounding the Sparta earthquake, with just three sites in the North Carolina Geodetic Survey CORS network, two campaign and one continuous (NCSR). NCSR is included in the University of Nevada Geodetic Laboratory GNSS solutions (Blewitt *et al.*, 2018), but does not appear to be in Earthscope's GNSS solution. Wicks and Chiu (2022) noted that NCSR is located on top of a building that was damaged during the earthquake, and was not used to constrain their coseismic model. We also do not use the NCSR offset to constrain our model, but we following Wicks and Chiu (2022) we do compare our model predicted offset to it. The presence of significant amounts of vegetation and man-made structures, together with the moderate magnitude of the Sparta earthquake, results in a low signal-to-noise ratio (SNR) of the InSAR measurements. Nevertheless, coseismic deformation can be detected in two ascending pass interferograms, one from Wicks and Chiu (2022) and one described below. LiDAR surveys also captured a coherent pattern of vertical deformation extending southwest of the rupture trace, as well as faint signal in northings and eastings. High uncertainty of the LiDAR data relative to the moderate coseismic surface displacements expected for an M_w 5.1 earthquake also results in a low SNR of the LiDAR measurements.

The fact that both interferograms are from similar viewing geometries, along with the low SNR of all available data, led to challenges that are not typically present when interpreting and inverting coseismic surface deformation. Regarding interpretation, the low amplitude and spatial extent of the deformation signal means artefacts in the digital elevation model (DEM), high contrasts in the strength of reflectors contained in neighboring resolution cells (*e.g.*, Xu *et al.*, 2019; Sauer *et al.*, 2011), and effects such as layover and foreshortening from reflectors with a large radar cross section (RCS), which are typically mitigated by multiple viewing geometries, must be considered (*e.g.*, Liang *et al.*, 2021; Sauer *et al.*, 2011). Regarding inversion, common issues, such as over-fitting of noise and lack of observations over the full 3-D displacement field, become amplified to a degree such that standard inversion methods may no longer be effective. As a result of these limitations, more care is needed when evaluating the observations for spurious signal and methods that are more robust to noisy and/or incomplete data should be employed.

To overcome the aforementioned obstacles, we turn to the field of compressed sensing, specifically sparse source recovery methods. In general, the aim of compressed sensing is the recovery of a source or signal from limited and/or noisy measurements (*e.g.*, Boche *et al.*, 2019; Donoho, 2006), where sparse source recovery seeks to find models which retain the

minimum number of parameters required to reconstruct the observed signal. We opt for the use of graph-guided fused LASSO (GGFL) (*e.g.*, Tibshirani *et al.*, 2004; Tibshirani, 2018; Chen, Kim, *et al.*, 2010), a method that combines LASSO and total-variation regularization in the prior. Even with the less than ideal state of the interferometry, we are able to determine that the Sparta earthquake involved shallow oblique slip on a SW dipping fault, a solution which is consistent with the focal mechanism solutions.

2.2 Data

We use two interferograms, one from the European Space Agency's Sentinel-1A/B (S-1A/B) platform (see Data and Resources) and one from the Japan Aerospace Exploration Agency's Advanced Land Observing Satellite 2 (ALOS-2). Radar scenes from both satellites covering the epicentral region and within a year of the earthquake are only available from ascending passes, and thus viewing geometries for both are very similar (the average incidence angles of S-1A/B and ALOS-2 are 35° and 39°, respectively). To form the Sentinel coseismic interferogram, which we refer to as S-1, we used an S-1A acquisition on 08 Aug 2020 as the reference and an S-1B acquisition on 14 Aug 2020 as the secondary. We used the ALOS-2 coseismic interferogram published by Wicks and Chiu (2022), which was based on acquisitions made on 12 Oct 2019 and 10 Oct 2020. The time spans for the S-1 and ALOS-2 inteferograms are six days and just over a year, respectively.

We use GMTSAR (Sandwell *et al.*, 2011) to calculate the S-1 interferogram, and the details of the processing of the ALOS-2 data can be found in Wicks and Chiu (2022). We low-pass filter the wrapped S-1 scene using a Gaussian filter with a 150 meter wavelength, decimate at 8 pixels in slant range by 2 pixels in azimuth, and then apply a Goldstein adaptive filter (Goldstein and Werner, 1998) with an exponent of 0.5 and patch size of 32 by 32 pixels. We then unwrap phase using SNAPHU (Chen and Zebker, 2002) with a coherence threshold of 0.1, allowing for phase discontinuities of up to 28 cm in the final unwrapped phase to avoid smoothing over the discontinuities associated with the surface rupture.

The first order features of both interferograms are consistent with each other, both having similar spatial extent and showing primarily away-from-satellite, negative line-of-sight (LOS) deformation to the southwest and towards-satellite, positive LOS deformation to the northeast of the surface rupture (Fig. 2.2A & 2.2B). The LOS offsets SW of the rupture trace indicate subsidence and/or eastward motion (note that due to the near-polar orbit of the InSAR satellites, InSAR has negligible sensitivity to north-south ground motion), while NE of the trace the LOS offsets indicate uplift and/or westward motion. If the LOS offsets are interpreted to be purely vertical, the interferometric measurements are broadly consistent

with either normal slip on a SW dipping fault, or reverse slip on a NE dipping fault. On the other hand, if the LOS offsets are interpreted to be purely horizontal they would indicate either left-lateral fault slip or reverse slip on a fault with either SW or NE dip, respectively. However, it is more likely that the LOS range change results from a combination of both vertical and horizontal (based on the incidence angles of the satellites, the sensitivity of vertical to horizontal motion is about 4:3). That the magnitude of LOS range change decreases toward the fault trace suggests that uplift and horizontal motion away from the satellite tracks cancel each other out to some extent, motion that is consistent with reverse slip on a SW dipping fault.

The interferograms also exhibit two regions of positive LOS offsets along, and on the southwestern side of the Sparta earthquake trace (indicated by the blue polygons in Figs. 2.2A & 2.2B). These positive LOS areas are more pronounced in the ALOS interferogram (*c.f.*, Figs. 2.2A & 2.2B), with the region near the southeastern end of the fault trace in the ALOS interferogram being the strongest. The positive LOS offsets are coincident with the locations of several industrial parks, consisting of large warehouses and other structures (Fig. A.1). We return to the possible effect of the built environment on the interferograms in Subsection 2.2.1.

In order to reduce the number of LOS measurements to a computationally feasible size, we down-sample the interferograms using a saliency-based quadtree sampling (SQS) algorithm (Gao *et al.*, 2021). The concept of image saliency is taken from computer vision and enables the identification of the most prominent or salient features of an image. The advantage of SQS for InSAR sampling is that it allows for the identification and separation of near-field and far-field information while simultaneously mitigating over sampling of noise. The mean displacement and propagated uncertainty for each sample from the resulting down-sample are retained for modeling of coseismic slip. The final sample sizes are 458 and 361 for the S-1 and ALOS-2 interferograms respectively (Fig. A.2).

We assume the phase covariance matrix $\mathbf{C} = \mathbf{C}_\varphi + \mathbf{C}_s$, where $\mathbf{C}_\varphi$ represents a spatially independent decorrelation of phase, and $\mathbf{C}_s$ is a spatial dependent component (*e.g.*, Hanssen, 2001). Once orbital and topographic phase errors are corrected, the spatially correlated component consists primarily of tropospheric phase contributions. To abate issues of any residual orbital and topographic errors in the interferograms, as well as to account for tropostatic phase contributions (*e.g.*,Tarayre and Massonnet, 1996; Emardson *et al.*, 2003), we use the composite error removal method of Xu *et al.* (2014), which has the effect of reducing $\mathbf{C}$ to just $\mathbf{C}_\varphi$, which can be modeled stochastically and estimated from coherence (Hanssen, 2001).

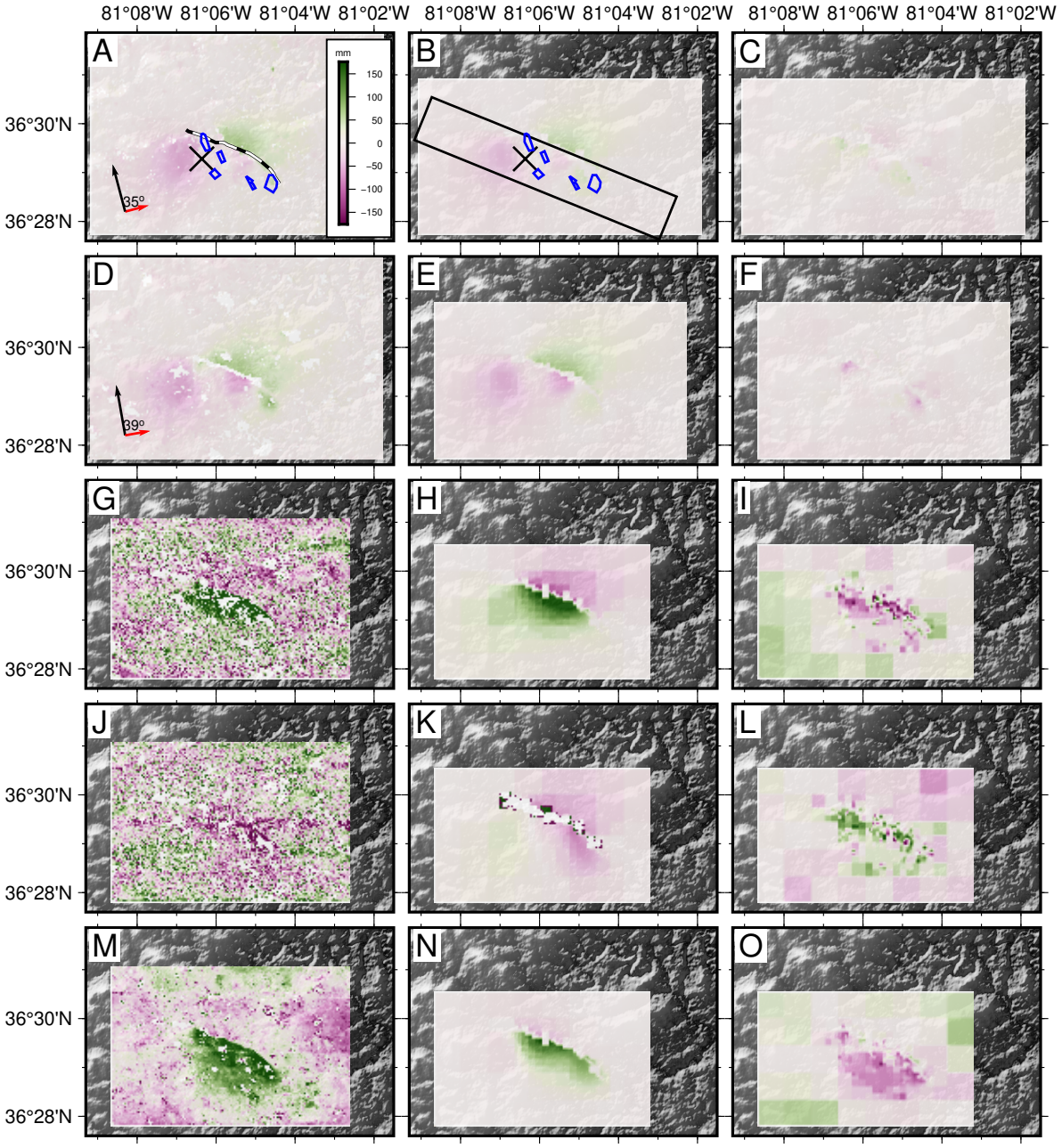


Figure 2.2: ALOS-2 (A) and S-1 (D) interferograms, and LiDAR ICP X (G), Y (J), and Z (M) components. Panel (A) and (B) contain a cross indicating the centroid, blue polygons outlining prominent industrial parks in the interferogram footprint, and line indicating the field mapped surface rupture (A) (Figueiredo *et al.*, 2022) or a black rectangle indicating the surface projection of the modeled fault edges (B). Black arrows indicate the satellite azimuth and red arrow indicates the average look vector, with number indicating the average look angle from vertical. Synthetic interferograms for ALOS-2 (B) and S-1 (E), and LiDAR components X (H), Y (K), and Z (N), and the residuals (C), (F), (L), (I), and (O) respectively. The colorbar in panel (A) is common to all images.

2.2.1 Impacts of the built environment on the interferograms

Change detection is reliant on the ability to capture an accurate representation of the surface of interest at a given moment in time. For InSAR interferometry, an accurate representation of surface deformation is achieved by first removing several other contributions from the total recorded phase. Of particular interest here is the topographic contribution to total phase, the removal of which requires use of a DEM. The standard procedure is to produce synthetic topographic phase values from a given DEM, typically SRTM data, and then subtract the synthetic phase from the total phase. However, due to the coarse 90 m resolution of the SRTM DEM, many structural details may not have been captured (*e.g.*, Gamba *et al.*, 2002), and when they were, the height of structures were likely severely underestimated (*e.g.*, Misra *et al.*, 2018). In contrast, ALOS-2 is capable of 3–6 m resolution, significantly increasing the likelihood of capturing a more complete morphology of structures present in the SAR footprint. The discrepancy between the resolution of the interferogram and DEM likely results in residual topographic phase corresponding to large structures remaining after a topographic correction has been applied, which will manifest as erroneous toward-satellite signal in the interferogram (*i.e.*, positive LOS offsets). This spurious toward-satellite signal can be further exacerbated by a side lobe effect, whereby reflectors with a high RCS and/or high reflection coefficient are in close proximity to reflectors with a small RCS and/or low reflection coefficient. If this occurs the high side lobes of high-intensity scatterers contained in a resolution cell interfere with, and overpower, the lower main lobes of weaker scatterers contained within neighboring cells (*e.g.*, Xu *et al.*, 2019; Liang *et al.*, 2021; Sauer *et al.*, 2011). This side lobe effect results in spatially diffusing signal from high-intensity scatters.

Issues in interferograms arising from the lower DEM resolution and side lobe effects are mitigated by having multiple interferograms with both ascending and descending passes, and the effects are likely to be negligible when imaging larger earthquakes with higher SNR (*i.e.*, earthquakes producing larger amplitude and spatial extent of surface deformation). In the case of the Sparta earthquake, both effects are likely pertinent to an interpretation of the interferograms. As there are several industrial parks located along a local highway (Fig. A.1), coincident with the positive LOS offsets along the SW of the fault trace, we believe these toward-satellite signals may be anomalous. We explore the effect of including or neglecting this potentially anomalous signal in the coseismic slip models we develop below.

2.2.2 LiDAR

Two LiDAR surveys conducted by the USGS bracket the Sparta earthquake (see Data and Resources), with the first collected in 2016, over the period of 27 February to 12 April, as a

routine regional survey. The post-earthquake survey was conducted 12–14 December 2020, specifically to survey surface deformation caused by the Sparta earthquake. The 2016 pre-earthquake survey was collected in gieger mode with a pulse repetition frequency (PRF) of 50 kHZ achieving an average point density of 36.62 pts/m^2. The 2020 post-earthquake survey was collected in linear mode with a PRF of 1000 kHZ achieving a point density of 90.85 pts/m^2 along the rupture area. We retain only the last returns from both point clouds, which are assumed to represent the ground surface reflections. We also perform statistical outlier removal which uses global statistics to first establish a threshold value and then remove any data points exceeding that threshold (*e.g.*, Rusu *et al.*, 2008). Our 3D topographical differencing is conducted using software provided by Open Topography (Scott, 2020), which uses a windowed implementation of the iterative closest point (ICP) algorithm to align and estimate differences between point clouds (Scott *et al.*, 2018; Besl and McKay, 1992; Nissen *et al.*, 2012; Chen and Medioni, 1992). The data are processed using a window size and grid spacing of 32 m as prescribed in Scott *et al.* (2021) for processing ground-return-only data sets. Point cloud misalignment penalization was estimated using point-to-plane errors. While we are able to recover information for all three components, deformation signal was significantly more coherent in the vertical component with the horizontal components containing only weak signal in close proximity to the fault trace. The less robust signal in the horizontal components may be the result of the low relief of the surrounding landscape relative to the window size used (*e.g.*, Glennie *et al.*, 2014; Lajoie *et al.*, 2019). Uncertainties for the ICP components are estimated from the 24 nearest-neighbor grid nodes on the same side of the fault, where vertical uncertainties are calculated using the standard deviation and the horizontals are calculated using a PCA analysis (Scott *et al.*, 2018). The LiDAR deformation fields are then down-sampled in a similar manner to the interferograms. However, in this case a quad-tree sampling is constructed using only the vertical component as it is most coherent, and the horizontal components are sampled using the resulting tree (Fig. A.2). Since we are inverting for a planar fault which fails to account for the more complex fault trace, we do not consider samples associated with tree nodes intersected by the fault trace.

The vertical component of the LiDAR data SW of the fault trace consistently indicates uplift, and does not have clear variations coincident with the identified industrial parks (Fig. 2.3A). This suggests that the variations in InSAR data SW of the trace are either purely horizontal motion or are indeed due to residual errors in the processing, as discussed in the previous section. The horizontal components of the differential LiDAR SW of the fault trace show a significant amount left-lateral strike-slip motion, further corroborating the interferogram interpretation. The horizontal displacements to the NE of the fault trace

show primarily reverse motion along the central region of the fault trace, and left-lateral strike-slip motion the ends of the trace.

It is worth noting that tree groves present in the vicinity of the Sparta earthquake may be of concern (Fig. A.1); while it is often assumed that the LiDAR last return in vegetated regions represents the ground surface, it is more precise to say in areas with significant vegetation and/or ground cover the last return represents the maximum penetration depth of the LiDAR laser, and accuracy may only be sub-meter (*e.g.*, Reutebuch *et al.*, 2003; Crow *et al.*, 2007; Vega *et al.*, 2016). The maximum observed coseismic displacement from the Sparta earthquake is ∼20cm, consistent with expectations for an earthquake of this size, and thus on order of the LiDAR accuracy for highly vegetated areas. Much of the area local to the Sparta earthquake is composed of mixed forested areas, farm fields, and industrial parks. A lower density of both trees and ground cover lends itself to more accurate surveying within the farm fields when compared to the forested areas. The industrial parks have more noise in the form of vehicular traffic, changes in structures, and placement of materials, all sources of potential noise not present in the areas occupied by fields. A large portion of the most significant surface rupture occurred in several farm fields, therefore deformation in the LiDAR data within this area likely captures the coseismic ground deformation.

2.3 Inverse Methods

Geodetic observations of coseismic surface displacements are routinely used to estimate fault geometry and the patterns of fault slip at depth. The most common approach is to assume that surface displacements, $\mathbf{d}$, are the result of fault slip on sub-faults, each with uniform slip, in a homogeneous elastic half-space. This assumption allows one to use analytic Green's functions, $\mathbf{G}$, from, for instance, Okada (1985) and Evans and Meade (2012). This gives rise to the system $\mathbf{G}(\mathbf{m}) = \mathbf{d}$, which is inverted for slip on the sub-faults, $\mathbf{m}$. In an elastic media, $\mathbf{G}$ is linear with respect to the slip on the sub-faults, while it is non-linear with respect to the geometry of those sub-faults. Estimating all of the model parameters simultaneously can be costly, due to the non-linearity of some of the parameters (*e.g.*, Minson *et al.*, 2013). To avoid that cost, researchers commonly first assume that coseismic slip is uniform on a planar fault, and use some flavor of Monte Carlo search to estimate the geometric parameters of that fault, including location, dip, strike, and dimensions (*e.g.*, Clarke *et al.*, 1997). Once an optimal fault plane geometry is found, it is divided into a collection of sub-faults, fixing the location, strike, and dip, and then determining the distribution of slip across those sub-faults via a linear least squares inversion. While computationally efficient, this approach assumes that the optimal fault geometry obtained assuming uniform fault slip is also the optimal fault

geometry when allowing for non-uniform fault slip. For instance, He *et al.* (2017) found that the optimal fault geometry of the 2016 M_w 7.8 Ecuador earthquake obtained assuming uniform fault slip was unlikely to be the correct fault geometry, due to that geometry's mismatch to the mapped megathrust. Moreover, when He *et al.* (2017) inverted for the spatial pattern of slip on a fault with a geometry fixed to the megathrust, they obtained a better fit to the data than they achieved using the geometry from the initial search. Wicks and Chiu (2022) also recognized the limitations of assuming uniform slip in the initial non-linear search for fault geometry, and proposed using a prescribed functional form to describe a smooth slip distribution in the search for fault geometries. Here we linearly invert for the distribution of slip for each of the fault geometries tried in a Monte Carlo search over the fault geometry parameters, without prescribing any functional form that that slip distribution needs follow outside of regularization constraints in the inversion, which we address below.

The challenges presented by limited data availability and the low SNR of the data we consider make the inversion for coseismic slip in the Sparta earthquake an ideal candidate for sparse model recovery methods developed in the field of compressed sensing. We opt to use GGFL, which incorporates both LASSO and smoothness constraints. The GGFL objective function is

$$J\left(\mathbf{w}, \lambda_1, \lambda_2\right) = \sum_{s \in V} (y_s - w_s)^2 + \lambda_1 \sum_{s \in V} |w_s| + \lambda_2 \sum_{(s,t) \in E} |w_s - w_t| \,, \tag{2.1}$$

where V and E are the sets of graph vertices and edges respectively (*e.g.*, Murphy, 2012; Tibshirani *et al.*, 2004). When applied to a 2D lattice prior, the objective function can be written as,

$$\hat{\mathbf{m}} = \min_{\mathbf{m}} \left\{ ||\mathbf{G}\mathbf{m} - \mathbf{d}||_2^2 + \lambda_1 \left|\left|\mathbf{m}\right|\right|_1 + \lambda_2 \left|\left|\nabla \mathbf{m}\right|\right|_1 \right\}, \tag{2.2}$$

where λ_1 and λ_2 are penalty parameters associated with the LASSO constraint ($\left|\left|\mathbf{m}\right|\right|_1$) and the ℓ_1 of the model gradient ($\left|\left|\nabla \mathbf{m}\right|\right|_1$), respectively. The application of both constraints promotes sparse, smooth model solutions (*e.g*, Murphy, 2012). The LASSO constraint promotes sparsity by placing slip on the minimum number of patches required to reproduce the observed displacements (*e.g.*, Tibshirani, 2018; Evans and Meade, 2012), which can be viewed as seeking more parsimonious model solutions. In general, model sparsity through LASSO is achieved by imposing a Laplacian prior on the model in contrast to the ℓ_2 or Gaussian prior imposed by the more common ridge constraint. The Laplacian operator enforces the "fused" aspect of the resultant models by restricting variability in the component-wise slip of neighboring patches. This provides model solutions that are smooth in both rake and slip

magnitude, while also reducing areas of anomalous or disconnected slip. This smoothing effect can cause a decrease in the sparsity of the estimated model, but slip outside of the of the main rupture area is typically negligible.

The GGFL objective function requires the estimation of two penalty parameters. For the first, λ_1, following Miller (1970), we use an *a priori* estimation that is informed by the data uncertainties, sub-fault area, and seismic moment. Calculating λ_1 *a priori* significantly reduces computational burden. Briefly,

$$\lambda_1 = \frac{\delta}{\alpha} \tag{2.3}$$

where δ is related to data error, $||\varepsilon||$, and α is related to model size, $||\mathbf{m}||_1$. In our case, $\mathbf{m}$ contains only slip components, as nuisance parameters are solved and removed during data processing. An estimation for λ_1 can be found by assigning values to δ and α that satisfy the relations,

$$||\varepsilon|| \leq \delta \text{ and } ||\mathbf{m}|| \leq \alpha, \tag{2.4}$$

where values for α and δ need not be exact, but only reasonable estimations. Our estimations are given by,

$$\delta \approx ||k\sigma_{LOS}||_2 \text{ and } \alpha \approx \frac{\sqrt{2}M_0}{\mu A}, \tag{2.5}$$

where k is used to scale how conservative an estimation is, μ is the shear modulus, and A is the sub-fault area. Note, this does not force the model to match the seismic moment and only serves to penalize coseismic slip models more severely as the model moment exceeds the observed seismic moment. The second, λ_2, is associated with the model gradient constraint and is estimated using the L-curve criterion. We use the L-curve criterion of Hansen (2000) because it is more robust to spatially correlated data then other penalty parameter estimation methods.

We assume a single, planar slip surface. Recognizing that a single plane assumption is a simplification of faulting, we kept open the possibility of segmenting the plane into several connected planes, or adding additional planes, although we did not see anything in the model residuals that suggests such model complexity is warranted. Based on the surface rupture prominent in the interferograms (Fig. 2.2A and 2.2D), we fix the strike of the fault plane at 111°. The center of the trace is fixed at the middle of the surface rupture. The fault plane extends 5 km along-strike from the midpoint in both directions and has a down-dip width of 4 km. We discretize the fault plane into 0.2 km by 0.2 km sub-faults. With the location and strike of the fault fixed, we use a Monte Carlo search over dip, considering any dips ranging from southwest dipping to northeast dipping, including perfectly horizontal. We then solve

for the distribution of slip across the sub-faults via GGFL for every fault dip considered in the Monte Carlo search. To evaluate the fit between candidate models and the observations we use the root mean squared error (RMSE) of displacement, considering only the down sampled data used for model estimation, to quantify the misfit of each slip model.

2.4 Results

We present five coseismic slip models in total, referred to as CSM-S1, CMS-FULL, CSM-DAR, CSM-LiDAR, and CSM-JOINT. CSM-S1 is based on only the S1 interferogram, while CSM-FULL is based on both the S1 and ALOS-2 interferograms. CSM-DAR uses both interferograms, but masks data associated with the industrial parks, as discussed above. CSM-LiDAR is based only on the LiDAR data, and CSM-JOINT is based on all data, with the industrial parks masked from the interferometric data. CSM-JOINT is our preferred model, for reasons that will be expanded on in the Discussion section.

All of the coseismic slip models are characterized by oblique-reverse slip on a SW dipping fault, with compact slip primarily in the upper 1.5 km (Figs. 2.3A-E). In the models constrained by only InSAR, coseismic slip is composed of largely left-lateral strike-slip motion at depth and oblique reverse motion near the surface. The slip in CSM-S1 is more compressed near the surface compared with the models estimated using the additional ALOS data (*cf.*, Fig. 2.3B), with the coseismic slip all shallower than about 0.5 km (Table 2.1). Slip in CSM-FULL and CMS-DAR extends further to the southeast compared in CSM-S1, with near surface, right-lateral slip that is quite a bit more prominent in CSM-FULL than in CSM-DAR. The dip of CSM-FULL is 41° with an M_w of 4.99, assuming a shear modulus of 30.0 GPa (Table 2.1). CSM-DAR has a slightly steeper fault, with a dip of 50° (Fig. 2.3C), and M_w of 4.93. CSM-S1 has an even steeper dip of 60°, and lower M_w of 4.70. In contrast to the InSAR models, CSM-LiDAR (Fig. 2.3D) is composed largely of reverse motion at depth, and left-lateral strike-slip motion near the surface. The majority of the high amplitude slip is restricted to the upper 0.5 km in CSM-LiDAR, and is mainly localized in a region composed of left-lateral slip. CSM-LiDAR has a dip of 49°, and M_w of 5.01. CSM-JOINT has a significantly smoother distribution of slip than any of the other models (Fig. 2.3E) , with a dip of 50° and M_w of 5.08, the closest to the seismic moment of all coseismic slip models developed. Slip in CSM-JOINT is predominantly oblique, with a region of more left-lateral motion on the southeast of the fault plane and more reverse to the northeast and at depth (Fig. 2.3E).

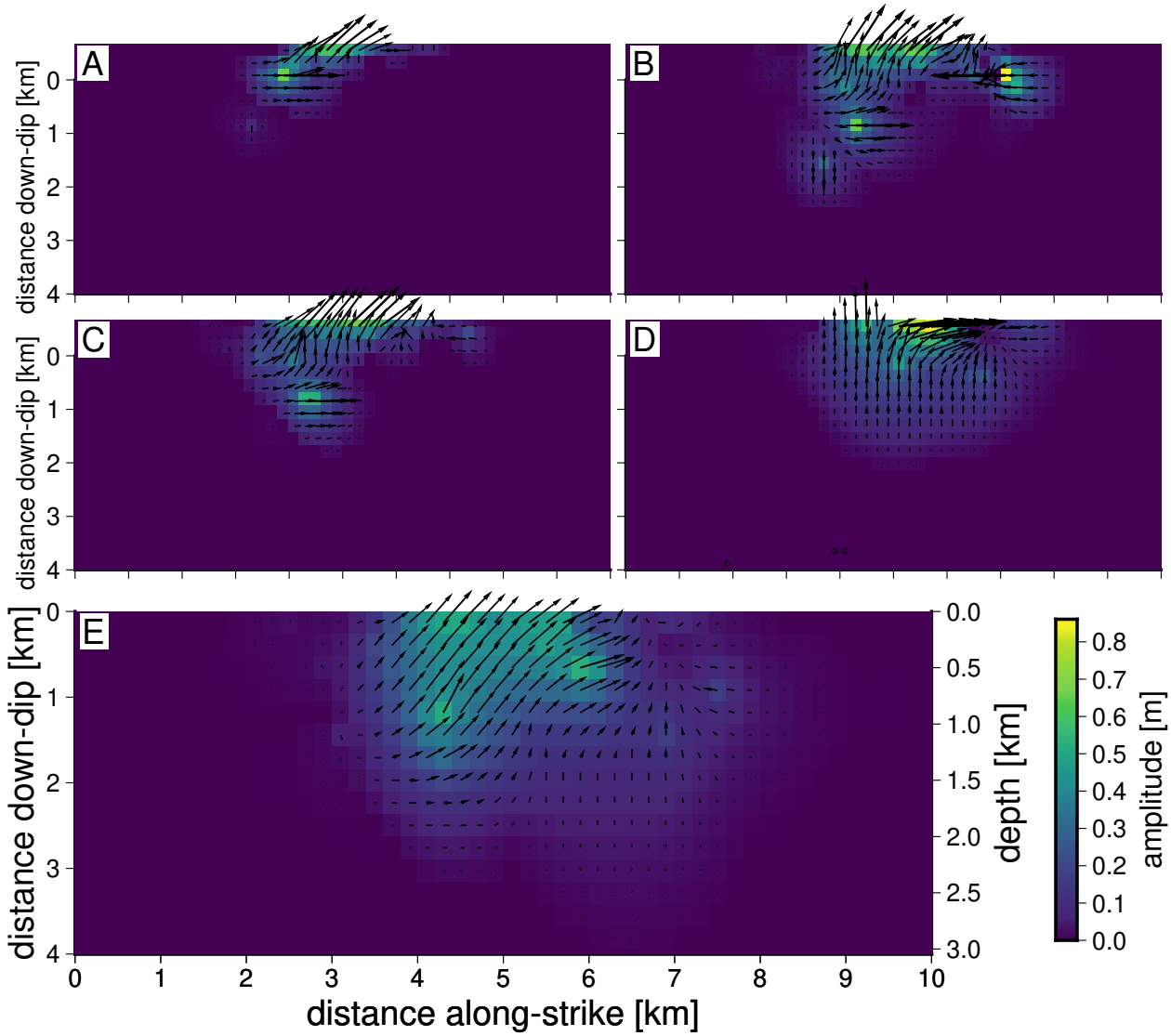


Figure 2.3: Slip distributions for CSM-S1 (A), CSM-FULL (B), CSM-DAR (C), CSM-LiDAR (D) and CSM-JOINT (E), with black arrows indicating the slip vector on each subfault, and colors indicating the magnitude of slip. The color bar and along-strike distance is common to all panels.

model	λ_1	λ_2	dip	avg. rake	$RMSE_{\text{InSAR/LiDAR/Full}}$	M_w	$\overline{\Delta\sigma}$ [MPa]
CSM-S1	0.956	0.004	60°	21°	0.0242/0.1110/0.0734	4.70	12.4
CSM-FULL	1.899	0.024	41°	45°	0.0112/0.0956/0.0618	4.99	7.3
CSM-DAR	1.889	0.024	50°	49°	0.0197/0.0988/0.0650	4.93	8.1
CSM-LiDAR	1.692	0.031	49°	67°	0.0364/0.0914/0.0648	5.01	11.7
CSM-JOINT	1.713	0.026	50°	50°	0.0143/0.0841/0.0549	5.08	5.9

Table 2.1: Optimal penalty parameters, λ_1 and λ_2, used in the inversion for the three coseismic slip models, fault dip, the average rake weighted by the slip magnitude, RMSE associated with the InSAR, LiDAR, and full data sets, and estimated stress drop, $\overline{\Delta\sigma}$ (see Electronic Supplement for calculation of $\overline{\Delta\sigma}$) for each of the coseismic slip models.

2.5 Discussion

2.5.1 Preferred model

Our coseismic models are built on an assumption of a homogeneous elastic half-space with a flat free surface, which is admittedly a crude simplification of Earth. Often times the inclusion of a lower-rigidity layer in the construction of $\mathbf{G}$ can result in differences in the estimated fault slip distributions compared to using a half-space solution (*e.g.*, Savage, 1998; Hearn and Burgmann, 2005; Ragon and Simons, 2020). However, the moderate magnitude and shallow depth of the Sparta earthquake likely makes the addition of such layering unnecessary (*e.g.*, Cattin *et al.*, 1999). With regards to our use of a flat free surface, the topography in the foothills of North Carolina is composed of rolling hills, while the effects of topography on coseismic slip models are most apparent with high topographic gradients (*e.g.*, Langer *et al.*, 2020). We also note the relatively small footprint of this earthquake, compared to larger earthquakes where coseismic deformation can extend on order of 100 kilometers, earthquakes in which the half-space approximation is routinely used. For these reasons we opted to forgo the inclusion of topography in our modeling, benefiting from the computation ease of the half-space models.

All of the coseismic slip models are successful at describing the interferograms to varying degrees, with more limited success describing the LiDAR data. The latter is likely due to the higher uncertainty associated with the LiDAR data itself. It's worth noting, however, that CSM-JOINT surprisingly fits the LiDAR data better than CSM-LiDAR does (Table 2.1). With the exception of CSM-FULL, CSM-JOINT explains more of the InSAR data than other models, the larger misfit of CSM-JOINT relative to CSM-FULL can be attributed to the data coincident with the industrial parks being ignored, which is expected as CSM-JOINT did not seek to describe this data.

The shallow, thrust-dominated slip distribution of CSM-S1 under-estimates the magnitude by an appreciable amount (Table 2.1), and contains insufficient left-lateral slip to match the rake predicted by the Saint Louis University Earthquake Center (SLU) moment tensor solution. CSM-FULL is in closer agreement to the observed magnitude than CSM-S1 (Table 2.1); however, CSM-FULL contains two prominent regions of right-lateral or normal slip, opposite of the sense of slip over the majority of the fault (Fig. A.3B). Those spurious slip patches are absent in CSM-DAR (Fig. A.3C), owing to the fact that CSM-DAR neglects the interferometric data associated with the industrial parks, and has a moment closer to the seismic moment. While CSM-LiDAR has a dip and magnitude in close agreement with the SLU moment tensor solution, it contains an excess of left-lateral slip, significantly over-estimating the SLU derived rake. CSM-JOINT is consistent with both the moment magnitude and the SLU focal mechanism rake. Interestingly, CSM-JOINT fits the interferometric and LiDAR data better than CSM-DAR and CSM-LiDAR, respectively. For these reasons, we prefer CSM-JOINT as the closest representation to the true slip in the Sparta earthquake.

Using the average rake, weighted by the slip magnitude, we can construct a double couple representation of CSM-JOINT, which is quite close to the SLU focal mechanism (Fig. 2.4A). Through our Monte Carlo search over the fault dip, all estimated models are retained and can be interrogated to assess the variability in the model. Here, we consider all models that had a RMSE model fit that was no larger than 1.5% larger than the best model. While this limit is quite arbitrary, it sufficiently captures model solutions representative of the neighborhood around the best-fit model solution. For each of those models, we compute the average weighted rake, and thus a focal mechanism representation of that model, which are shown in Fig. 2.4A.

CSM-JOINT predicts an offset at the GNSS station NCSR of 20.5 mm in the direction 47° from North (14 mm eastward and 15 mm northward). The cosesimic offset estimated from the NCSR time series is 13.5 mm, 55° from North (Fig. A.8 in the electronic supplement). Although the predicted azimuth of the offset is comparable to that detected by NCSR, the magnitude is nearly twice as large. In contrast, the predicted offset from the coseismic model of Wicks and Chiu (2022) is roughly perpendicular to the NCSR offset (see Fig. 3A in their paper). As indicated above, NCSR is located on top of a multistory building that was damaged in the earthquake (Wicks and Chiu, 2022), and thus we do not give the fit between our predicted offet and that estimated from NCSR data much credence.

The inclusion of the LiDAR data results in a smoother slip distribution relative to when constrained only by InSAR data (Fig. 2.3). The smoother distribution is likely due to more robust near-surface slip in CSM-LiDAR, in contrast to CSM-DAR where the majority of the near-surface slip is constrained to the top layer of sub-faults. Despite the fact that

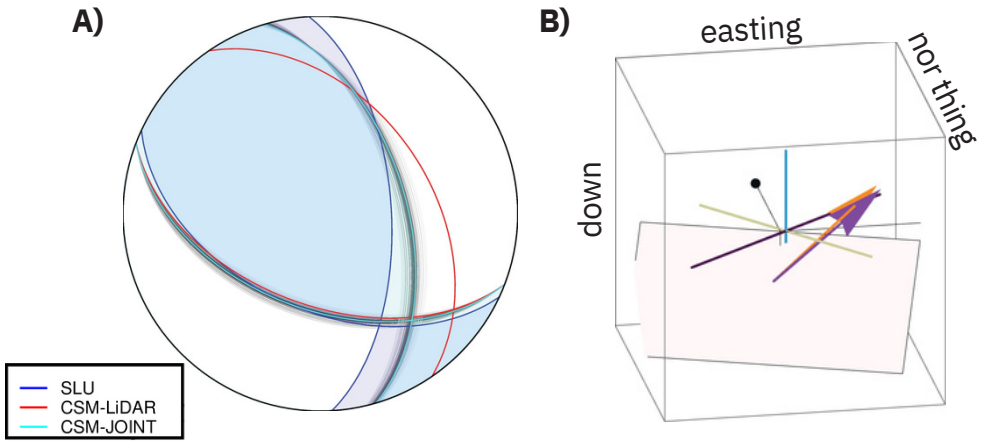


Figure 2.4: (A) The Saint Louis University focal mechanisms (P quadrant shaded light purple and nodal planes depicted with blue lines), with the nodal planes associated with our preferred coseismic slip model CSM-JOINT (cyan lines, thin gray lines depict ensemble of models with misfit up to 1.5% higher than CSM-JOINT) and those associated with the coseismic slip model estimated from the LiDAR data alone (red lines). (B) Perspective view of the fault in CSM-JOINT from the SSW (thin black line with finial sphere is pointing North, and thin black line with no finial is pointing East), and the average slip vector in CSM-JOINT (orange arrow). The most, intermediate, and least compressive stresses (purple, tan, and blue lines, respectively), assuming that the most compressive stress is aligned with Sh_{max} from the World Stress Map (Heidbach *et al.*, 2016, 2018) and that least compressive stress is vertically oriented. Also shown is the direction of the maximum fault shear stress (plum colored arrow) for this orientation of principal stresses.

CSM-LiDAR contains two distinct patches at the top of the fault, with nearly pure thrust or left-lateral slip, CSM-JOINT is characterized by oblique thrust slip at the top of the fault, similar to the near-surface slip rake in CSM-DAR. This suggests that, at least with these data, the InSAR is largely constraining the slip rake even at shallow depths. CSM-LiDAR contains some deeper slip (at about 1 km down-dip from the surface, slightly to the right of the near-surface slip seen in Fig. 2.3D), which is not contained in CSM-DAR, but is retained in CSM-FULL. This suggests that both the LiDAR and InSAR data are sensitive to coseismic slip at these depths using our GGFL estimation scheme. (Scott *et al.*, 2019) found that LiDAR data from the M_w Kumamoto, Japan, earthquake was more sensitive to slip at shallow depths, while the InSAR was more sensitive to deeper slip. Their finding which might seem contradictory to what we find here, although, it is important to note that the Kumamoto earthquake slip extended 10 km or more, whereas coseismic slip in Sparta is entirely constrained to depths not exceeding 2 km. Moreover, the interferograms considered by (Scott *et al.*, 2019) and here were downsampled at entirely different resolutions.

2.5.2 Comparison to coseismic model model of Wicks and Chiu (2022)

All of our coseismic slip models are in stark contrast to the model of Wicks and Chiu (2022). In part, the motivation for including a normal fault in their model was the attribution of away-from-satellite LOS motion to the southwest of the fault trace to vertical subsidence, making it inconsistent with thrusting and necessitating the introduction of the normal fault. However, our single fault coseismic slip models demonstrate that oblique slip, composed of left-lateral and reverse motion, are sufficient to explain the observed LOS offsets. As for the introduction of the second reverse fault by Wicks and Chiu (2022), it is heavily reliant on the region of positive LOS offsets on the southwest side of the trace, within a region that is characterized by predominantly negative LOS offset (Fig. A.2B). We suggest that this patch, along with several other areas, are composed of spurious signal related to the presence of industrial parks, and is not the result of coseismic deformation. When these data are removed, as was done in developing CSM-DAR and CSM-JOINT, the estimated fault geometry and fault motion agree with other independent observations much more than CSM-FULL or the model of Wicks and Chiu (2022), both of which included these suspect data in the estimation.

2.5.3 Consistency of coseismic slip model with tectonic stress

Coseismic slip models of moderate to large magnitude earthquakes are often characterized by complicated patterns of that slip, with both rake and slip magnitude varying across the slip surface (*e.g.*, Feng *et al.*, 2010; Simons *et al.*, 2002). In contrast, images of coseismic slip for smaller magnitude earthquakes are are often characterized by a single "bulls-eye" of coseismic slip (*e.g.*, Lohman and Simons, 2005). It is worth noting that estimation of coseismic slip is routinely regularized by just minimizing the curvature of the spatial slip pattern, which might result in actual slip variations being smoothed over when inverting small magnitude surface displacements. As we demonstrate, using an inversion technique that is better suited to data with low SNR, variations of rake and slip magnitude across the fault, if present, may be resolvable even for moderately small earthquakes.

On average, the inferred coseismic slip rake in CSM-JOINT is consistent with what is known of the regional stress field. The World Stress Map (WSM; Heidbach *et al.*, 2016, 2018) indicates that SHmax is approximately 111° in the vicinity of the Sparta earthquakes. Assuming that SHmax is the orientation of the most compressive stress direction, MCS, and that the magnitudes of the intermediate and least compress stresses, ICS and LCS, respectively, are equal, the rake of the maximum shear stress on the fault plane is about 48° (additional details given in the Electronic Supplement). As the magnitude of the ICS increases and assuming vertical LCS, the rake of maximum shear stress on the fault increases. In the extreme case where the magnitudes of the MCS and ICS are equal, the rake of the maximum shear stress is 90°, as faults of any strike within that plane stress state would be stressed purely in reverse manner. Assuming that when a fault fails it slips, on average, in the direction of the maximum pre-seismic stress resolved on that slip surface, the WSM predicted angle of maximum shear stress is quite consistent with the average rake of 50° in CSM-JOINT, particularly when the ICS magnitude is more similar to the LCS magnitude.

Motivated by the consistency of WSM-derived direction of maximum fault shear stress and the average coseismic slip rake, we explore the consistency of CSM-JOINT with models of stress. We consider stress models varying from thrust regime to strike-slip regime (*i.e.*, with LCS varying from vertical to horizontal), with varying relative magnitudes of ICS to the magnitudes of MCS and LCS. We follow the method of Walbert and Hetland (2022), which estimates pre-earthquake stress tensor from coseismic slip models, assuming that WSM SHmax indicates the MCS orientation. We additionally add the constraint that the magnitude of the MCS, σ_{M}, is sufficient to generate a shear stress on the CSM-JOINT fault plane at least as large as the estimated coseismic shear stress drop, which is to say that the fault shear stress is fully to partially relieved by the Sparta earthquake. To estimate the stress drop we use a Brune model (*e.g.*, Scholz, 2019; Brune, 1970; Noda *et al.*, 2013,

assuming that fault slip is over a square fault patch (see details in the Electronic Supplement), noting that these assumptions are rough approximations of CSM-JOINT. The stress drop, $\overline{\Delta\sigma}$, we calculate for CSM-JOINT is about 6 MPa (Table 2.1), in-line with stress drops resolved by Huang *et al.* (2017) for eastern US earthquakes. Finally, to account for the fact that rake varies from strike-slip (0° rake) to reverse (90° rake) in CSM-JOINT, we quantify the match between a given stress model and the slip in CSM-JOINT using a von Mises likelihood function with concentration 9.9 (Fig. A.9A).

We find that to be consistent with our image of the Sparta earthquake, σ_{M} has to be larger than 15 MPa (Fig. A.9B). Note that the lower bound of σ_{M} does not rely on any assumption of coefficient of friction, and corresponds to the case when an 6 MPa stress drop relieves the full accumulated shear stress on the fault. The expected lithostatic stress at the centroid depth is about 26.5 MPa (see Electronic Supplement for more details), which overlaps the posterior probability density function of σ_{M} at the lower end (Fig. A.9B); however, it is important to note that the lower bound is highly dependent on the estimated stress drop, for instance assuming a 10 MPa stress drop, the lower bound on MCS increases to about 28 MPa, slightly larger than the expected lithostatic stress (Fig. A.9B).

While a lower bound of σ_{M} of 20–30 MPa is not particularly informative about the stress level in the Sparta region, that the bound is similar to lithostatic stress suggests that the assumption of SHmax indicating the MCS orientation is reasonable. The stress tensors consistent with CSM-JOINT are characterized by a near Andersonian thrust regime, with the LCS rotated off of vertical less that about 40° (Fig. A.9C), or a strike-slip regime but with the magnitudes of the horizontal LCS and vertical ICS similar (*i.e.*, a stress regime that can be consistent with reverse faulting even though ICS is vertical). Stress tensors with LCS about 20° off vertical are the most likely, in which case the magnitude of ICS relative to MCS or LCS is unconstrained (Fig. A.9C). Stress tensors with the magnitudes of ICS and LCS close to equal are also consistent with CSM-JOINT. In these cases, the distinction between Ansdersonian thrust and strike slip starts to break down, and in the extreme that the magnitudes of the two lessor principle stresses are equal, the two stress regimes reduce to the same stress tensor. A roughly thrust stress regime is consistent with the predominance of reverse focal mechanisms in the Eastern US (*e.g.*, Huang *et al.*, 2017), and while we can constrain the lower limit of plausible tectonic stress to about 20–30 MPa, constraining the upper limit would require the consideration of independent stress loads (*e.g.*, Walbert and Hetland, 2022).

2.6 Conclusions

We invert the LOS displacements from two interferograms, an ALOS-2 interferogram from Wicks and Chiu (2022) and a Sentinel-1 interferogram, and differential LiDAR to image the coseismic slip in the 2020, M_w 5.1, Sparta, North Carolina, earthquake. Due to the low SNR of the interferometric and LiDAR data, we use a sparse inversion scheme, GGFL, incorporating a LASSO sparsity constraint and Laplacian smoothing, to improve model estimation. To simultaneously solve for both the fault dip and the distribution of coseismic slip, we vary dip through a Monte Carlo search, inverting for the distribution of slip via GGFL for each dip tested. We find that slip in the Sparta earthquake was shallow and largely oblique, on a fault trending northwest-southeast and dipping 50° to the southwest. Our single-fault coseismic slip model is in contrast to the previous slip model proposed by Wicks and Chiu (2022), which was composed of two fault planes, one slipping aseismically with normal motion and one slipping seismically with reverse motion. We argue that that two-fault plane solution arose due to anomalies in the interferograms resulting from mismatched resolution between the DEM and the InSAR during processing, and the effect of built structures close to the fault trace.

Our preferred coseismic slip model derived from the InSAR data is consistent with the slip that would be expected based on the WSM (Heidbach *et al.*, 2016, 2018). Assuming that MCS is co-linear with Sh_{max} of the WSM and that slip on the fault will be in the direction of maximum fault shear stress on that fault plane, we infer that the Sparta earthquake is consistent with stress tensors that do not depart from Andersonian thrust regime to a large degree. Specifically, we find that if the magnitudes of ICS and LCS are substantially different, the Sparta earthquake is only consistent with stresses with an LCS oriented near vertically. On the other hand, if the magnitudes of ICS and LCS are more similar, the Sparta earthquake is consistent with any orientation of LCS, from horizontal to vertical. Using the calculated stress drop of our preferred coseismic slip model, of about 6 MPa, we additionally constrain the magnitude of the MCS to be over 20–30 MPa.

2.7 Data and Resources

Damage assessment for the Sparta earthquake is from the National Geophysical Data Center / World Data Service (NGDC/WDS): NCEI/WDS Global Significant Earthquake Database. NOAA National Centers for Environmental Information (doi:10.7289/V5TD9V7K; accessed May 2023). The ALOS-2 interferogram is from Wicks and Chiu (2022). The Sentinel-1 data used to produce the S-1 interferogram are publicly available from the European

Space Agency (scihub.copernicus.eu/dhus/#/home; accessed Aug 2020). The Sentinel-1 data were processed using GMTSAR (github.com/gmtsar; Sandwell *et al.*, 2016). The LiDAR data are available at open topography (portal.opentopography.org/datasets; accessed Oct 2021). The focal mechanism of the Sparta Earthquake is from Saint Louis University Earthquake Center (www.eas.slu.edu/eqc;event20200809120737; accessed Mar 2023). Seismicity and Mineral VA earthquake focal mechanism in Fig. 2.1 is from the United States Geological Survey (www.usgs.gov/programs/earthquake-hazards/earthquakes; accessed Jan 2023). The GNSS times series for NCSR is from the Nevada Geodetic Laboratory (geodesy.unr.edu/NGLStationPages/stations/NCSR.sta; Blewitt *et al.* (2018); accessed Feb 2024) All figures were made using the Generic Mapping Tools version 6.2.0 (www.soest.hawaii.edu/gmt; Wessel *et al.*, 2019), with the exception of Figures 2.4B and A.6 which were rendered in Mathematica. The electronic supplement contains additional figures of interferograms, coseismic slip models, and satellite imagery of the Sparta earthquake rupture area. It also includes descriptions of stress drop calculations, a comparison of CSM-DAR to the World Stress Map, and ascii files of the coseismic slip models.

2.8 Acknowledgements

Funding for this research was provided by the the Department of Defense (DoD) through the Department of Defense Science and Engineering Fellowship (NDSEG) awarded to E. Szymanski and NSF grant EAR 1722994 to E. Hetland. We thank Chuck Wicks for kindly sharing the ALOS-2 interferogram, Yihe Haung for discussion regarding computing stress drop, Nathan Niemi for suggesting the inclusion of the LiDAR data, and Fred Pollitz for general discussions about the Sparta earthquake. Finally, we thank one anonymous reviewer, reviewer Chelsea Scott, and associate editor Cezar Trifu, whose comments improved our manuscript, most notably our treatment of the LiDAR data.

CHAPTER 3

Revisiting the 2010 Jiashian and 2016 MeiNong Earthquakes in Taiwan: Geodetic Evidence for Shared Westerly Dipping Thrust Fault

Abstract

Coseismic surface deformation from the 04 Mar 2010 M_w 6.3 Jiashian and 05 Feb 2016, M_w 6.4 MeiNong earthquakes in southern Taiwan was recorded by GNSS for both events and InSAR for the 2016 event. However, coseismic slip did not reach the surface in either case. Their moderate magnitudes, combined with the lack of surface expression, created uncertainty regarding which nodal plane from the seismologically derived focal mechanisms was associated with the responsible faults. While several coseismic slip models for both events have previously been published, the range of fault geometries was rather restricted in both cases. We reassess both earthquakes and create coseismic slip models based on geodetic observations, employing graph-guided fused LASSO within a two-step, integrated estimation approach. We also allow for a wider range of fault geometries, initially starting with non-informative priors on all pertinent fault geometry parameters. Our coseismic model for the 2010 Jiashian event aligns well with the focal mechanisms and earlier reported models. In contrast, for the 2016 MeiNong event, the geodetic data suggests a slip surface that is both more northerly oriented and shallower than what is indicated by the focal mechanisms or previous coseismic slip models. We argue that constraints placed on fault geometry, particularly fault depth, biased the previously modeled coseismic slip. The similarity in fault strikes of our final coseismic models, combined with the proximity of the inferred fault slip regions, indicates that these two earthquakes likely occurred on a single fault structure that dips to the east and becomes steeper at depth.

3.1 Introduction

In 2010 and 2016, a pair of moderate magnitude yet extremely destructive earthquakes struck southern Taiwan: the 04 Mar 2010, M_w 6.3 Jiashian and the 05 Feb 2016, M_w 6.4 MeiNong earthquakes. Coseismic slip in neither earthquake reached the surface (Hsu *et al.* (2011; Jiashian), Huang *et al.* (2016; MeiNong), Qu *et al.* (2017; MeiNong), and Rau *et al.* (2022; MeiNong)), leading to ambiguity as to which nodal planes of the seismologically constrained focal mechanisms corresponded to the slip surfaces. Coseismic surface deformation of both earthquakes was captured by GNSS data (Hsu *et al.* (2011; Jiashian), Huang *et al.* (2016; MeiNong)), and coseismic deformation in the 2016 event was captured by InSAR, allowing for the finite fault to be resolved.

Coseismic slip in the Jiashian earthquake has been imaged on a northwest-southeast striking fault plane, dipping to the northeast (Fig. 3.1; Hsu *et al.*, 2011; Huang *et al.*, 2011; Lee *et al.*, 2013). In contrast, the 2016 earthquake has been imaged to have occurred on a more east-west trending and shallower dipping plane (Fig. 3.1; Qu *et al.*, 2017; Rau *et al.*, 2022). The strikes of these inferred planes are quite different from the strike of the fault that slipped in the 1999, M_w 7.6 ChiChi earthquake (e.g., Yoshioka *et al.*, 2001), as well as the inferred slip planes of the 2013, M_w 6.2 and M_w 6.5 Nantou earthquake pair, which occurred downdip of the ChiChi earthquake (e.g., Lee *et al.*, 2015). The strikes of the Jiashian coseismic models, as well as the inferred slip plane of the 2012, M_w 5.9 Wutai earthquake (Chiang *et al.*, 2016), are all rotated relative to the ChiChi earthquake, although not to the degree that the published MeiNong coseismic models are (Fig. 3.1).

We re-examine the 2010 Jiashian and 2016 MeiNong earthquakes, developing new coseismic source models from geodetic data. Our new models suggest that the earthquakes occurred on a single thrust fault with dip steepening at depth. We use GNSS data to constrain both the 2010 Jiashian (coseismic offsets from Hsu *et al.*, 2011) and the 2016 MeiNong (offsets from Huang *et al.*, 2016) earthquakes, in addition to InSAR data for the 2016 MeiNong event (data described below). We use the GGFL (graph-guided, fused LASSO) inversion method described in Szymanski *et al.* (2024), a compressed sensing-based inversion whose objective function includes both Laplacian smoothing and sparsity constraints. We follow a two step inversion process, initially performing a Monte Carlo search over fault strike, dip, location, depth, length, and width assuming uniform fault slip. We then invert for distributed slip on the best 10,000 models found in the initial search, integrating the ranking of both fault geometry and slip distribution. This two-step process is a departure from our earlier work on the 2020, M_w5.1 Sparta, NC earthquake, where we fully integrated the inference of the fault dip and distributed slip in a single step (the Sparta earthquake was surface breaking,

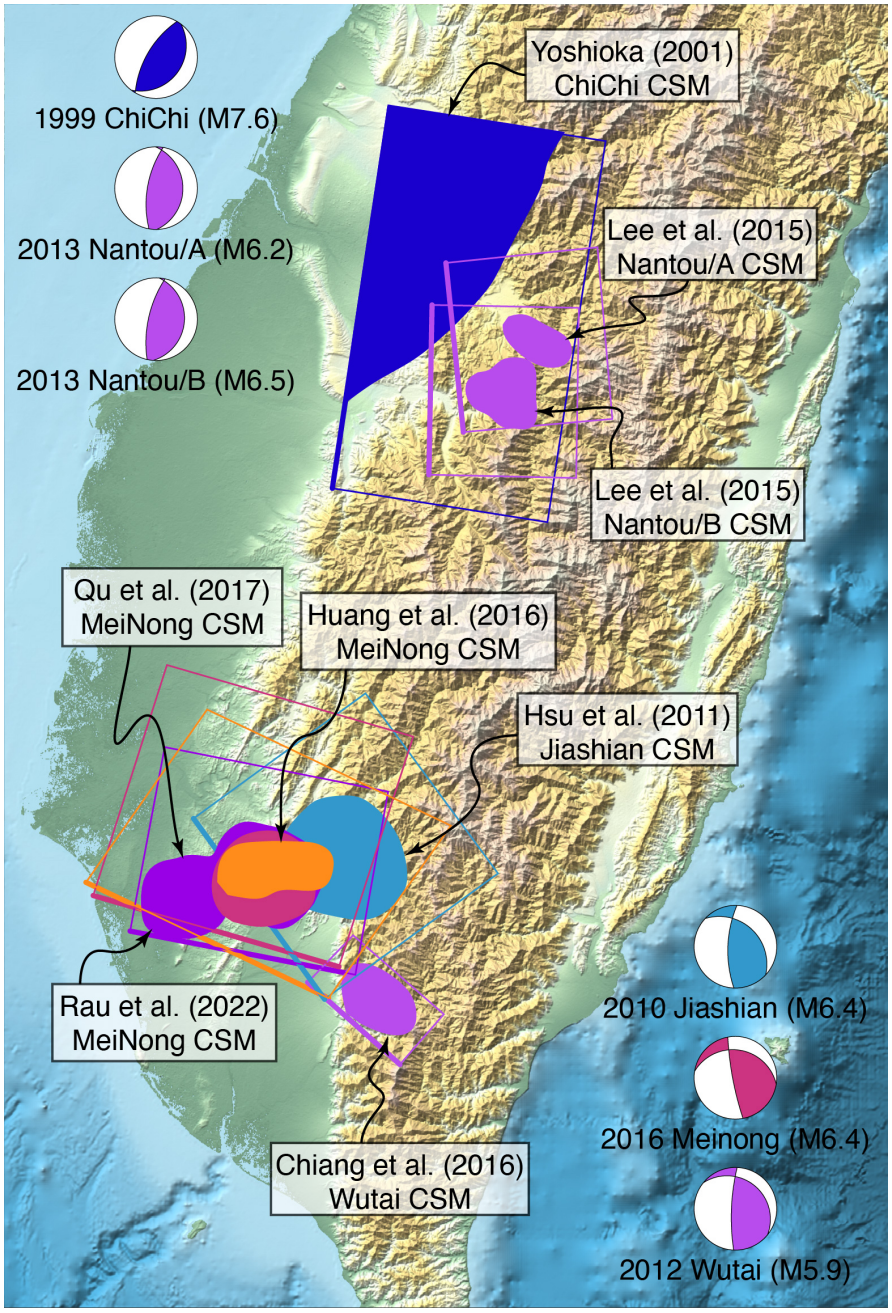


Figure 3.1: Focal mechanisms of several notable earthquakes in western Taiwan (double couple solutions from the Global Centroid Moment Tensor Catalog, GCMT), along with coseismic slip models (CSMs) of those earthquakes; thick lines indicate the top edge of the fault in the CSMs, and filled areas are the approximate regions of sizable fault slip in those CSMs (regions are approximated from figures in the associated publications, with filled polygons roughly correspond to the regions where slip was larger than about 20% of the maximum slip and are just for illustration purposes, readers should see references for details of their CSMS; Yoshioka (2001; ChiChi), Hsu *et al.* (2011; Jiashian), Lee *et al.* (2015; Nantou events), Chiang *et al.* (2016; Wutai), Huang *et al.* (2016; MeiNong), Qu *et al.* (2017; MeiNong), and Rau *et al.* (2022; MeiNong).

allowing other fault geometry parameters to be estimated from the earthquake trace).We do not impose any constraints on the slip rake.

The surface deformation due to the 2010 Jiashian earthquake was captured by GNSS observations, which Hsu *et al.* (2011) used to develop a coseismic slip model of the 2010 Jiashian earthquake. They inverted for distributed slip using Laplacian smoothing and rake constraints, varying the slip plane strike from 290° to 330° and dip from 30° to 90°. The optimal fault strike and dip was found to be 324° and 40°, respectively, which is broadly consistent with aftershocks (Huang *et al.*, 2011) and the focal mechanisms (within 10° of one of the nodal planes of the Jiashian earthquake; 3.1). The oblique thrust slip was also quite consistent with $S_{H_{\max}}$ values (the azimuth of inferred slip rake in their model was in the range 245°–270°). Assuming the same optimal planar slip surface determined by Hsu *et al.* (2011), Lee *et al.* (2013), subsequently determined a coseismic slip model from the same GNSS data, but adding in constraints from local seismic data. Their refined coseismic slip model had a slightly larger main slip patch, with some slip near the tip of the buried fault. In developing our coseismic slip model of the Jiashian earthquake, we only consider GNSS data and integrate the inference of the fault plane geometry and distributed slip. As shown below, our coseismic slip model is consistent with these two previously determined models. Our motivation for re-considering the 2010 earthquake was partly as we wanted to consider a wider range of potential fault geometries, including geometries corresponding to the second nodal plane of the focal mechanism solutions. A large motivation to reconsider this earthquake was merely as because the coseismic slip models of Hsu *et al.* (2011) or Lee *et al.* (2013) are not openly disseminated beyond the figures in their publications, accompanied by limited quantitative information, limiting our ability to use the coseismic model for future investigations.

The surface deformation due to the 2016 MeiNong earthquake was captured by GNSS and InSAR data (e.g., Huang *et al.*, 2016). The coseismic deformation was also captured by leveling data (Rau *et al.*, 2022), although the data does not appear to be openly available. The study of Huang *et al.* (2016) used GNSS data and four InSAR interferograms, along with near source seismic data, to develop a coseismic slip model of the 2016 MeiNong earthquake. They searched planar fault geometries with strikes ranging from 280° to 320° and dips ranging from 0° to 40°, but at a fixed depth and location and with a uniform rake across the fault plane, ranging from 30° to 70°. They found that coseismic slip on a single planar fault (strike, dip, and rake, 299°, 15°, and 45° respectively) was unable to explain all of the surface uplift, and proposed that the coseismic slip triggered aseismic slip on a smaller fault in the hanging wall. Qu *et al.* (2017) re-examined the MeiNong earthquake, developing a coseismic slip model composed of a curved fault, with initial dip of 30° at an assumed depth

and then flattening to 10° dip at depth. Qu *et al.* (2017) assumed a fixed location of the fault, a strike of 288° (they state that the fault parameters were settled on through trial-and-error, although do not give details on the strategy for that optimization), and a constant *a priori* unknown slip rake. They developed a coseismic slip model using two Sentinel-1A interferograms and the GNSS data, inferring coseismic slip with a rake of 24°. Similar as to Huang *et al.* (2016), Qu *et al.* (2017) favored that there was induced aseismic slip on a shallow, north-south striking fault in the hanging wall, based on residual uplift unexplained by the coseismic slip model and a pattern of aftershocks in the hanging wall, aftershocks that were delayed by 14 minutes. More recently, Rau *et al.* (2022) developed a finite fault model constrained only by local seismic data. They assumed a planar fault striking 288° and dipping 25°, with fixed location and at a depth of just over 10 km, inferring oblique thrust slip, with patches of substantial left-lateral slip (see Fig. 3.4a of Rau *et al.*, 2022). Using that finite fault model, Rau *et al.* (2022) forward modeled the observed geodetic offsets, finding that the finite fault model underpredicted the large vertical offsets in the GNSS data. The lack of ability to capture the vertical offsets is a similar finding as that of Huang *et al.* (2016) and Qu *et al.* (2017), although Rau *et al.* (2022) argued for inelastic deformation associated with mud diapirism rather than aseismic slip on a shallow fault.

All three of the MeiNong coseismic slip models described above are largely consistent in their salient features, including the more east-west strike of the fault compared to the adjacent Jiashian fault plane (Fig. 3.1), the shallow dip of the fault, the large degree of left-lateral strike-slip, and the inability to capture the observed vertical surface offsets by the seismic slip alone. Additionally, all of these models share that they assumed some aspect of the geometry of the source fault, either *a priori* or through a potentially limited, and in some cases undocumented, preliminary search. Motivated by curiosity about the degree to which particular choices of model geometry parameters affects the coseismic slip model, we develop a coseismic slip model of the 2016 MeiNong earthquake, integrating determination of all fault plane geometry parameters with determination of the coseismic slip using a compressed sensing inversion method. Faults nearer to the surface or with slip rake closer to pure thrust result in larger amplitude vertical deformation, and thus choosing to only consider deep fault planes may exacerbate the need to appeal to non-seismic components. There is also a strong trade-off between fault plane strike and slip rake in coseismic slip models in coseismic slip models, with stronger thrust slip components resulting in more coseismic surface uplift. Finally, as in the Jiashian earthquake, part of our motivation was that the lack of open dissemination of the previously published coseismic slip models, beyond the figures in the aforementioned papers. We use GNSS data and two interferograms, as described below, to develop the MeiNong coseismic slip model, reserving another two, fully independent,

interferograms to test the resulting slip models. In contrast to the consistency between our new Jiashian coseismic slip model and previous models, we find that the geodetic data favors a MeiNong coseismic model with a shallower, more northwest-southeast striking, and larger thrust component than previously published coseismic slip models.

In the following sections, we first describe our estimation strategy. Secondly, we present the result of our estimation of the Jiashian and MeiNong earthquakes, including describing the results of the initial uniform search, the integrated search, and present the best fit models. Third, we discuss the geodetic evidence for our new MeiNong coseismic model, contrasting that model to one that is more similar to previously published models. Fourth, we discuss the relationship between the inferred slip patches in our Jiashian and MeiNong earthquakes, suggesting that both occurred on the same fault structure.

3.2 Integrated estimation of coseismic slip models

To constrain the Jiashian and MeiNong coseismic slip models, we invert the GNSS data from Hsu *et al.* (2011) and Huang *et al.* (2016), respectively (Fig. 3.2). Despite the similarity of the magnitudes of the two earthquakes, the coseismic surface offsets differ markedly. The maximum magnitude of the horizontal deformation in the Jiashian and MeiNong earthquakes is 27.3 and 39.4 mm, respectively, with only 8 stations in the Jiashian coseismic data having offsets larger than 10 mm compared to 29 in the MeiNong coseismic data (Fig. B.1). The coseismic vertical offsets are even more contrasting, with a maximum uplift of 25.1 mm in the Jiashian earthquake, compared to 104.7 mm in the MeiNong earthquake. Two GNSS stations recorded uplifts of over 70 mm in the MeiNong earthquake, with 41 stations registering vertical deformation over 10 mm. In contrast, there are only 10 stations whose GNSS derived offsets during the Jiashian earthquake was over 10 mm. The large vertical offsets in the MeiNong were noted previously (*e.g.*, Haung *et al.*, 2016, Qu *et al.*, 2017 Rau *et al.*, 2022), with the Rau *et al.* (2022) describing the vertical offsets as "unexpectedly large." However, it is worth noting that the ratio of the vertical offsets to the magnitudes of the horizontal offsets is not drastically different for these two earthquakes (Fig. B.1), suggesting that it is not that the MeiNong produced unusually large uplift, but that it produced much larger total deformation.

For the MeiNong earthquake, we additionally invert line-of-sight (LOS) offsets from two interferograms, derived from ascending or descending orbits of the European Space Agency's Sentinel-1A/B satellite. The ascending interferogram is derived from radar scenes acquired 02 Feb 2016 and 14 Feb 2016, for a time span of 12 days, encompassing 3 days before the MeiNong earthquake and 9 days of the postseismic period (Table 3.1). The descending

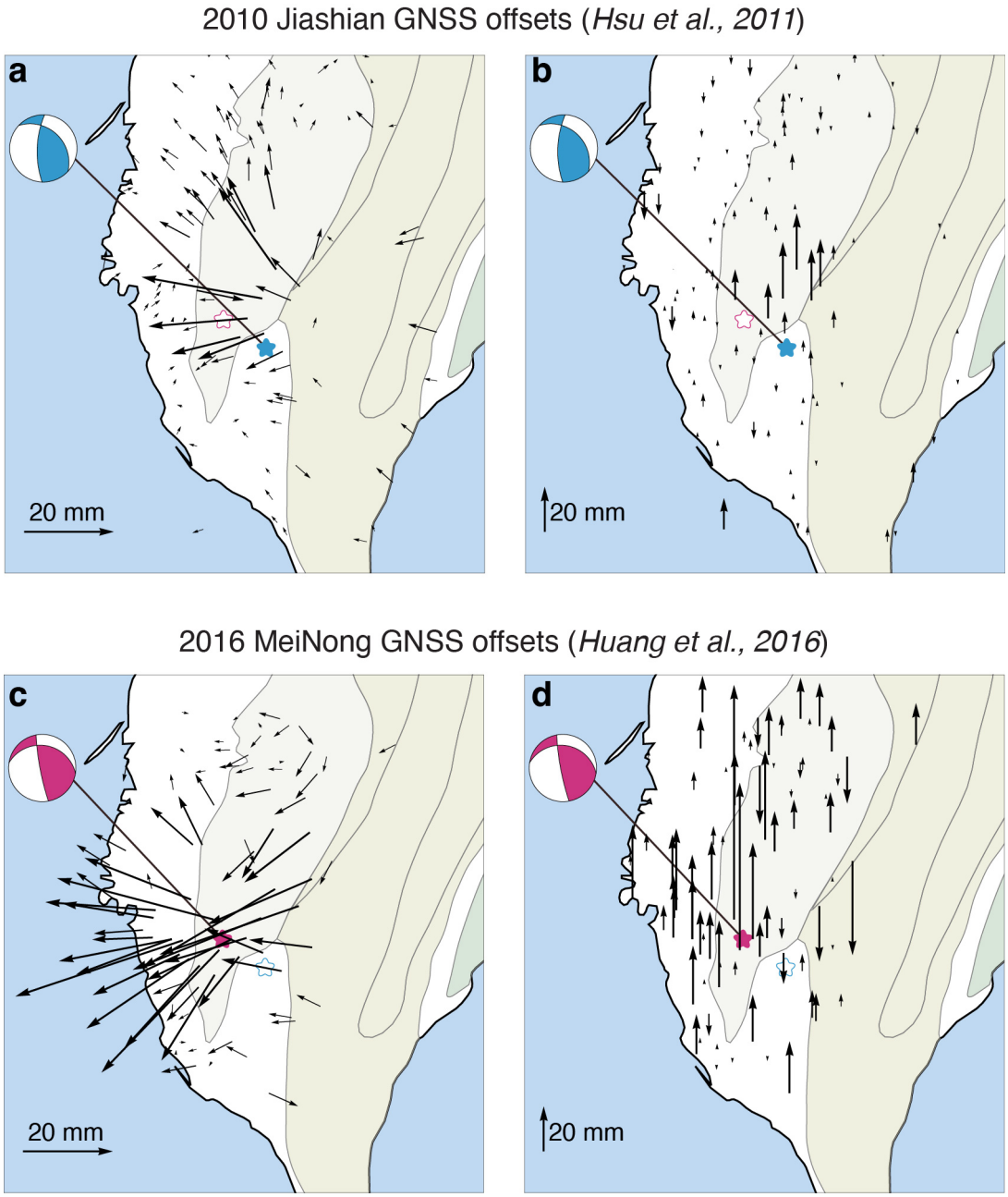


Figure 3.2: GNSS coseismic offsets for the Jiashian (**a** and **b**; Hsu *et al.*, 2011) and MeiNong (**c** and **d**; Huang *et al.*, 2016) earthquakes. Panels (**a**) and (**c**) are the horizontal deformation, while (**b**) and (**d**) are vertical deformation. Purple and red stars indicate the GCMT centroid locations for the Jiashian and MeiNong earthquakes, respectively. Shaded regions are generalized geological regions of Taiwan: Western Foothills (tan); Hsueshan Range, Backbone Range, and Eastern Central Valley Range (yellow); and Coastal Range (green)

orbit	date 1	date 2	span	# pre-eq days	# post-eq days	role
ascending	2016-02-02	2016-02-14	12 days	3 days	9 days	training
ascending	2016-01-09	2016-03-09	60 days	27days	3 days	testing
descending	2016-02-04	2016-02-28	24 days	1days	23 days	training
descending	2016-01-11	2016-03-23	72 days	25 days	47 days	testing

Table 3.1: Orbits and dates of SAR acquisitions (year-month-day) used to produce interferograms of the MeiNong coseismic deformation. The time span of each interferogram is indicated, along with number of days prior to ("pre-eq") and following ("post-eq") the earthquakes. The role of the interferograms in the inversion process, either being inverted to determine the coseismic slip model ("training") or unseen data used to test the resulting cosiemsic slip model ("testing"), is indicated.

interferogram is derived from scenes acquired 04 Feb 2016 and 28 Feb 2016, with a 24 day time span. We use LOS measurements from two independent interferograms to calculate the chi-square of the resulting slip model. These latter testing interferograms, unseen by the inversion, are derived from Sentinel-1A/B radar scenes acquired on 09 Jan and 09 Mar 2016 in ascending orbit and 11 Jan and 23 Mar 2016 in descending orbit (3.1). We choose to use the two interferograms whose time span closest brackets the MeiNong earthquake for training, while using two fully independent interferograms with a longer temporal baseline for testing, as in general cleaner data should be used for model training to build a more precise understanding of the underlying signal, whereas use of noisier data for testing aids in selecting a robust model with more predictive power (Murphy, 2012). For both earthquakes, we use the GNSS data both in the inversion and to rank the resulting model via chi-squared.

To generate the interferograms we use the open-source SAR processing software GMTSAR (Sandwell *et al.*, 2011). The wrapped scenes are first low-pass filtered with a 160 meter wavelength Gaussian filter and then filtered a second time using a Goldstein adaptive filter (Goldstein and Werner, 1998) with an exponent of 0.6 and patch size of 32 by 32 pixels. Once filtered, we unwrap phase using SNAPHU (Chen and Zebker, 2002) for all resolution cells exceeding a coherence threshold of 0.1. We then estimate and remove residual orbital, topographic, and tropostatic phase contributions via a bicubic ramp containing an elevation term, fit to the interferograms using a robust least-squares algorithm (Xu *et al.*, 2014). The unwrapped, detrended scenes are then cropped to the box 120.0°–121.1°E longitude and 22.45°–23.53°N latitude, and then down sampled using a saliency-based quad-tree sampling algorithm (Gao *et al.*, 2021). The mean LOS range change for each quad-tree node is retained as a sample, either inverted for slip (if from a training interferogram) or used to rank the resulting coseismic slip model (if from a testing interferogram). Sample sizes for

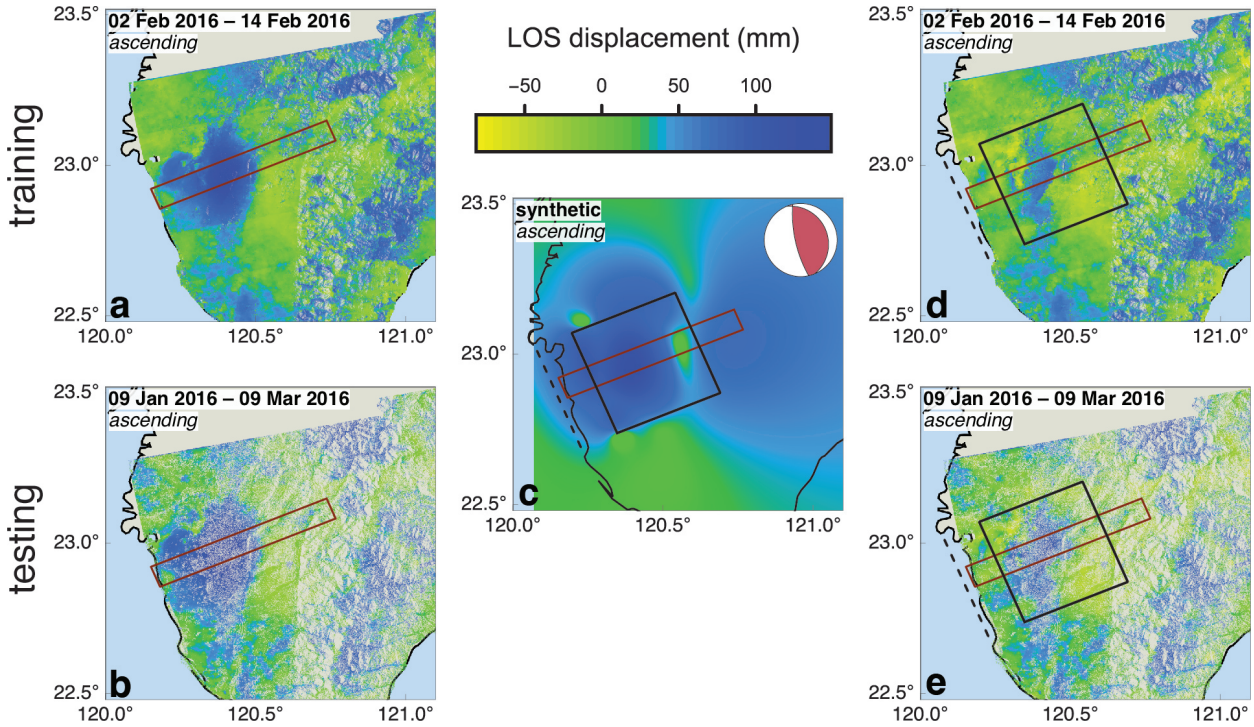


Figure 3.3: Ascending interferograms capturing the coseismic displacements of the MeiNong earthquake (**a** and **b**), that are either inverted (training; **a**) or used to calculate the χ^2 of the resulting model (testing; **b**). Burgundy line indicates swath of LOS offsets in Fig. 3.11. Synthetic LOS offsets resulting from slip in the best fit MeiNong coseismic model (**c**; with best-fit double-couple of the model shown), and residual interferograms (**d** and **e**).

the ascending and descending interferograms used for training are 210 and 196, respectively, and 387 and 229 for the testing ascending and descending interferograms respectively. For the estimation of the InSAR noise covariance matrix, $\mathbf{C}_n$, we follow Lohman and Simons (2005) and use the structure function

$$S(r) = E\left[(f(\mathbf{x}) - f(\mathbf{x}+\mathbf{r}))^2\right] \tag{3.1}$$

to calculate $\mathbf{C}_n$, as

$$C_n(r) = \sigma^2 - S(r)/2, \tag{3.2}$$

where σ^2 is the noise variance for a given scene and r is the distance between two points. To estimate $S(r)$ and σ^2 we use variography. Following Lohman and Simons (2005) we use a large, uniform sampling from the interferograms, masking out the regions of the interferograms that are most expected to have coseismic deformation signal, to determine $S(r)$, taking the variogram sill value to be σ^2.

We follow a two-step process for developing the coseismic slip models, incorporating an

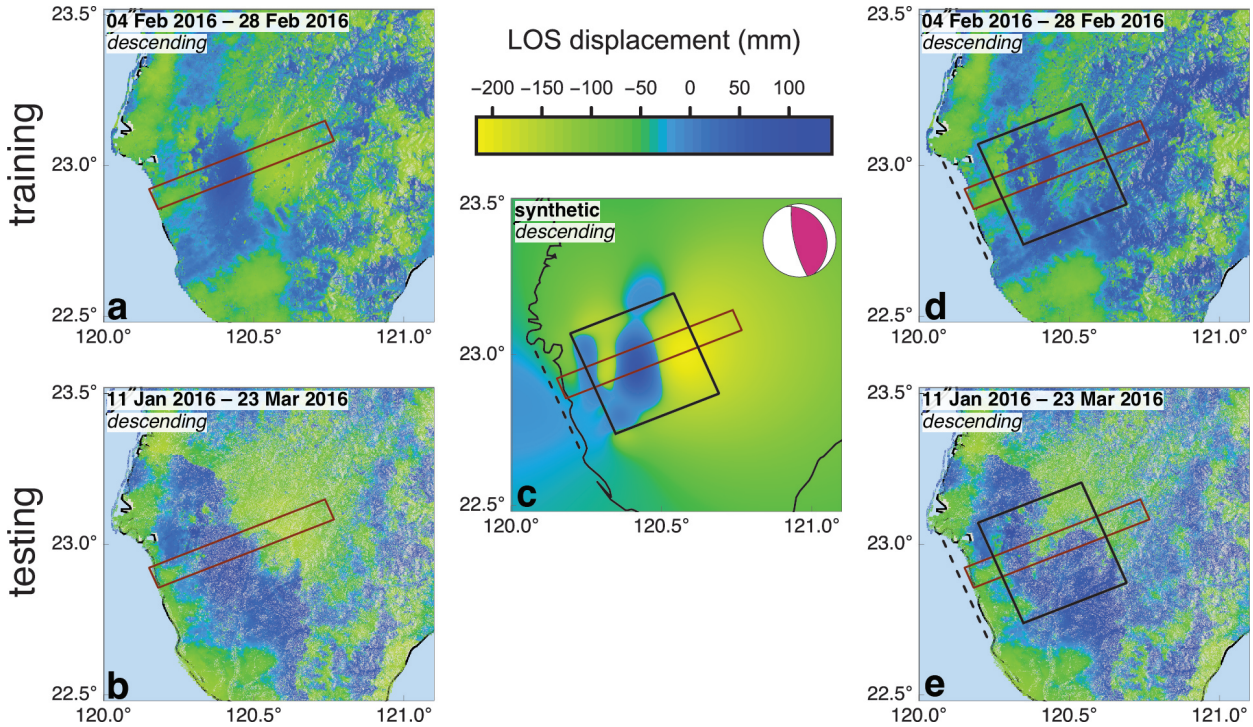


Figure 3.4: Descending interferograms capturing the coseismic displacements of the MeiNong earthquake (**a** and **b**), that are either inverted (training; **a**) or used to calculate the χ^2 of the resulting model (testing; **b**). Burgundy line indicates swath of LOS offsets in Fig. 3.11. Synthetic LOS offsets resulting from slip in the best fit MeiNong coseismic model (**c**; with best-fit double-couple of the model shown), and residual interferograms (**d** and **e**).

initial step composed of a Monte Carlo search over all parameters describing the geometry of a plan with uniform slip, and a secondary step integrating a search over fault geometry parameters with the inversion of distributed slip. Such a two-step search process, is often used to determine coseismic slip models, allowing one to separate the estimation of the non-linear parameters controlling the fault plane geometry with the linear inversion of distributed slip (*e.g.*, Clark *et al.*, 1997, Jonsson *et al.*, 2002). However, the most optimal geometry determined assuming uniform slip is not necessarily most optimal geometry for a model in which coseismic slip is non-uniform (*e.g.*, He *et al.*, 2017; Wicks and Chiu 2022; Szymanski *et al.*, 2024). Combining the estimation of the geometry parameters with slip distribution can range from a full-blown estimation of all parameters simultaneously (e.g., Minson *et al.*, 2013) to using a parametric description of slip distribution (e.g., Wick and Chiu 2022). For our work in the Sparta earthquake, we integrated a Monte Carlo search of the fault dip with the inversion for distributed slip into a single one-step process (Szymanksi *et al.*, 2024), which included determination of the inversion penalty parameters for each candidate slip surface (a full description of the penalty parameters is below). This full integration was

computationally tractable for the surface breaking Sparta earthquake, as the only non-linear geometry parameter to be estimated was the fault dip. For the two blind thrust earthquakes we consider here, we start from an assumption that none of the fault geometry parameters are *a priori* known, and thus fully integrating their estimation along with distributed slip is computationally burdensome. We, therefore, use a two-step estimation, taking the 10,000 best planar geometries, out of more than four million trial models, in the initial uniform search as candidate geometries for which we determine distributed slip on. As we assume non-informative priors in our initial search, one may view our initial search as narrowing the priors on the fault geometry parameters, that are then used in a subsequent integrated estimation. To further reduce computational demands, we opt to use fixed penalty parameters, as discussed below. The entire estimation process for a single coseismic slip model takes about 12 hours on a circa 2001 Intel Core i9 (3.7GHz and 64GB memory).

The initial search assumes uniform slip on a planar fault, parameterized by the location of the center of the top of the fault (c_x, c_y), the depth of the top of the fault (*i.e.*, burial depth; d), the length and dip of the fault (L and W, respectively), and the strike and dip (ϕ and θ, respectively). We generate trial fault planes, assuming all parameters are equally likely, generating trial samples uniformly within the bounds of 5 km$\leq L, W \leq$12 km, c_x between 25 km west and 5 km east of the USGS epicenter, and c_y between 10 km south and 20 km north of the USGS epicenter. The range of c_x and c_y was chosen through iteration, so that the range fully encompassed the top 20,000 models. We assume any ϕ and θ are equally likely (*i.e.*, $-\pi < \phi \leq \pi$ and $-\pi/2 \leq \theta \leq 0$) and generate near evenly spaced samples on a sphere defined by ϕ and θ, which ensures that we do not over sample near horizontal faults relative to vertical faults. In total, we general 4,050,080 and 4,051,420 trial fault planes for the Jiashian and MeiNong coseismic slip models, respectively (note that the algorithm to sample the sphere is randomly seeded, and thus only a target number of samples can be specified, not the exact number). For each of the trial fault planes, we then invert for the strike- and dip-slip components of slip (U_s and U_d, respectively) via linear least squares, with no constraint on either the sign of slip or the slip rake.

We then take the fault geometries from the best 10,000 coseismic models found in the initial search for each earthquake, based on χ^2 fit. For both earthquakes, χ^2 includes the GNSS model residuals and the published data uncertainties. For the MeiNong earthquake, χ^2 additionally includes the LOS model residuals and the uncertainties, as described above, for the testing data. From these coseismic models we use c_x, c_y, ϕ, θ, and d to generate fault planes on which we solve for the distributed slip. We set each of the fault planes to 40 km by 40 km, and discretized into 200 2×2 km^2 subfaults. We solve for the optimal distribution of slip on each trial fault plane using the GGFL inversion scheme we developed in Szymansk *et*

al. (2024), which includes both sparsity and smoothness regularization terms. The sparsity constraint is imposed on the model vector in an L1-norm, and the constraint tends to decrease the number of subfaults with nonzero slip. The smoothness constraint is imposed via the L2-norm of the Laplacian on the slip across the fault surface, increasing the smoothness of the inferred slip (each component of slip, dip- or strike-slip is smoothed independently). As the sparsity constraint is in terms of the L1-norm, we cast the estimation as a second-order cone program (SOCP; Boyd and Vandenberghe, 2004). Framing the optimization as a SOCP allows us to avoid approximating the absolute value contained in the L1-norm, as we did in our previous implementation (Szymanski *et al.*, 2024). To solve for the strike- and dip-slip offsets, we use a splitting-conic solver, which employs the alternating direction method of multipliers, and is a more efficient method than using other solvers which typically employ less flexible interior point methods (O'Donoghue, 2016). We do not add any constraint on allowable rake or sign of the strike- or dip-slip offsets.

In the GGFL estimation, there are two penalty parameters, λ_1 on the sparsity constraint and λ_2 on the Laplacian constraint, imposing smoothness. Following Szymanski *et al.* (2024), λ_1 can be related to a bound on the moment of the resulting coseismic slip model, and we use the seismic moment along with the data errors to calculate it *a priori*. Using this approach allows us to both reduce computational burden and tie λ_1's value directly independently observed physical attributes of the earthquake. λ_2 can be solved for using the L-curve criterion, an analytical method for determining the optimal trade-off point of a standard L-curve used to determine penalty parameters in least squares problems (Hanssen, 1999). For both earthquakes, we initially explored searches where the optimum λ_2 was solved for in each of the 10,000 sample fault geometries, finding two distinct populations associated with each nodal plane. The distributions of λ_2 for both earthquakes shared similar characteristics with heavy right-skew distributions for values associated with the north dipping nodal planes and approximately symmetric distributions for values associated with the west dipping nodal planes. The median values for the north dipping distributions were approximately 0.12 and 0.1 for MeiNong and Jiashian respectively, with median values for the west dipping distributions being approximately 0.23 and 0.13 for each of the earthquakes. For simplicity, we opted to set $\lambda_2 = 0.2$ and 0.1 for the Jiashian and MeiNong coseismic models, respectively, which fell within the central regions of each of the distributions of λ_2. The higher λ_2 in the Jiashian coseismic model likely reflects the use of the much smaller data set compared to that for the MeiNong earthquake. Inversion runs with different λ_2 values either resulted in noisy models (*i.e.*, models with oscillations of normal and reverse dip-slip or left- and right-lateral strike-slip) or overly smoothed models and associated degraded χ^2.

3.3 Results

3.3.1 Initial uniform slip search

As described in the previous section, we initially invert for U_s and U_d on over four million trial fault plane geometries for each of the earthquakes. Each of the trial fault planes is then ranked according to how well the associated coseismic slip model fits the GNSS data, along with the the unseen InSAR data in the MeiNong models. The location, ϕ, and θ of the the 20,000 best fitting models are shown in Fig. 3.5. As our goal with this initial search is to determine trial fault plane geometries that are then used to determine distributed slip, we do not discuss the variations of L, W, U_s, and U_d here (the distribution of these parameters is discussed in the Supplemental Material, and are are presented in Fig. B.1), and save discussion of the fault slip for our discussion of the integrated search results below. Likewise, we only discuss b in context of the integrated search. From the initial search we find that the fault location for steeply dipping planes is more tightly constrained than for shallow dipping planes, with the locations of the latter varying by 20–25 km (Figs. 3.5a and b).

The inferred dip of the fault planes in the initial search of both earthquakes is bimodal (Figs. 3.5c and d). The steeper dipping planes are associated with north-south striking faults, while the shallower planes are associated with northeast-southwest strikes (Figs. 3.5e and f). For very shallow dipping planes, large variations in strike will result in minimal variation in the actual fault plane for these relatively compact planes (the dimension of the uniform slip patches in these top 20,000 models are roughly 6–10 km; Fig. B.2), which leads to a less well constrained strike. Each of the constellations of ϕ and θ correspond to one of the two nodal planes in the seismic moment tensors (Fig. 3.5e and f), although for these blind earthquakes the geodetic data is fit better by the shallower dipping planes (Fig. 3.5e and d). Generally, the best fitting coseismic models for the MeiNong earthquake have strikes closer to north-south trending than the associated nodal plane in the seismic moment tensor, an issue we discuss further below. Finally, the most successful MeiNong coseismic models have faults with shallower dips compared to the Jiashian models (Fig. 3.5).

3.3.2 Integrated search: fault geometries

We then invert for distributed slip on the fault geometries, including only location, ϕ, θ, and d, of the 10,000 best fitting models found in the initial search. As before, the resulting coseismic slip models are ranked by the χ^2 fit to the GNSS data for each of the earthquakes, and the unseen InSAR data of the MeiNong earthquake. We first discuss ϕ and θ in context

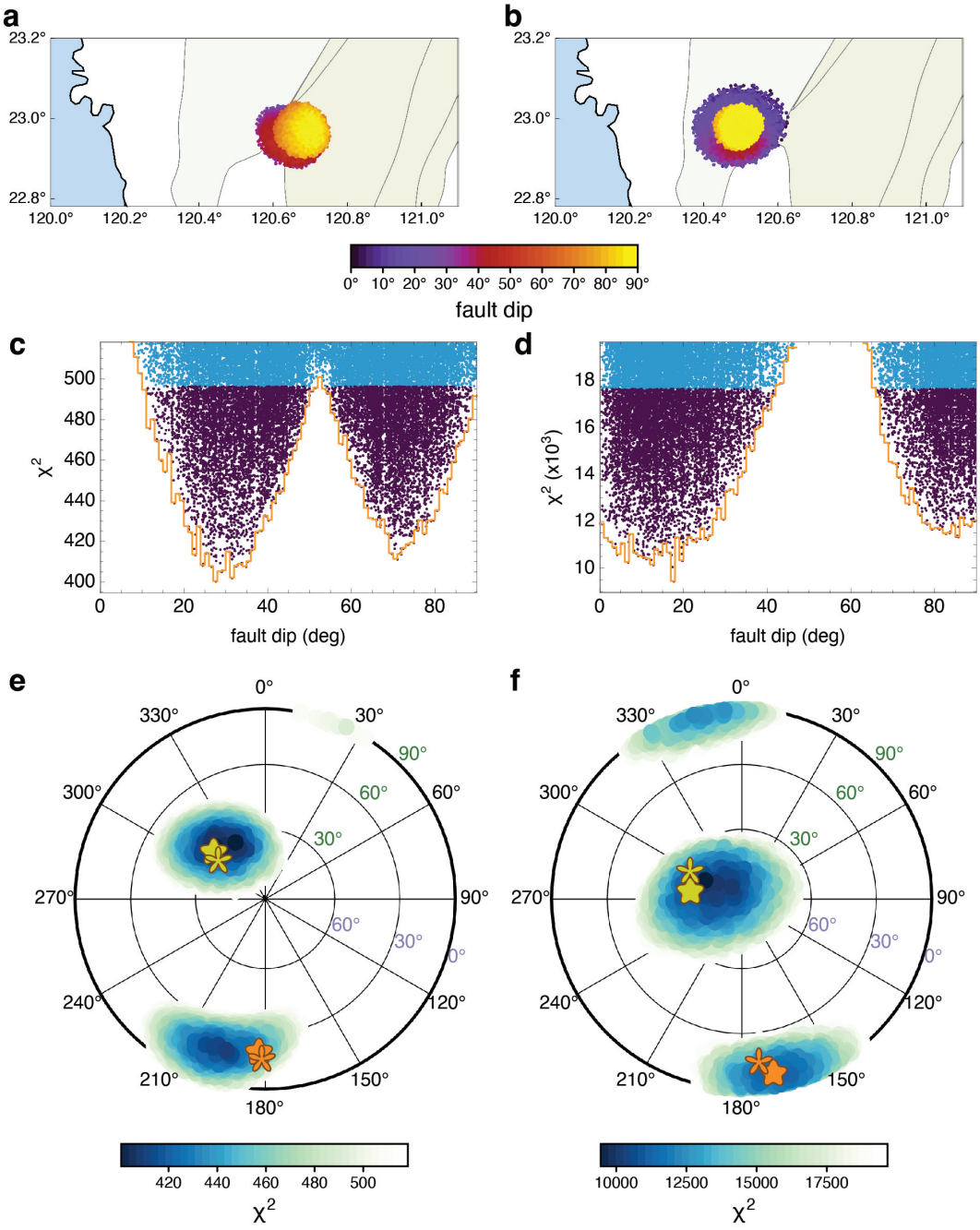


Figure 3.5: Location of the faults in the 20,000 best fitting coseismic slip models found in the initial search for the Jiashian (**a**) or MeiNong (**b**) earthquakes. Plotted point is the location of the center of the top of the fault plane, colored by the dip of the fault. Model fit *vs.* fault dip in the top 20,000 initial Jiashian (**c**) or MeiNong (**d**) coseismic slip models. Purple points depict the top 10,000 best fitting models and blue are the next 10,000; orange lines are the lowest χ^2 in 1° bins. Strike and dip of the fault planes in these 20,000 models for the Jiashian (**e**) or MeiNong (**f**) earthquakes, shown in a Lambert projection and colored according to the fit of the coseismic slip model. Values along the outer circumference indicate the strike of the fault plane, and numbers in the interior circles indicate either dip (green text) or codip (blue text); stars and asterisks depict the two nodal planes in the GCMT or USGS focal mechanisms, respectively.

		fault plane				centroid		
event		depth (km)	strike	dip	λ	lat	lon	depth (km)
Jiashian	GCMT	N/A	-47°	30°	45°	22.86°	120.56°	29.1
	USGS	N/A	-50°	26°	42°	22.92°[1]	120.80°[1]	35.0
	uniform	14.3	-28°	27.5°	46°	22.90°	120.50°	18.8
	best int.	3.1	-35°	29°	44°	22.99°	120.62°	13.5
	ensemble	1.3	8°	6°	10°	0.01	0.01	1.2
MeiNong	GCMT	N/A	-81°	22°	21°	22.94°	120.43°	17.3
	USGS	N/A	-61°	25°	38°	22.94°[1]	120.60°[1]	25.5
	uniform	10.9	-63°	18°	40°	22.90°	120.50°	16.0
	best int.	4.1	-23	17°	80°	22.99°	120.44°	10.1
	ensemble	1.4	15°	4°	14°	0.01	0.01	0.5

Table 3.2: Nodal plane orientations of the GCMT and USGS focal mechanisms most closely associated with the slip surfaces resolved here, along with location and depth of the centroid (1: USGS location is the epicenter); parameters of the fault plane and centroid location for the model with lowest χ^2 in the initial search with uniform fault slip, and the best model from the integrated search. Also given are the standard deviation of the parameters from an ensemble of all models within 10% of the best-fit χ^2, for each earthquake (38 and 107 models for Jiashian and MeiNong coseismic models, respectively). Depth is to the top of the fault plane; λ is either slip rake or the average slip rake in the subfaults, weighted by the slip magnitude in that subfault, for the uniform or the integrated best/ensemble, respectively. For the uniform model, centroid depth is the depth of the center of the fault plane.

of the integrated search. We then discuss location and d of the fault planes for the two earthquakes, and finally we discuss the inferred slip distributions.

In the secondary integrated search, the data fit increases over the fits in the initial search as more data features can be described by non-uniform distributions of slip. The trial values of ϕ and θ do not change from what was presented above, although the associated fit of these values does change, and hence the two constellations of ϕ and θ similar to each of the focal mechanism nodal plane persist; however, for both earthquakes fault geometries similar to the shallower of the nodal planes are even more favored by the data compared to in the uniform search (Fig. 3.6). Likewise, that the geodetic data of the MeiNong earthquake are best fit by northwest-southeast striking faults is more prominent in the integrated search (*cf.* Figs. 3.5f and 6d), an issue we discuss in the Discussion section.

The dips of the faults in the best fitting Jiashian coseismic slip models are generally steeper than the dips in the best fitting MeiNong models (20°–40° in the Jiashian models, compared to less than about 20° in the MeiNong models; Fig. 3.6). In contrast, the strikes of the faults in best fitting Jiashian and MeiNong coseismic models are quite similar, with the centroid of slip in the MeiNong models is almost directly west of the centroid of slip in the Jiashian models (Fig. 3.7a). The burial depths of the faults in the best fitting Jiashian or MeiNong earthquakes are similar (*cf.*, Figs. 3.7b and c), although that does not indicate that the inferred slip in each earthquake is at the same depth, as the dips of the fault planes are not the same for the two earthquakes. Rather, the shallower dip of the MeiNong fault models results in shallower centroids (3.2; Fig. B.3). Note that the GGFL-based inversion of slip can indeed put the centroid of slip deep, corresponding to the lower part of the 20 km wide fault plane, and indeed of these 10,000 MeiNong models many have inferred centroids that are up to 20 km deep (Fig. B.3); however, overall most of the inferred centroids of the Jiashian earthquake are deeper than for the Meinong earthquake. Moreover, the models that best fit the geodetic data all have centroids closer to the surface than in the Jiashian models (Fig. B.3). Taken together, the shallower slip in the MeiNong earthquake directly to the west of the inferred Jiashian earthquake slip, on a more gently dipping fault plane with similar strike, suggests that the slip in these two earthquakes occurred on a single fault dipping to the east and steepening with depth. Before exploring this interpretation further, we present the inferred slip distributions for these two earthquakes.

3.3.3 Integrated search: best fit models

The inferred slip in each of the best fitting coseismic slip models of the two earthquakes is relatively compact (Fig. 3.8). The average slip rake, weighted by the magnitude of slip in each

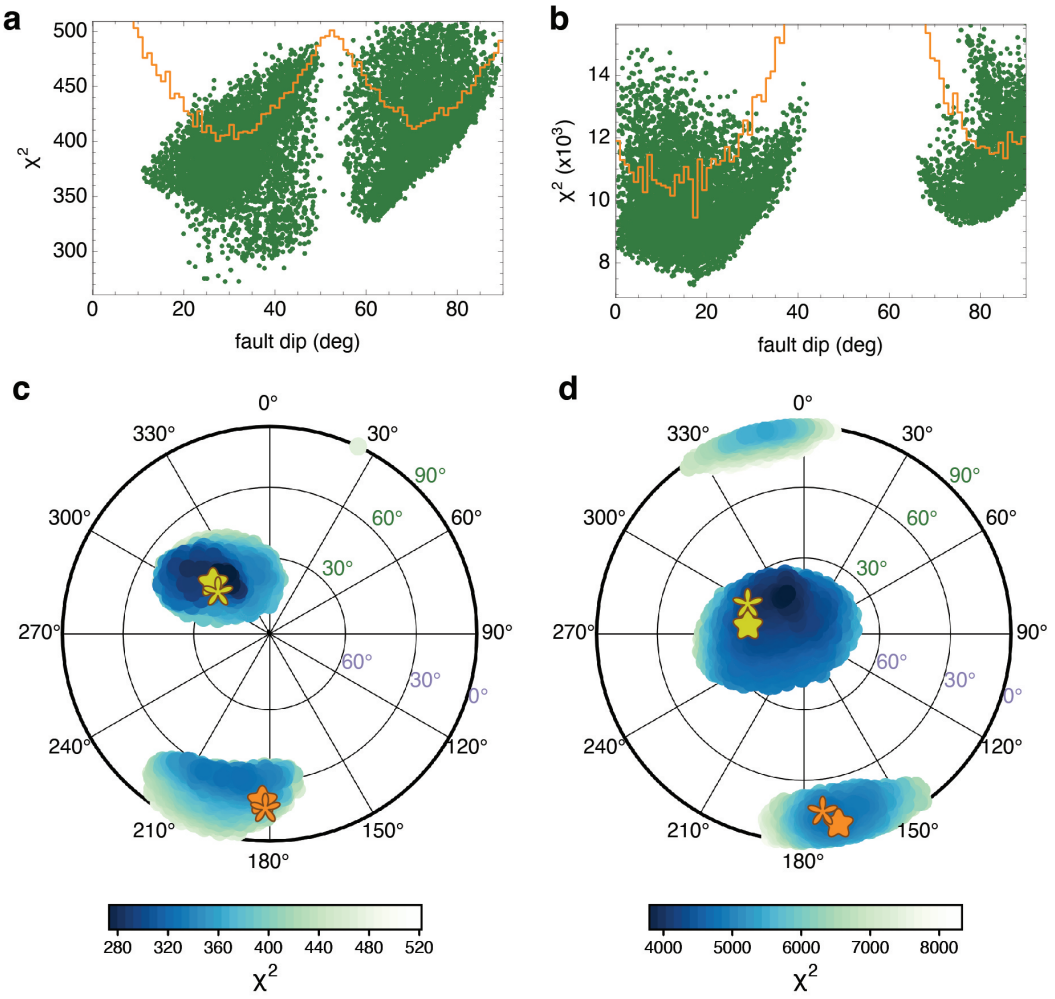


Figure 3.6: Model fit *vs.* fault dip in the 10,000 trial faults in the integrated search for the Jiashian (**a**) or MeiNong (**b**) coseismic slip models; orange lines in panels (**c**) and (**d**) are from Figs. 3.5a and 5b, respectively. Strike and dip of the fault planes in the trial models for the Jiashian (**c**) or MeiNong (**d**) earthquakes in the integrated search. Strike and dip are shown in a Lambert projection and colored according to the fit of the coseismic slip model. Values along the outer circumference indicate the strike of the fault plane, and numbers in the interior circles indicate either dip (green text) or codip (blue text); stars and asterisks depict the two nodal planes in the GCMT or USGS focal mechanisms, respectively.

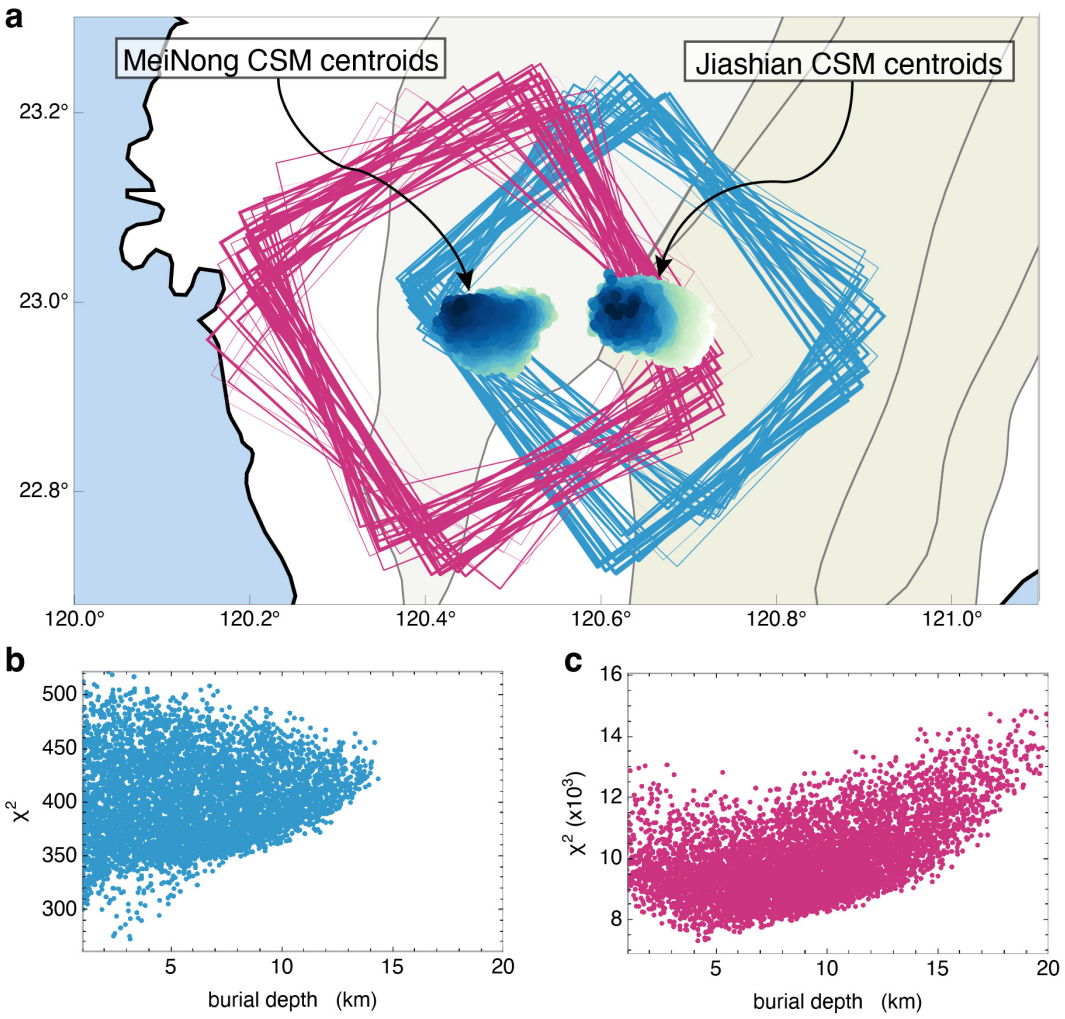


Figure 3.7: **a** Surface projections of the fault planes in the Jiashian (blue) and MeiNong (red) coseismic slip models with χ^2 within 10% of the best fitting model (38 and 107 models for Jiashian and MeiNong coseismic models, respectively; line thickness scales with χ^2). Also shown are the centroid locations of all 10,000 of the models in the integrated search, colored by χ^2 (coloring of Jiashian and MeiNong centroids as in Fig. 3.6a and 3.6b, respectively). Model fit *vs.* burial depths of all 10,000 trial models in the integrated search for the Jiashian (**b**) and MeiNong (**c**) earthquakes.

subfault, is 44° and 80° for the Jiashian and MeiNong earthquakes, respectively (3.2). While the average rake of the Jiashian coseismic slip model is comparable to the focal mechanism rakes of both the USGS and GCMT focal mechanisms (Fig. B.6), our inferred slip rake is characterized by more thrust slip than resolved by the focal mechanism (Fig. 3.8), a point we come back to in the Discussion section. Slip in the MeiNong earthquake is smoother and over a broader region than in the Jiashian earthquake, reflecting that the Laplacian smoothness regularization was dominant over the sparsity regularization in the MeiNong coseismic slip models. This was likely a combined result of our choice of a lower penalty parameter on the sparsity constraint and additional data in the MeiNong earthquake.

Both of the coseismic slip models contain slip at the edges of the fault plane domain, which we take to be model noise. Indeed, we find that slip in ensembles of all models within 10% of the best-fit χ^2 for each event, varies to an appreciable degree (38 and 107 models for the Jiashian and MeiNong earthquakes, respectively; Fig. 3.8). Both of the main slip patches are robust across the models in the ensembles of the two events. The ensemble varies less across most of the main fault for the Jiashian models compared to the MeiNong models, due to the fact that the sparsity constraint dominates in the Jiashian model owing to the lower number of data.

The predicted offsets at the GNSS stations from best fit coseismic slip models are quite close match to the observed GNSS velocities, both horizontal and vertical, for both earthquakes (Fig. 3.9; fit residuals are shown in Fig. B.4). Likewise, the predicted LOS for each of the interferograms is also a close match to the observed (Figs. 3.3 and 3.4; a comparison between the predictions at the quadtree samples for each of the interferograms is shown in Fig. B.5).

3.4 Discussion

The most surprising result of these inversions is that our best fitting coseismic slip model of the 2016 MeiNong earthquake is composed of a more northerly striking and larger thrust motion compared to focal mechanisms (3.2) and previously determined coseismic slip model of this earthquake (*cf.*, Figs. 3.1 and 3.7; Huang *et al.*, 2016, Qu *et al.*, 2017, Rau *et al.*, 2022). In contrast, our best fit Jiashian model not only agrees well with the focal mechanisms (3.1 and Fig. B.6), but the coseismic slip model proposed by Hsu *et al.* (2011). That our best Jiashian coseismic model is not a large deviation from prior models of this earthquake, indicates that there is no hidden bias in our estimation which is the cause of our inferred MeiNong coseismic model differing from prior models. We explore the relative support of our preferred MeiNong model over a model that is closer to the seismic focal mechanisms

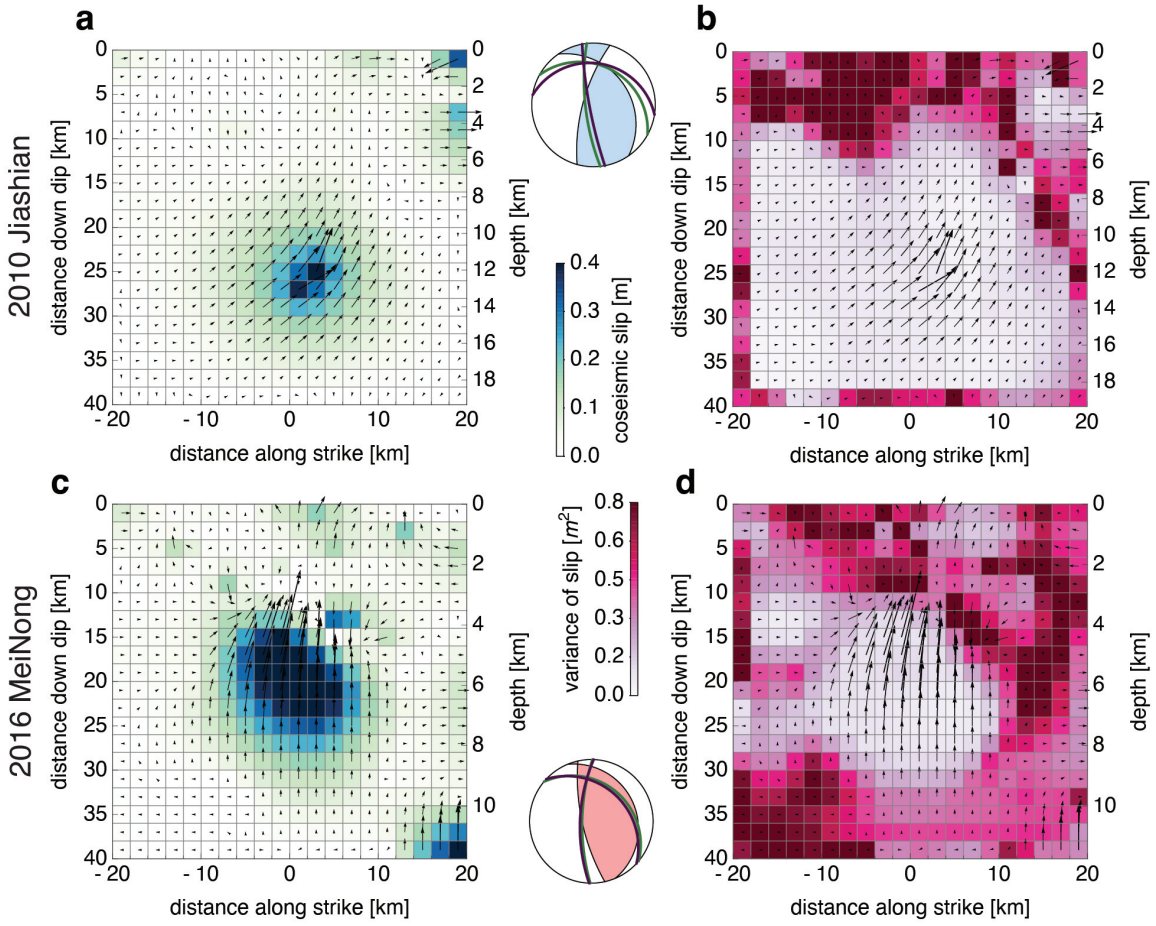


Figure 3.8: The slip distributions of the best fitting Jiashian (**a**) and MeiNong (**c**) coseismic slip models. To assess the degree to which the features of the slip are resolved, we plot the variance of the subfault slip in the coseismic models with χ^2 within 10% of the lowest χ^2 for the Jiashian (**b**; 38 models) and MeiNong (**d**; 107 models) earthquakes (all models used to compute the variance have strikes and dips similar to the best fit models; Fig. 3.7). Beachballs depict the double-couple focal mechanisms derived from the fault strike and dip, along with the weighted average slip rake, for each earthquake. Green and purple lines on the beachballs are the nodal planes from the USGS and GCMT focal mechanisms, respectively.

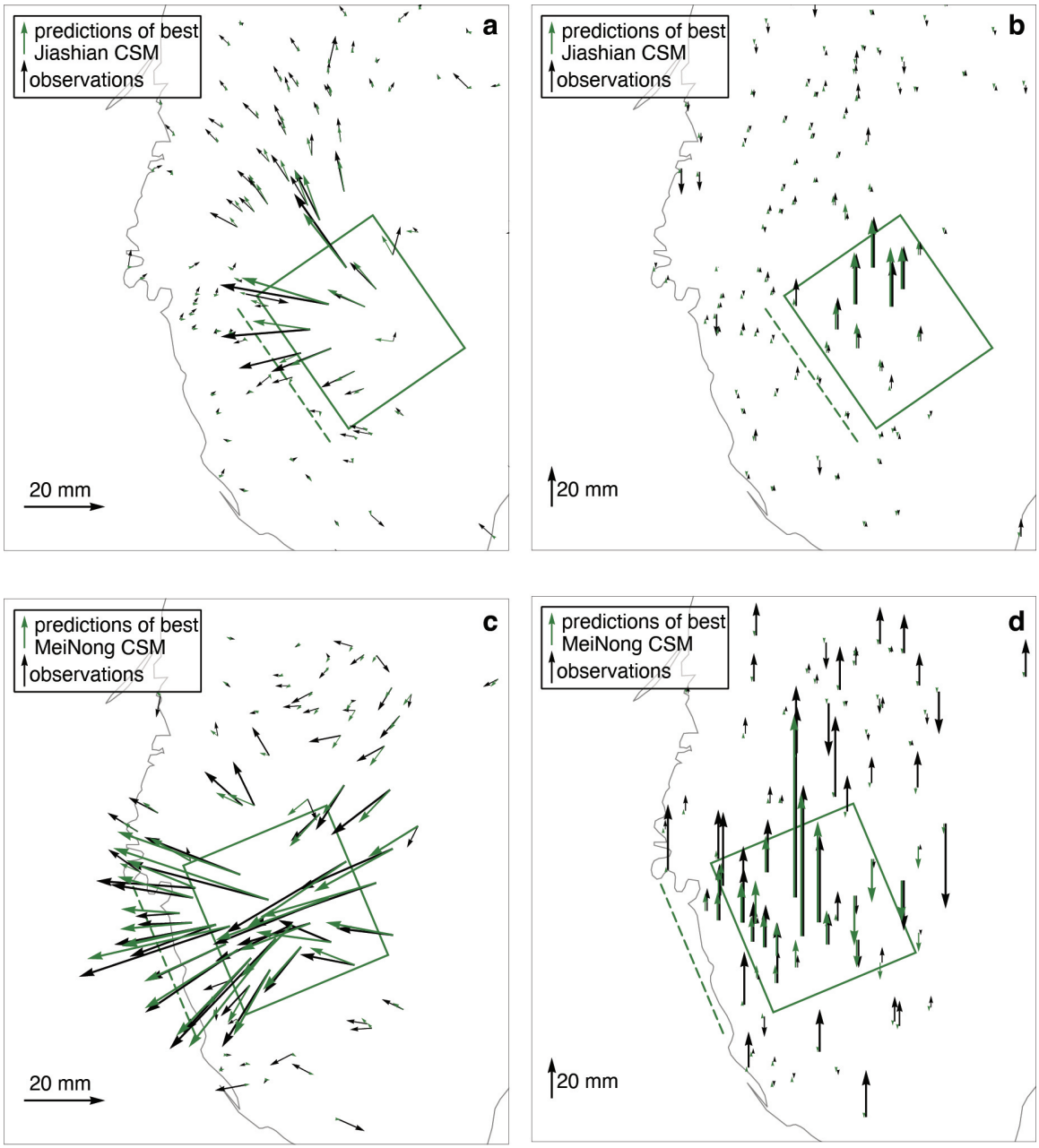


Figure 3.9: Predicted horizontal (**a** and **c**) and vertical (**b** and **d**) displacements for the best coseismic slip models determined of the Jiashian (**a** and **b**) and MeiNong (**c** and **d**) earthquakes. Vectors showing the model vertical displacements are slightly offset from the observed for clarity. The observed GNSS solutions are shown in black and are from Hsu *et al.*, 2011 (Jiashian; **a** and **b**) or Huang *et al.*, 2016 (MeiNong; **c** and **d**). Green rectangle is the surface projection of the fault planes and green dashed line is the projection of the top of the fault along the constant fault dip.

or previously determined models in the following subsection. We then explore the potential connection between our MeiNong and Jiashian models, suggesting that these two earthquakes occurred on the same fault structure.

3.4.1 Geodetic support of a shallower, more north striking, and largely thrust MeiNong coseismic model

In comparing our MeiNong model to past models, it is important to recognize potential biases that can arise due to incompletely searching all of the model space. This incomplete search might be due to limiting ranges of parameters searched over, or result from a decoupling the determination of different sets of parameters. The result of these biases might be a preference for some model features that are not the globally optimum.

Illustrating that decoupling estimation of different parameters can result in a bias, in our initial search over all fault geometry parameters assuming uniform fault slip, we find that a deeper fault with a more easterly strike and oblique slip provides the best fit to the geodetic data (3.1). Indeed, the strike we resolve in this best fit uniform search model (-63°) is quite similar to the strikes determined by Huang *et al.* (2016) (-61°) and Qu *et al.* (2017) (-72°), as well as strikes of the nodal plane most associated with the slip surface (Fig. 3.10). Moreover, the depth we find in the initial search (10.9 km) is comparable to the assumed depths of the faults in past coseismic models (Haung *et al.*, 2016; Qu *et al.*, 2017; Rau *et al.*, 2022) and focal depths (3.1). We note that when using only the testing InSAR to rank the model misfit, the best model found in the uniform slip search is a north-south striking fault (5°), but still at about the same depth (11.0 km). If we had fixed the fault geometry parameters based on an initial search assuming uniform slip, following standard practice in developing coseismic slip models (e.g.; Clark *et al.*, 1997), we would have determined a much different coseismic slip model than the best fitting model we present.

In our integrated search, varying both fault geometry patterns and inversion of distributed fault slip, our optimal solution is composed of a much shallower fault (4.1 km to the top of the fault plane) with almost pure thrust motion (rake of 80°; 3.1). Shallower faults and those with more thrust slip than strike-slip both result in larger vertical deformation. In that, we posit that allowing the search to encompass more shallow faults, results in a coseismic slip model that both fits the large vertical deformation to a better degree (Figs. 3.9c and d). Our preferred MeiNong coseismic model also is a good fit to the InSAR data, including to the interferograms that were unseen by the inversion (Fig. 3.11).

To further demonstrate that allowing shallower fault results in a more complete description of the geodetic data, we extract an alternative solution from the cloud of all 10,000 tested

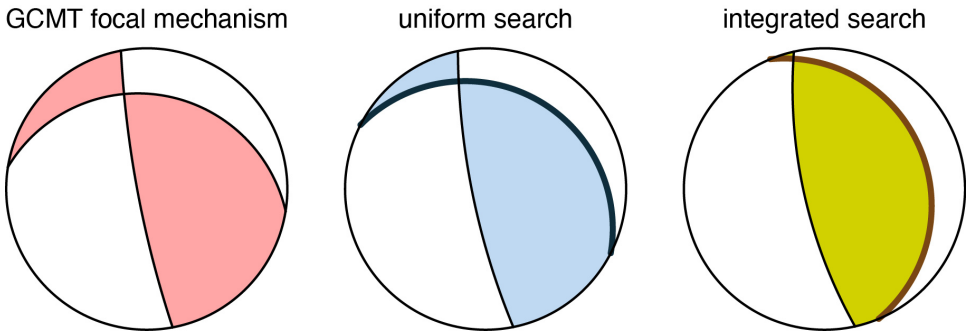


Figure 3.10: The GCMT focal mechanism of the MeiNong earthquake compared to the focal mechanisms for the best model found from the initial search assuming uniform slip and from the integrated search (the slip surface is highlighted).

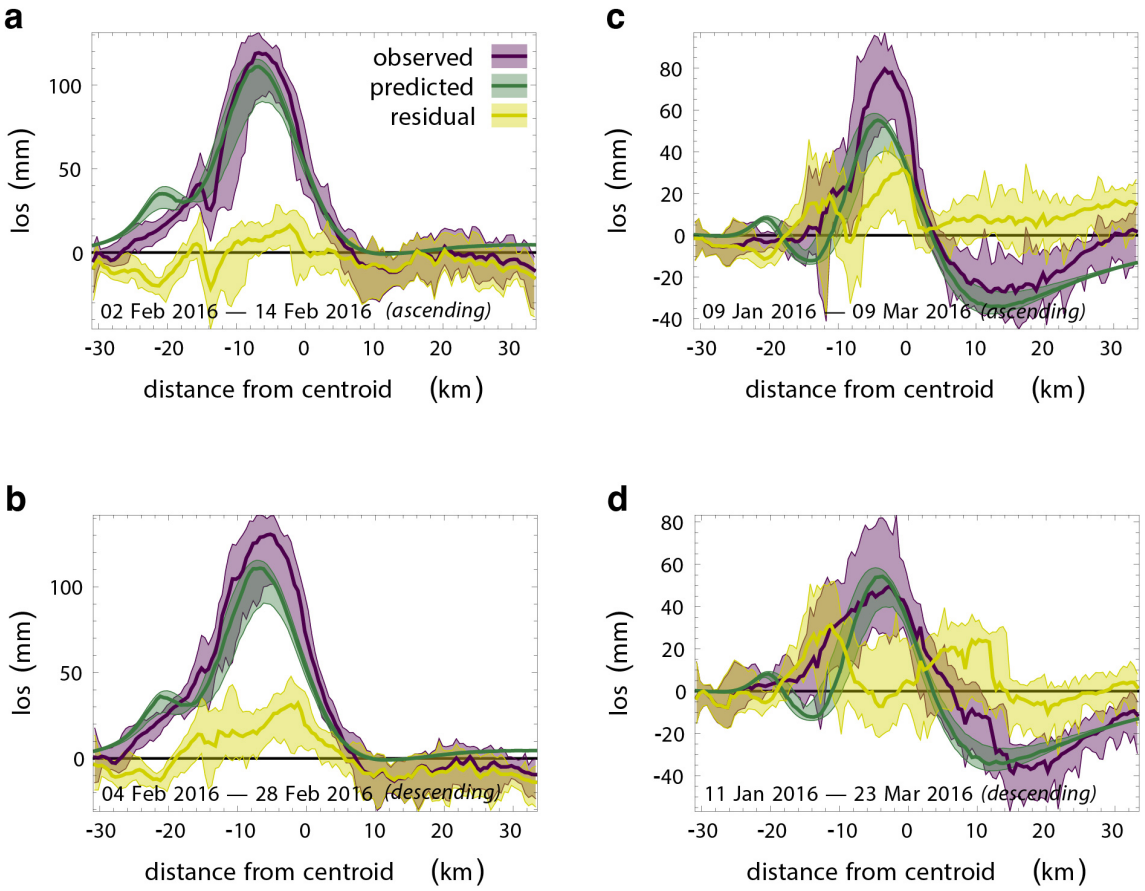


Figure 3.11: Line of sight (los) coseismic offsets for the MeiNong earthquake along the swath shown in Figs. 3.3 and 3.4, from southwest to northeast: profiles in (**a**) and (**b**) are from the training interferograms, either ascending or descending, respectively, while (**d**) and (**d**) are from the testing interferograms. Solid lines shows the median los offset within the swath, and shaded regions depict the range in which 90% of the los is along the swath (defined by the 5^{th} to 95^{th} percentiles).

models. This alternative model has a strike, dip, and average rake close to the primary nodal plane of the GCMT focal mechanisms (strike, dip, and weighted average rake are -83°, 20°, and 20°, respectively, all within 2° of the nodal plane of the GCMT solution). Additionally, the centroid depth of this alternative fault is 16.3 km, just slightly shallower than the GCMT centroid depth (3.2). This alternative model does not predict the horizontal GNSS observations as well as our preferred model (the χ^2 of this alternate model is about 40% larger than the best fit, which is the 4,524$^{\text{th}}$ best fit of all coseismic slip models with fault geometries with northeasterly dipping. More crucially there are quite large vertical GNSS residuals over the hanging wall of the fault (Fig. B.7). Likewise, the InSAR observations are under-predicted by this alternate model (Fig. B.8).

The previous coseismic models of the MeiNong earthquake were unable to explain all of the vertical deformation, leading the authors to appeal to either aseismic slip on a shallow fault in the hanging-wall (Huang *et al.*, 2016, Qu *et al.*, 2017) or mud diapirism (Rau *et al.*, 2022). Here we find little unexplained vertical deformation. To be clear, there are some vertical GNSS residuals (as the data errors on the vertical offsets are larger, the estimation favors explanation of the horizontal components), but there is no clear pattern of these residuals relative to the fault plane (Fig. B.4d). Indeed, the vertical residuals at stations over the hanging wall are generally smaller than the far field residuals (*cf.*, Figs. 3.9b and B.4d). Although interferometric data is sensitive to both vertical and horizontal deformation, we also do not see residual interferometric deformation that is unexplained by our preferred MeiNong model (Fig. 3.11). It is worthwhile reiterating that even the two interferograms that were not inverted are well described by the model (Figs. 3.11c and 3.11d). We will concede that there may be some component of aseismic deformation coincident with the MeiNong earthquake, but using a misfit between a coseismic slip model and the geodetic data is insufficient to argue for that additional deformation. In short, the available geodetic data is well explained by a simple cosiesmic model, without the need to appeal to aseismic processes.

While we contend that the differences between our best MeiNong coseismic model and previously published models arise from those earlier models constraining the allowable ranges of model parameters — most notably by assuming a given depth — the discrepancy between our MeiNong model and seismic focal mechanisms remains. That the inferred double-couple mechanism trades off with depth, as well as that depth itself trades off with the moment magnitude and is sensitive to the assumed velocity model, are well established in the literature (*e.g.*, Chang *et al.*, 2019). The depth of the centroid in our preferred MeiNong model is about half the depths given both by the USGS or GCMT (3.1). It is interesting to also note that the centroid depth of our preferred Jiashian coseismic model is also appreciably

shallower than the seismically determined depths (3.1). We demonstrate that deeper source faults are unlikely given the geodetic data (Figs. B.7 and B.8). Objectively, the geodetic data, both horizontal and vertical, are appreciably better fit by largely thrust slip on a shallower, northwest-southeast striking fault, compared to a model closer to previously proposed coseismic slip models.

3.4.2 Connecting the 2010 Jiashian and 2016 MeiNong earthquakes

Neglecting the imaged slip at the edges of the fault domains in each model, both of the final Jiashian and MeiNong coseismic models are composed well defined patches of slip (Fig. 3.8). Within the regions where slip is significant, there are differences between the imaged slip in the two models, but that difference is largely driven by differences in the relative constraints on sparsity *vs.* smoothness for these two earthquakes that are imaged by quite different data. The main slip patch of our MeiNong preferred model is adjacent to the main slip patch in the Jiashian model (Fig. 3.12a), with similar strikes of the faults (Fig. 3.7a). Additionally, the bottom edge of the MeiNong slip patch is roughly at the same depth as the top edge of the Jiashian slip patch (Fig. 3.12). The proximity of the slip patches suggests that these two earthquakes occurred on a single fault, steepening at depth. The oblique thrust slip rake in the Jiashian is close to the slip direction that would be expected from the background stress (Hsu *et al.*, 2011). The slip direction we resolve in our MeiNong earthquake is rotated towards pure thrust, suggesting that coseismic stress changes in the Jiashian earthquake perturbed the stress field at the MeiNong slip.

Our Jiashian coseismic slip model is broadly consistent with relocated aftershocks, where the aftershocks determined by Huang *et al.* (2011) all fall below the main slip patch we infer, and following the same dip (Fig. 3.12). In the developent of their coseismic slip model of the Jiashian earthquake, Hsu *et al.* (2011) use the general alignment of the Jiashian aftershocks to narrow their initial fault geometry search. That we find an alaignment with the aftershocks starting from a more open fault geometry search adds validation to the model of Hsu *et al.* (2020).

The comparison of our MeiNong cosiesmic model with the aftershocks of that earthquake is not as direct. The largest collection of MeiNong aftershocks is from Hsu *et al.* (2020), who located 524 aftershocks (Fig. 3.12). Taken together, those aftershocks describe a westward dipping plane of about 30°, quite contrary not only to our preferred MeiNong model, but the previously proposed coseismic slip models (Huang *et al.*, 2016, Qu *et al.*, 2017, Rau *et al.*, 2022). However, Hsu *et al.* (2020) noted that that aftershocks do not simply delineate

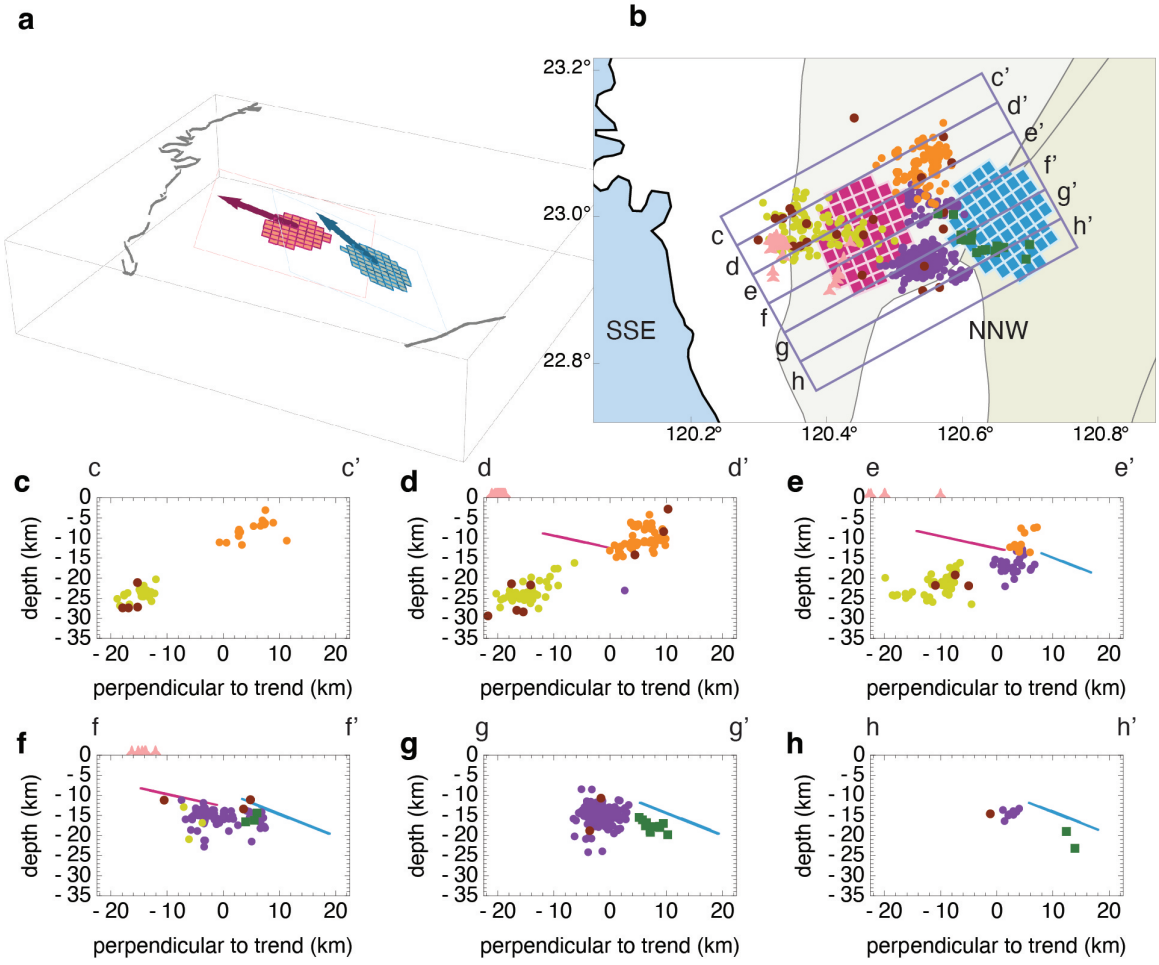


Figure 3.12: (**a**) Main slip patch of the Jiashian (blue) and MeiNong (red) coseismic slip models (defined as subfaults with slip $\geq 20\%$ of the maximum slip in each model, excluding subfaults at the edges of the fault domain, *cf.*, Figs. 3.8a and c); arrows are the weighted average slip direction of each coseismic slip model. (**b**) Map view of slip patches with epicenters of aftershocks determined by *Huang* et al. (2011; green squares, Jiashian aftershocks), *Wen* et al. (2017; dark red circles, MeiNong aftershocks), and *Hsu* et al. (2020; purple, orange, and gold circles, MeiNong aftershocks); pink triangles are locations where ground fissures were observed by *Yi* et al. (2023). (**c**–**h**) Cross sections indicated in **b**, symbols are aftershocks as in **b**, and blue or red lines are the main slip patch of the Jiashian or Meinong coseismic models, respectively.

a planar feature, but rather fall into three general clusters. Here we slightly modify their clustering by considering the depth of the aftershocks relative to the slip surfaces we infer in our coseismic models. The first two groups of MeiNong aftershocks are at the downdip edge of the main slip patch we image, one to the south and in the footwall, and one to the north in the headwall (Fig. 3.12). The third group of aftershocks is located deeper in the footwall, and delineate a west dipping plane (Figs. 3.12c–e). Based on proximity of the first two groups to the slip in our MeiNong coseismic model, we feel that these are relatively normal aftershocks associated with faulting. The aftershocks in these two groups, either individually or taken together, follow typical Omori-Utsu decays (Fig. B.9). In contrast, the aftershocks in the deeper, west dipping group, do not have such a simple relationship to the faulting. The heightened frequency of aftershocks in that group is delayed, with the peak number of aftershocks occurring one day after the MeiNong mainshock, and does not follow a typical Omori-Utsu decay (Fig. B.9c). Hsu *et al.* (2020) argued that the aftershocks in this group are related to fluid processes following coseismic stress changes in the MeiNong earthquake.

3.5 Conclusions

We revisit the coseismic deformation for the 2010 Jiashian and 2016 MeiNong earthquakes in southwestern Taiwan. We develop coseismic slip models of these two earthquakes, constrained by geodetic data and using the same estimation methodology. We find that a Jiashian coseismic model that is broadly consistent with seismologically determined focal mechanisms, as well as the coseismic model of Hsu *et al.* (2011). In contrast, we find that the geodetic data argues for a more northerly striking and shallower slip surface than is resolved in the focal mechanisms or in previously published coseismic slip models. The latter studies all constrained aspects of the fault geometry *a priori*, most notably the depth of the fault. We demonstrate that assumption of a deep fault likely led to biases in the final inferred coseismic slip model. Constraining fault geometry parameters using assumption of uniform slip would also lead to biases in the final coseismic slip model. As there are no systematic vertical residuals with our final MeiNong model, aseismic processes such as triggered creep on another fault structure or off-fault, volumetric deformation, do not need to be appealed to in order to explain the observed vertical coseismic offsets. The similarity of the fault strikes in our final coseismic models, along with proximity of the inferred regions of fault slip, suggests that these two earthquakes occurred on a single fault structure, dipping to the east and increasing with dip at depth. The majority of the aftershocks most closely related to the the MeiNong earthquake are located in the gap between the MeiNong and Jiashian

coseismic slip.

CHAPTER 4

Geodetic Data Fusion using Multi-Output Gaussian Processes

Abstract

Geodetic measurements of ground deformation are crucial to identifying and interpreting geophysical processes. When analyzing data from various geodetic techniques, the common approach is to treat the observations from each technique as distinct data streams. We present a method to fuse observations from multiple geodetic techniques, resulting in a single three-component deformation field spanning the entire spatial domain, complete with estimates of robust uncertainties, without any prior geophysical assumptions. Our fusion is built upon a semi-parametric latent factor model framework, combining a parametric mapping describing relationship between the geodetic techniques, and a non-parametric representation of the underlying, latent deformation field, which is determined through a multi-output Gaussian processes regression. Our geodetic data fusion technique exploits the complementary features of various data types to isolate spurious signals, thereby providing a more precise estimate of ground deformation. We consider coseismic deformation from the 2020 Sparta, NC, USA, and 2016 MeiNong, Taiwan, earthquakes, fusing interferometric synthetic aperture radar (InSAR) data with either light detection and ranging (LiDAR) data or global navigation satellite system (GNSS) data for the Sparta or Taiwan cases, respectively. The results show a significant improvement in the precision and coherence of the resolved deformation field. The strength of our methodology lies not only in its capacity to integrate diverse observational modalities and generate a continuous deformation field but also in its ability to characterize robust uncertainties within that field.

4.1 Introduction

Geodetic observations have played a critical role in the investigation of geophysical processes that result in the deformation of the surface, including earthquakes, fault creep, landslides,

volcanism, and group water variations. Indeed, Reid's theory of elastic rebound, which underpins our modern understanding of earthquakes and preceded the modern plate tectonic paradigm by about a half century, was formulated by comparing triangulation surveys conducted before and after the San Francisco earthquake of 1906 (*e.g.*, Lawson, 1908; Reid, 1909). Geodetic observations also add additional insight into seismic processes that is not captured by seismic data. For instance, the resolution of the geometry of the slip surface in the 1964 M9.2 earthquake was possible through geodetic observtions, whereas seismic data were unable to resolve which nodal plane corresponded to the slip surface (Plafker, 1965). Due to the groundbreaking advancements in technology, geodetic observations today have much higher precision and frequency, revealing even more insight into Earth deformation (*e.g.*, Herring *et al.*, 2010). Modern geodetic methods include the Global Navigation Satellite System (GNSS), of which the United State's Global Positioning System (GPS) is the longest operating system, Interferometric Synthetic Aperture Radar (InSAR), Light Detection And Ranging (LiDAR), and to several *in situ* instruments (*e.g.*, strain-meters, sea-floor pressure sensors). Each platform gathers measurements in their own unique way and provides a different view of surface deformation, with their own strengths and weaknesses. For example GNSS is quite sensitive to horizontal deformation but less so to vertical deformation, whereas InSAR has a larger sensitivity to vertical deformation compared to horizontal deformation. Moreover, GNSS is temporal dense and spatially sparse, while the converse is true for InSAR. LiDAR was initially used to develop precise digital elevation models, but recent advances in LiDAR data collection and processing, including the estimation of 3-D deformation fields through Iterative Closest Point (ICP) differencing, LiDAR is now proving to be a useful complement to GNSS and InSAR data (*e.g.*, Scott *et al.*, 2018; Szymanski *et al.*, 2024). ICP differencing is an interferometric approach, as is InSAR, although the current temporal irregularity of LiDAR surveys, effectively limits the use of LiDAR to investigation of static offsets.

Researchers typically treat data from different geodetic techniques as distinct data sets, optimizing a model of a geophysical process to fit the geodetic data, either individually or collectively (*e.g.*, Jonsson *et al.*, 2002; Simons *et al.*, 2002; Scott *et al.*, 2018). Models that consider only a specific type of data often resolve different features, and by simultaneously fitting all types of data the resulting model, in theory, captures the strengths of each of the data types (*e.g.*, Jonsson *et al.*, 2002; Delouis *et al.*, 2002), in essence using a geophysical model to leverage the individual strengths of each of the data types. Another approach is to use one modality of data to correct, or constrain, other data (*e.g.*, Lundgren *et al.*, 2009; Hammond *et al.*, 2018). For example, InSAR has an unknown absolute reference offset or may have long wavelength errors across the interferograms, which can be resolved by tying

the interferograms to GNSS observations (*e.g.*, Peltzer *et al.*, 2001; Lundgren *et al.*, 2009) or by using a GNSS constrained model (*e.g.*, Wei *et al.*, 2010).

We propose a new method to "fuse" geodetic data without reference to a model of a geophysical model. Data fusions, also referred to as sensor fusions, are common in various fields (*e.g.*, meteorology, medical imaging, aviation) and aim to incorporate information from two or more sources into a derivative data product that retains only signal common to all of the input data, leveraging the complementary nature of those data. Our data fusion method is based on Gaussian process regression and a semi-parametric latent factor model, and essentially follows from the methodology (Hines and Hetland, 2017). That earlier work only considered GNSS data, and thus was not a data fusion. Hines and Hetland (2017) used a Gaussian process regression to interpolate GNSS data in space and time to determine a spatiotemporally smooth deformation field which time-varying strain-rates could be derived from, and was coined PyGeoNS (*Py*thon-based *geo*detic *n*etwork *s*moother). We refer to our method as Gentoo moving forward, where "gen" derives from "*ge*odetic *n*etwork smoother" following Hines and Hetland (2017), and "too" loosely referencing the second evolution of PyGeoNS. At present, Gentoo only considers time-invariant deformation, either static offsets or secular velocities, and does not require observations from the various data sets be collocated. Gentoo results in an estimate of the three component surface deformation field, complete with estimates of the full uncertainties of that estimated field.

Earlier data fusions methods for InSAR data have been proposed, mostly fusing InSAR with GNSS data (*e.g.*, Gudmundsson *et al.*, 2002; Samsonov and Tiampo, 2006; Samsonov *et al.*, 2007; Samsonov *et al.*, 2008; Tong *et al.*, 2012; Wang and Wright, 2012; Banyai *et al.*, 2017; Shen and Liu, 2020; Qiu *et al.*, 2023), but a few using leveling (*e.g.*, Guglielmino *et al.*, 2011), LiDAR (He *et al.*, 2019), or Total Station measurements (*e.g.*, Muller *et al.*, 2015). Many of these proposed fusion methods use some flavor of least-squares regression (*e.g.*, Guglielmino *et al.*, 2011; Wang and Wright, 2012; Muller *et al.*, 2015; Banyai *et al.*, 2017; He *et al.*, 2019; Shen and Liu, 2020). These least squares methods either require an interpolated field for each input data type to get collocated samples (*e.g.*, Samsonov *et al.*, 2006; He *et al.*, 2019; Shen and Liu, 2020) or a subset of the input data contained within a given neighborhood around an arbitrary mesh point is regressed to estimate the deformation field at that mesh point (*e.g.*, Guglielmino *et al.*, 2011; Wang and Wright, 2012). Tong *et al.* (2012) use a multi-step process that involves using a interseismic velocity model estimated from GNSS data to constrain their 3D velocity field. Gudmundsson *et al.* (2002) and Samsonov and Tiampo (2006) use Markov random fields optimized by simulated annealing and minimization of Gibb's energy function, respectively. Here, the underlying assumption of independence between all but neighboring measurements imposed by the Markov property

prevents them from addressing dependencies between data types. In fact, all the previously mentioned studies, aside from Qiu *et al.*, (2023), treat each input data type as independent. Though this is unavoidable due to underlying assumptions of some of the proposed frameworks, and they are still able to produce valid, well-constrained deformation fields, they are still, self-admittedly in some cases (Samsonov, *et al.*, 2007), leaving valuable information provided by those dependencies unused. The fusion method proposed by Qiu, *et al.* (2023) is the closest comparison to Gentoo's framework in that it incorporates dependencies between data types, does not require collocation of observations, and provides an estimate of uncertainties in the form of a posterior covariance matrix. However, they use a simplistic projection of InSAR line-of-sight (LOS) observations into the vertical component of deformation based on the cosine of the radar incidence angle and they estimate the spatial covariance between GNSS and InSAR data through kriging. The estimation of vertical deformation in this manner makes significant assumptions about the contribution of the various deformation components to LOS range change and the choice of kriging to estimate spatial correlations between the data types entangles the inherent correlation structure of the underlying deformation field and noise covariance contained in the observations themselves. In contrast, as stated above, Gentoo makes minimal assumptions about the underlying signal, can ingest heterotopic data sets, and encodes the correlation structure of the underlying deformation and noise covariance separately in a rigorous manner.

Our proposed data fusion leverages the complementary nature of different geodetic techniques, in order to isolate noise structures unique to a particular technique, and result in a more accurate and precise estimate of the true ground deformation. For instance, InSAR data is well known to be corrupted by a myriad of spatially coherent signal that is not actual ground deformation (*e.g.*, Massonet and Feigl, 1998; Emardson *et al.*, 2003; Lohman and Simons, 2005; Simons and Rosen, 2015). Often these signals can be filtered from the interferograms using approximate models, such as bilinear ramps for residual orbital errors (*e.g.*, Shirzaei and Walter, 2011; Pritchard *et al.*, 2006), approximations of topology correlated tropo-static signal (*e.g.*, Delacourt *et al.*, 1998; Cavalié *et al.*, 2007; Lin *et al.*, 2010), or auxiliary data sources (*e.g.*, Li *et al.*, 2009; Bekaert *et al.*, 2015; Murray *et al.*, 2019). To isolate and remove these non-ground deformation signals, researchers have proposed "stacking" interferograms (*e.g.*, Peltzer *et al.*, 2001; Gourmelen and Amelung, 2005; Hetland *et al.*, 2012), although the appropriateness of the manner in which the interferograms are stacked is quite important (Simons and Rosen, 2015). Analogous to these stacking methods, Gentoo seeks to leverage the individual strengths of different geodetic data types to beat down noise, not only in the interferograms but across all of the data. Specifically, the resulting fused deformation field contains deformation that are are common to all of the input data, where

that input data overlaps spatially.

In the following section, we describe our proposed geodetic data fusion method, Gentoo. After describing how the semi-parametric latent factor model formulates the correlation structure of the data types, we review the theory of Gaussian process regression for both single and multiple data types, referred to as single-output and multi-output, respectively. We discuss covariance models that can be used to describe the prior on the underlying latent three-dimensional deformation field, introducing a new covariance model capable to capturing discontinuities in the latent deformation field, and how to estimate the hyper-parameters of the prior covariance models. We then demonstrate Gentoo for coseismic ground deformation from the M_w 6.3 2016 Meinong, Taiwan and M_w 5.1 2020 Sparta, North Carolina, USA earthquakes. For the Meinong earthquake we fuse GNSS measurements (Huang *et al.*, 2016) with two InSAR interferograms, from ascending and descending orbits of the European Space Agency's Sentinel-1A/B satellite. For the Sparta earthquake, we use fuse ICP differencing LiDAR data (3) with two ascending interferograms, one from Sentinel-1A/B (3) and one from Japan Aerospace Exploration Agency's Advanced Land Observing Satellite 2 (Wicks and Chiu, 2022). While the fused deformation fields can be used to constrain geophysical models, or to derive strain-fields (*e.g.*, Hines and Hetland, 2017), our focus on these examples is to demonstrate that even with limited input data, the resulting deformation fields are robust and effectively de-noise the input data. Specifically, we show that anomalous signals resulting from the built environment in the Sparta interferograms, as described by Szymanski *et al.* (2024), are effectively removed.

4.2 Fusion Architecture

We cast Gentoo within a semi-parametric latent factor model (SLFM; Teh *et al.*, 2005), which provides a structure in which to fuse multiple types of geodetic observations together. Specifically, an SLFM codifies that different types of geodetic observations (*i.e.*, response variables of the SLFM) are linear mixture of the underlying components of the deformation field (*i.e.*, latent variables of the system), as

$$\mathbf{v} = \Phi\mathbf{u}, \tag{4.1}$$

where $\mathbf{v} \in \mathbb{R}^C$ contains the observations, $\mathbf{u} \in \mathbb{R}^P$ is the latent deformation, and $\Phi \in \mathbb{R}^{C,P}$ is a linear mixture matrix relating the two. The dimension of $\mathbf{u}$ includes both the number of locations where measurements are made and how many components of ground deformation those measurements are sensitive to. For example, in the case where geodetic

data sample offsets at N points and all of those measurements are sensitive to all three components of surface deformation, $P = 3{\times}N$. The dimension of $\mathbf{v}$ is just the number of geodetic observations, of any type. Φ is then a mapping between the *a priori* unknown underlying deformation field and the geodetic observations at hand. We assume $\mathbf{v}$ and $\mathbf{u}$ to be nonparametric (*i.e.*, not described by a particular functional form), while Φ includes the parametric description of the specific geodetic technique depends on $\mathbf{u}$, hence the name "semi-parametric latent factor model."

The components of Φ reflect the geometry of the various observations relative to the underlying deformation field. Where observations coincident with the components of deformation (*e.g.*, components of GNSS data, leveling data), will have a one-to-one relationship, while other types of geodetic observations will be some weighted combination of the components of the underlying deformation field. While in general, these weights in Φ can be learned themselves (*e.g.*, Teh *et al.*, 2005), although in the case of geodetic observations, the specifics of the technique prescribe what the weights are. For instance, with InSAR line-of-sight measurements, the components of the satellite look vectors are the weights. Including only GNSS observations, as in Hines and Hetland (2017), Φ is just the identity matrix, with dimension of $\mathbf{v}$ and $\mathbf{u}$ $3{\times}N$, where N is the number of GNSS monuments. For two of the demonstrations we consider here, fusing either GNSS offsets or LiDAR-derived offsets with two InSAR interferograms (assuming time-invariance),

$$\Phi = \begin{bmatrix} I_e & 0 & 0 \\ 0 & I_n & 0 \\ 0 & 0 & I_v \\ H_{\alpha,e} & H_{\alpha,n} & H_{\alpha,v} \\ H_{\beta,e} & H_{\beta,n} & H_{\beta,v} \end{bmatrix} \tag{4.2}$$

where $H_{\alpha,i}$ are matrices containing the ith look vector component for viewing geometry of interferogram α, and similarly for interferogram β.

We treat the latent deformation field as a Gaussian process, defined as

$$u(\mathbf{x}) \sim \mathcal{GP}(m(\mathbf{x}), k(\mathbf{x}, \mathbf{x}')), \tag{4.3}$$

where $\mathbf{x} \in \mathbb{R}^2$ is position, $u(\mathbf{x})$ is multi-valued function describing the three components of surface deformation (*e.g.*, easting, northing, and vertical deformation), $m(\mathbf{x})$ and $k(\mathbf{x}, \mathbf{x}')$ are the mean and covariance functions, respectively, and the standard notation $\sim$ denotes that $u(\mathbf{x})$ follows the given probability distribution (*i.e.*, that $u(\mathbf{x})$ is any function that is within the Gaussian process distribution of functions). Note that $m(\mathbf{x})$ is not the average

function that describes a specific latent field, but is rather a statement of expectation of what that latent field is in absence of data. In that, we assume that $m(\mathbf{x})$ is zero, as is standard practice, and thus the Gaussian process distribution is entirely defined by $k(\mathbf{x}, \mathbf{x}')$. The vector $\mathbf{u}$ is then a realization of the the Gaussian process at specific sample points $\mathbf{x}_*$.

We can cast the geodetic observations in a general functional form as

$$v(\mathbf{x}) = \varphi\left(u(\mathbf{x})\right) + \epsilon, \tag{4.4}$$

where φ encapsulates the parametric relationships of the geodetic observation to the ground deformation (*i.e.*, the equivalent to to Φ in Eq. (4.1)), and $\epsilon \sim \mathcal{N}(0, \sigma_s^2)$ are the alleatoric data uncertainties. Importantly, inclusion of errors not only improves the veracity of the resultant model, but also improves numerical stability of the Gaussian regression (Williams and Rasmussen, 2006; Murphy, 2012). It is worth reiterating that Eq. (4.4) defines observations to be parametrically related to the unknown $u(\mathbf{x})$ with added noise. We are then left with the problem of determining $u(\mathbf{x})$, in other words regressing $v(\mathbf{x})$ onto $u(\mathbf{x})$, which we do via Gaussian process regression. In Gaussian process regression the *a priori* unknown $u(\mathbf{x})$ is estimated as a probability distribution over a general function space.

4.2.1 Gaussian processes regression

Gaussian process regression is a Bayesian inference technique that is used widely in the machine learning community (Williams and Rasmussen, 2006; Murphy, 2012). Here "regression" is used in a broad sense, to mean the estimation of a field representing an underlying signal from which the observations have been sampled, as opposed to more common parlance where "regression" refers specifically to estimation of parameters of an underlying parametric model. Being Bayesian at its core, Gaussian process regression provides a robust framework for updating observational uncertainties to reflect knowledge gained. Gaussian process regression results in well-defined, continuous probability distributions of $u(\mathbf{x})$, from which deformation at specific points can be sampled, along with their associated uncertainties. In the case of Gentoo, as also in PyGeoNS (Hines and Hetland, 2017), the probability distribution resulting from the input GNSS data fully describe the deformation field at every point in the domain. The differentiation of that distribution gives the probability distribution of strain-rates, which can be sampled to determine strain-rates at any point within the domain complete with their uncertainties.

The work of Hines and Hetland (2017) only considered the three components of GNSS data as input to infer one, multi-component output field, and is an example of a so-called single-output Gaussian process regression (SOGP). A Gaussian process regression can also

be posed to combine several types of input data to infer the same multi-component output field, a so-called multi-output Gaussian process regression (MOGP). The nomenclature of how the variants are referred to can be somewhat misleading in our application, as our aim is to use multiple types of input data to produce a single, multi-component output field. In that, the end product of the method we present here is the same as that in PyGeoNS, although in that earlier work, Hines and Hetland (2017) treated each component was treated independently, neglecting any potential cross correlations between the components, either in the input GNSS data or the components of the output fields. In that, PyGeoNS is three parallel Gaussian process regressions, each independently estimating a single component of the deformation field. The assumed lack of correlation between components is known to not be true. For instance different components of GNSS data are highly correlated (*e.g.*, Herring *et al.*, 2016), correlations which would result in correlations between the components of the output deformation field. More crucially, considering correlations is necessary when the input data are not colinear with a single component of the latent deformation field. For instance, the single LOS component of InSAR is dependent, to varying degrees, on all three primary components of the deformation. When combined with other types of data that are also sensitive the the same deformation components, for instance combining InSAR and GNSS, there are induced corellations between the input data themselves. The linear mixture coefficients included in Φ of Eq. (4.1) encode the conditional dependencies between different data types, and the associated correlations between components of the resulting output field.

4.2.1.1 Single-output Gaussian process regression

In a single-output Gaussian process regression, Φ is just the identity matrix, and the observations are

$$v(\mathbf{x}) = u(\mathbf{x}) + \epsilon. \tag{4.5}$$

Both the *a priori* unknown $u(\mathbf{x})$ and the known $v(\mathbf{x})$ are Gaussian processes. Note that the observation vector is a specific realization of $v(\mathbf{x})$, $\mathbf{v} = v(\mathbf{x}_o)$, where $\mathbf{x}_o$ are the locations at which observations are known. $u(\mathbf{x})$ is estimated from those noisy observations as probability distribution, and we see that Gaussian process regression is merely a non-parametric interpolation (*e.g.*, Williams and Rasmussen, 2006).

Leveraging the marginalization property of Gaussian processes, which states that any finite subset of a Gaussian process follows a joint Gaussian distribution (Williams and Rasmussen, 2006; Murphy, 2012), the joint prior distribution of $\mathbf{v}$, along with $u_* = u(\mathbf{x}_*)$ where

$\mathbf{x}_*$ is any desired set of sample locations within the domain, is given by

$$\begin{bmatrix} \mathbf{v} \\ u_* \end{bmatrix} \sim \mathcal{N}\left(\begin{bmatrix} \mathbf{0} \\ 0 \end{bmatrix}, \begin{bmatrix} K(\mathbf{x}_o, \mathbf{x}_o) + \Sigma & K(\mathbf{x}_o, \mathbf{x}_*) \\ K(\mathbf{x}_*, \mathbf{x}_o) & K(\mathbf{x}_*, \mathbf{x}_*) \end{bmatrix} \right). \tag{4.6}$$

In Eq. (4.6), Σ is the data covariance matrix and K is the covariance matrix describing the *a priori* correlation structure of the latent deformation field. $K(\mathbf{x}_o, \mathbf{x}_o)$ is the covariance with respect to the observation locations, $K(\mathbf{x}_*, \mathbf{x}_o)$ and $K(\mathbf{x}_o, \mathbf{x}_*)$ are cross-covariances of the latent field between the observation and sample locations, and $K(\mathbf{x}_*, \mathbf{x}_*)$ is the covariance between sample locations. It is worth reiterating, that K is an *a priori* on the covariance structure of the latent field $u(\mathbf{x})$, which is to say the spatial covariances that are *believed* to be present in the deformation field. As with all Bayesian estimation schemes, the prior can be set as narrowly or widely as desired (*e.g.*, Tarantola, 2005); however, in the case of Gaussian process regression, a fully non-informative prior is not possible, as it would result in an ill conditioned K. With the prior defined, Gaussian process regression then uses Bayes theorem to condition the prior on the observations, giving the posterior distribution as

$$\hat{u}_* = \hat{u}(\mathbf{x}_*) = K(\mathbf{x}_o, \mathbf{x}_*)^T \left[K(\mathbf{x}_o, \mathbf{x}_o) + \Sigma\right]^{-1} \mathbf{v} \tag{4.7}$$

and

$$\Sigma_* = \mathrm{cov}(\mathbf{u}_*) = K(\mathbf{x}_*, \mathbf{x}_*) - K(\mathbf{x}, \mathbf{x}_*)^T \left[K(\mathbf{x}_o, \mathbf{x}_o) + \Sigma\right]^{-1} K(\mathbf{x}_o, \mathbf{x}_*), \tag{4.8}$$

where $\hat{u}_*$ is the most likely estimate of a single component of the latent deformation field and Σ_* is the covariance of that estimate.

4.2.1.2 Multi-output Gaussian process regression

The downsides to using a single-output GPR are that correlations between deformation components are ignored, as noted by Hines and Hetland (2017), and the input data is constrained to be coincident with the components of the latent deformation field (*i.e.*, the relationship between the data and latent field would have to follow Eq. (4.5)). A single-output Gaussian process regression can be generalized by mapping the prior K to a new covariance matrix, K_M, on the geodetic observations. The mixture matrix Φ in the SLFM provides the mapping, via a standard propagation of Gaussian uncertainties, as

$$K_M = \Phi K \Phi^T. \tag{4.9}$$

K_M includes the covariances between the components of the latent deformation field and the multiple data types. By including the general K_M, the input data are not constrained

to be coincident with the latent field components (*i.e.*, with general data description as in Eq. (4.4)).

Following Eqs. (4.7) and (4.8), all components of the deformation field are estimated by

$$\hat{u}_* = \hat{u}(\mathbf{x}_*) = K_M(\mathbf{x}_o, \mathbf{x}_*)^T \left[K_M(\mathbf{x}_o, \mathbf{x}_o) + \Sigma\right]^{-1} \mathbf{v} \tag{4.10}$$

and

$$\Sigma_* = \mathrm{cov}(\mathbf{u}_*) = K_M(\mathbf{x}_*, \mathbf{x}_*) - K_M(\mathbf{x}, \mathbf{x}_*)^T \left[K_M(\mathbf{x}_o, \mathbf{x}_o) + \Sigma\right]^{-1} K(\mathbf{x}_o, \mathbf{x}_*), \tag{4.11}$$

where Σ is a covariance matrix of all of the input data and $\mathbf{v}$ contains all of the input data. For C types of input data,

$$K_M(\mathbf{x}, \mathbf{x}') = \begin{bmatrix} K_{11}(\mathbf{x}, \mathbf{x}') & \cdots & K_{1C}(\mathbf{x}, \mathbf{x}') \\ \vdots & \ddots & \vdots \\ K_{C1}(\mathbf{x}, \mathbf{x}') & \cdots & K_{CC}(\mathbf{x}, \mathbf{x}') \end{bmatrix}, \tag{4.12}$$

where $K_{ii}(\mathbf{x}, \mathbf{x}')$ is the prior covariance matrix mapped onto each observation type and $K_{i \neq j}(\mathbf{x}, \mathbf{x}')$ is the cross-covariance between the observation types — these covariances fully describe the covariance of the components of the estimated deformation field. By using the formalism of Eq. (4.1), we are able to account for conditional dependencies between samples in v and the latent variables in u. As such, the inclusion of the cross-covariance blocks in Eq. (4.12) allows for a sharing of statistical strengths, or "transfer learning" in machine learning parlance, between different data types.

4.2.2 Construction of the prior covariance

The prior covariance matrix K, and through mapping of the SLFM, K_M, strongly influences the posterior deformation field, both the most likely given by Eq. (4.10) and the covariance structure given by Eq. (4.11). Σ_* includes the uncertainties of the most likely estimate of deformation at the sample locations, along with the covariances between deformation components and the spatial correlations of the predicted deformation field between neighboring locations. The Gaussian process regression conditions the prior, $K(x_*, x_*)$, to the posterior covariance, Σ_* (Eq. 4.8). K is constructed via a covariance model, or kernel, and we denote the collection of the controlling parameters of that kernel (*i.e.*, the hyper-parameters) as $\mathbf{\Theta}$. There are many different flavors of covariance functions, but all must produce valid covariance matrices (*i.e.*, matrices that are symmetric and positive semi-definite).

4.2.2.1 Squared-exponential covariance function

A commonly used covariance function is the smooth and continuously differentiable, squared-exponential

$$k_{SE}(\mathbf{x}, \mathbf{x}') = \sigma_f^2 \exp\left(-\frac{1}{2}(\mathbf{x} - \mathbf{x}')^T P^{-1}(\mathbf{x} - \mathbf{x}')\right), \tag{4.13}$$

where σ_f^2 is the signal variance, P is a diagonal matrix containing the square of the correlation length scales for each dimension. The collection of the length scales are referred to as the kernel hyper-parameters, which we denote $\mathbf{\Theta}$.

4.2.2.2 Discontinuous squared-exponential covariance function

The allowance for a discontinuity within the estimated field is accomplished by reducing the correlation between points on opposing sides of a known discontinuity, for instance the mapped surface rupture of an earthquake or a creeping fault. This necessitates prior knowledge of the location of the discontinuity and results in a non-stationary covariance function, meaning covariance values are no longer simply dependent on the distance between two points but also their position. We begin with an isotropic squared-exponential covariance function

$$k_{SE} = \sigma_f^2 \exp\left(\frac{r^2}{2l^2}\right) \tag{4.14}$$

where r is the distance between the two locations being considered and l is the scalar characteristic length scale. If the line segment between the two locations intersects the surface rupture, we take r to be the sum of the distances between each location and the terminal end of the surface rupture that results in the shortest path around the surface rupture. As a consequence of this increase in r, the covariance between the two locations is reduced (Fig. S1). Note that when including the location of a discontinuity, there is no ad hoc enforcement on the magnitude of the offset across that discontinuity (*i.e.*, the estimated field could be continuous across a fault trace), and any offsets resolved in the estimated deformation field are entirely driven by the data themselves.

4.2.2.3 Estimation of prior covariance hyper-parameters

Many approaches exist for determining hyper-parameter values for kernel functions, including arbitrary user choices, variography, or optimization. Where the choice of kernel function dictates the general characteristics, the hyper-parameter values can be tuned to capture more nuanced aspects of the data. An *a priori* choice of the hyper-parameters may be appropriate when there is a clear connection between a given hyper-parameter and some characteristic of an underlying process. For instance, a particular magnitude of earthquake

at a given depth may regularly produce a certain spatial footprint of deformation, which can guide the selection of a the characteristic length scale for the SE kernel. Variography is only possible when the kernel under consideration contains a variogram model, which limits the choice of kernel. It is important to note that variography of the original data does not discriminate between data covariances and the covariance structure of the latent field, and while it can be used to determine the covariance structure of the data noise (*e.g.*, Lohman and Simons, 2005), that should not be confused with the covariance structure of the latent field.

Here we approach the selection of the hyper-parameters describing the covariance structure of the latent field through a minimization of the negative log-marginal likelihood (NLML). In the two example cases we consider, we assume a squared-exponential covariance model, with hyperparameters $\theta = (\sigma_f, l)^T$. For that θ the equation for the NLML is given by

$$-\log p(\mathbf{r}|\mathbf{x}_o, \theta) = \frac{1}{2}\mathbf{r}^T \left[K_M + \Sigma\right]^{-1} \mathbf{r} + \frac{1}{2}\log\left|K_M + \Sigma\right| + \frac{n}{2}\log 2\pi \tag{4.15}$$

. The first term can be viewed as a measure of data-fit where r is the residual vector and expanding $K_M + \Sigma$ to $\Phi K \Phi^T + \Sigma$ is the estimation of the posterior covariance. The interpretation of this term is different than that of a typical misfit measure; where both quantify how close the predictions are the observations, in a typical misfit that misfit is relative to the observation uncertianties, whereas here the misfit is relative to the posterior covariance of the latent field. In other words, while a misfit is quantifying how well the predictions match the observations, the quantification in the first term of equation (4.15) is how well the observations are matching the predicted field. The remaining terms in the NLML are equivalent to the differential entropy of a multi-variate Gaussian up to a constant (Thomas and Joy, 2006), as such can viewed as aiming to find hyper-parameter values that minimize information loss during optimization. Taken in conjunction, minimization of the NLML is attempting to balance the predictive accuracy and how well the overall uncertainty of the resolved field is reduced by the selected model.

4.2.3 Construction of the observational covariance

The covariance matrix, Σ, describes the uncertainties and correlations in the input data. For C types of independent input data,

$$\Sigma = \begin{bmatrix} \Sigma_{11} & \Sigma_{12} & \cdots & \Sigma_{1C} \\ \Sigma_{12} & \Sigma_{22} & \cdots & \Sigma_{2C} \\ \vdots & \vdots & \ddots & \vdots \\ \Sigma_{1C} & \Sigma_{2C} & \cdots & \Sigma_{CC} \end{bmatrix}, \tag{4.16}$$

where Σ_{ii} is the covariance matrix for the i^{th} input data type, and $\Sigma_{i \neq j}$ are the cross-covariances between the input i and j data types. As we are treating each component of a multi-component geodetic technique as a separate input data type, $\Sigma_{i \neq j}$ would include the covariances between the components of the geodetic technique. In contrast, for two distinct data types, such as GNSS and InSAR, the associated cross-covariance would be a zero matrix.

The diagonals of Σ_{ii} are the squares of individual data uncertainties, while the off diagonals give the spatial covariances of the geodetic data. The spatial covariance structure might be known by the data processing, or estimated via variography from the data, as it is in InSAR (*e.g.*, Emardson, 2003; Lohman, 2005). As a side note, using a squared exponential kernel, optimized to describe the estimated spatial covariance structure in the data, as the prior covariance in a Gaussian process regression effectively reduces it to kriging. As Σ_{ii} is the covariance structure of the noise in the data, ideally if it is estimated from the data, one should do so in an area of the data that is signal free, or as close to as possible. Here we only assume that the InSAR and LiDAR data spatial covariances, which we assume can be estimated via variography on data away from the probable area of the signal, following Lohman (2005).

4.3 Demonstrations

As proof-of-concept demonstrations, we consider coseismic deformation from two earthquakes. We limit our demonstrations to coseismic deformation, as currently we only solve for time invariant deformation. Additionally, as earthquakes generate large enough surface offsets, and of relatively distinctive pattern, the evaluation of the results is straightforward. We choose two moderately small magnitude earthquakes, the magnitude 6.4 2016 MeiNong earthquake in Taiwan and the magnitude 5.1 Sparta earthquake in North Carolina, USA, as demonstrations. In both demonstrations two types of geodetic data are fused to result in an

estimate of the latent deformation field. In the case of MeiNong, the data is characterized by a moderate signal-to-noise ratio, with expected pattern of coseismic deformation readily identified in the GNSS data (*e.g.*, 3). In contrast, the data in the Sparta earthquake has much lower signal-to-noise ratio (Szymanski et al., 2024), and serves to be a demonstration of the de-noising aspect of our data fusion technique. Additionally, we choose these two earthquakes as demonstrations since the appropriate prior covariance for each is quite different. The MeiNong earthquake did not produce a surface break, resulting in spatially smooth coseismic deformation, allowing us to use a standard squared exponential as a prior. In contrast, the smaller Sparta earthquake did produce a surface break, resulting in discontinuous coseismic deformation across the break, which makes the use of a smooth, stationary kernel problematic.

4.3.1 Coseismic deformation of the 2016 Meinong earthquake

We first consider the coseimsic deformation of the 2016 M6.4 MeiNong earthquake. We fuse three component coseismic displacements from 75 GNSS (Huang *et al.*, 2016; Figs. 4.1a and b), with two interferograms derived from from SAR scenes acquired by the Sentinel-1 satellite (European Space Agency), one ascending and one descending interferogram (Figs. 4.1c and d). Both interferograms are produced from scenes with the shortest time span bracketing the earthquake, 12 days for the ascending pass and 24 days for the descending pass, including 9 and 23 days of the postseismic period for ascending and descending, respectively. These interferograms are the training interferograms from 3, and are fully described there. We also developed two independent interferograms in 3, which could also be used as input to the fusion, but we opt not to in the present work. Including multiple interferograms with the same viewing geometry will further reduce the noise in the fused deformation field, as we discuss more below; however, our present focus is on the impact of different geodetic techniques in the fusion.

Since it would be computationally intractable to use the full interferograms, we use random sampling as input for our fusion (this procedure scales as $\mathcal{O}\left(n^3C^3\right)$, where C is the number of data, a point we come back to in the Discussion section). The samples size are 8790 and 10419 for the ascending and descending interferograms, respectively. These number of samples correspond to 0.14% and 0.15% of the line-of-sight measurements in the original interferograms. We use the standard SE kernel for the prior covariance of the underlying deformation field. We learn the hyper-parameters of the SE kernel, including σ_f^2 and l, by minimizing the negative log-marginal-likelihood, finding optimum values 0.0014 m^2 and 10.0 km, respectively.

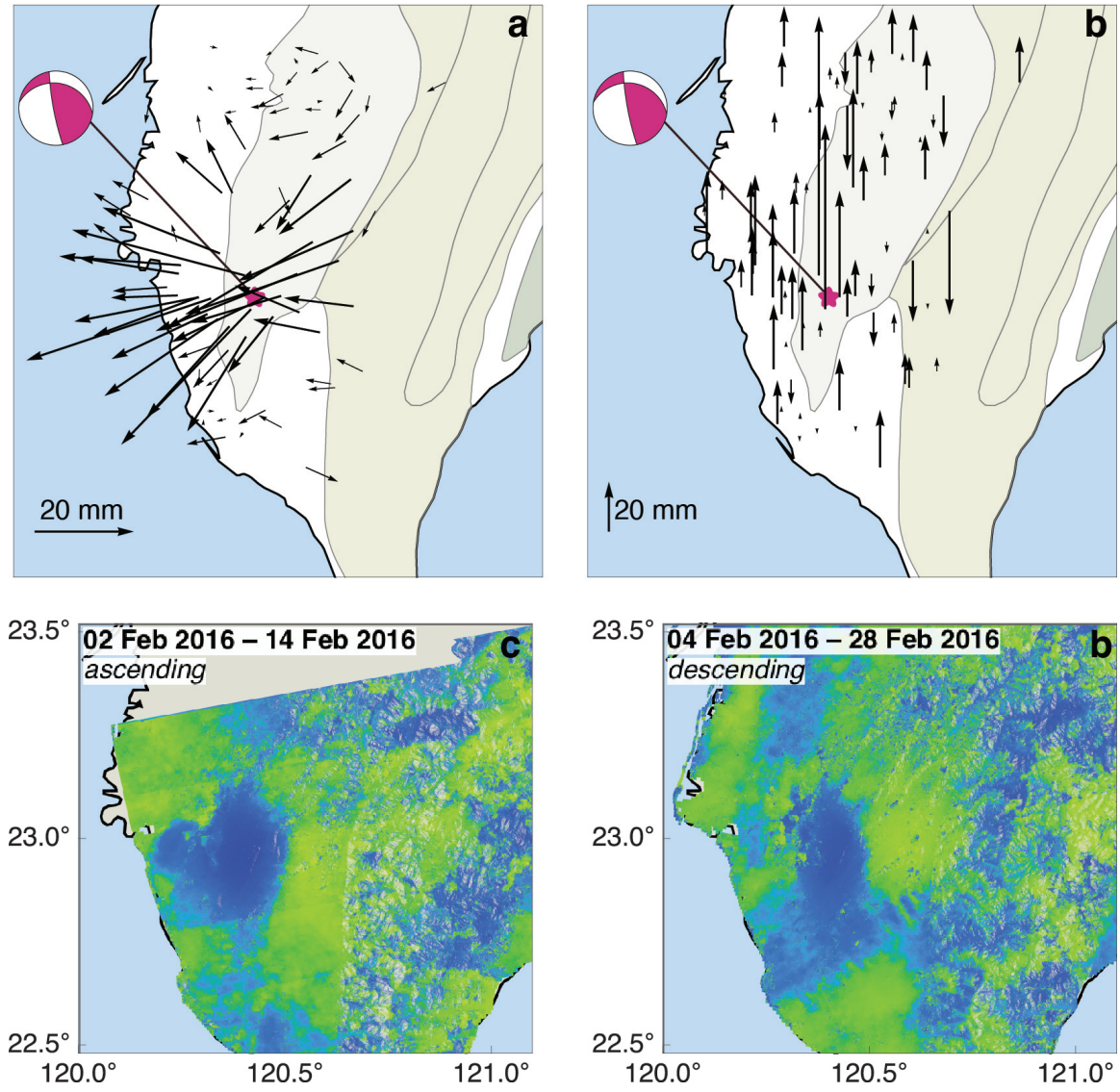


Figure 4.1: Geodetic data used in the MeiNong coseismic example: GNSS offsets from Haung *et al.*, 2016 (**a** and **b**) and interferograms from 3 (**c** and **d**). Red star in (**a**) and (**b**) is the GCMT centroid and GCMT focal mechanism is indicated. Figure after 3.

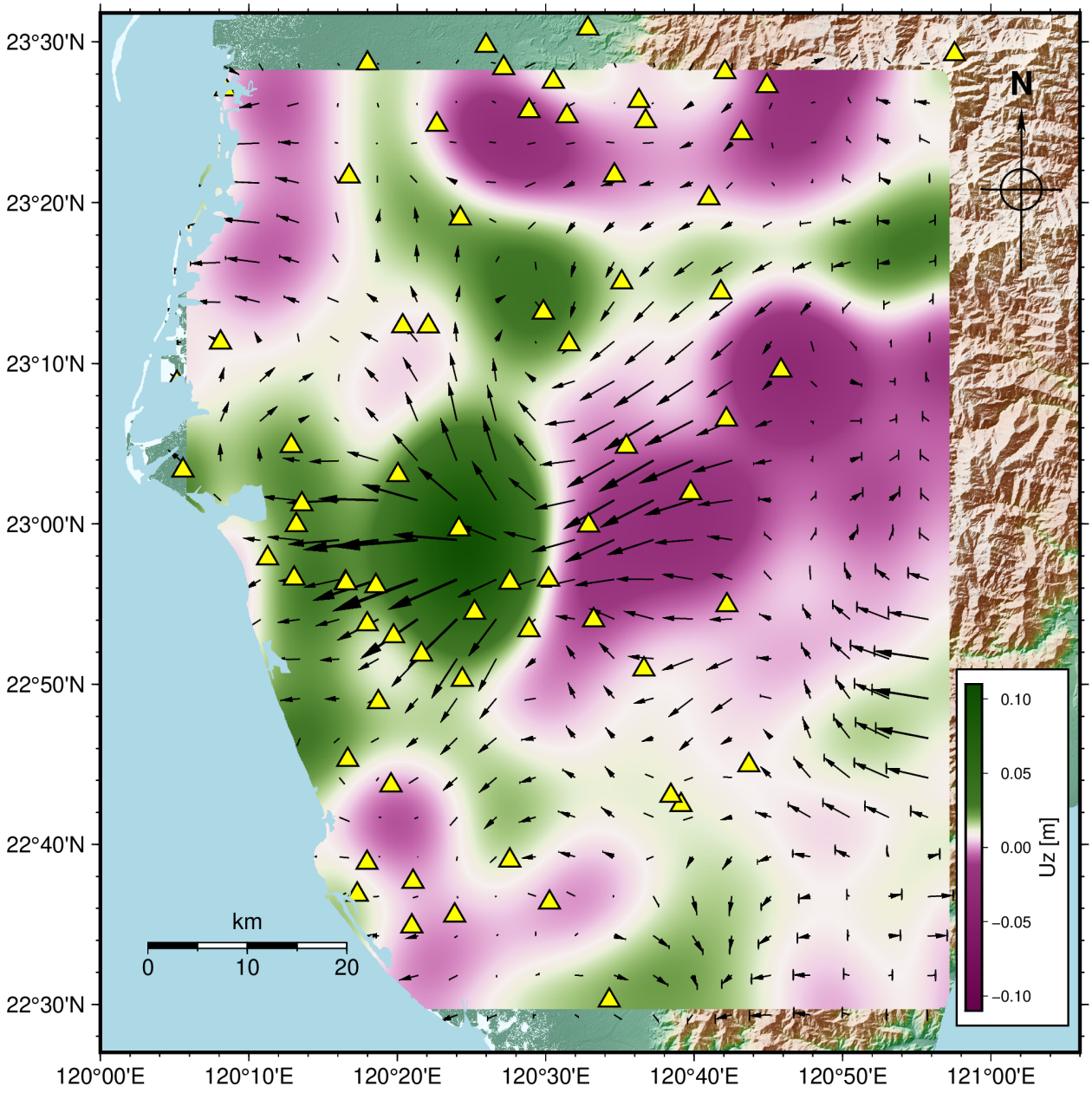


Figure 4.2: Fusion results for MeiNong 2016, earthquake. Colors show vertical deformation, the vector field is horizontal deformation, and the yellow triangles are the locations of GPS stations used in the fusion. The number of plotted horizontal samples from the posterior has been reduced to improve figure clarity.

The final fused deformation field captures the coseismic deformation of the MeiNong earthquake, but retains some degree of far-field spurious deformation, manifest mainly in the vertical component (Fig. 4.2). The most significant horizontal motion trends toward the west-southwest. Two large lobes of vertical deformation are present, corresponding to expected coseismic deformation. The westerly lobe is upward and the easterly one is down. There are several areas of deformation, primarily vertical, that are likely the result of spatially coherent noise contained in the Sentinel-1 interferograms. The regions of larger horizontal deformation along much of the eastern boundary and to the northwest are a consequence of poor constraint on the resolved field since those areas are located outside the network of GNSS stations used. The far-field spurious vertical deformation is largely influenced by the interferometric data (Figs. 4.1c and d), which is in general much more prone to spatially coherent noise sources (*e.g.*, Lohman and Simons, 2005; Edmardson, 2003). Using more interferograms could potentially reduce the influence of this non-earthquake related signal, there are eight Sentinel-1 interferograms that captured this event, including two used for testing purposes by 3 and another four that are not fully independent.

There is appreciable reduction in uncertainty between the resolved deformation field and GNSS observations. InSAR uncertainties are not shown because the spatial covariance of the observations makes any direct comparison difficult. The most significant reduction of uncertainty is for the verticals, with appreciable reduction in the eastings, and minor improvements in the northings (Fig. **??**). This can be explained by the sensitivity of InSAR observations to the different components, it being most sensitive in the vertical direction and with more sensitivity in range (easting) than azimuth (northing). The effect InSAR viewing geometry has on the reduction of uncertainties for the various components is explored analytically and discussed in C.1.

4.3.2 Coseismic deformation of the 2020 Sparta earthquake

We next consider the coseismic deformation of the 2020 M5.1 Sparta, NC earthquake, and the fusion of LiDAR and InSAR data. We note that this was only the second use of LiDAR to constrain a coseismic slip model, that we are aware of, and is of a much smaller magnitude earthquake than the first application of LiDAR to the M7.0 2016 Kumamoto, Japan (Scott *et al.*, 2018). We use three components of ground deformation derived from ICP differencing of repeated LiDAR surveys (data is from Szymanski *et al.*, (2024), and is fully described therein). We fuse the LiDAR data with two interferograms, one derived from radar scenes acquired by the ALOS-2 satellite (Japan Aerospace Exploration Agency) and one derived from scenes acquired by the Sentinel satellite (European Space Agency). The

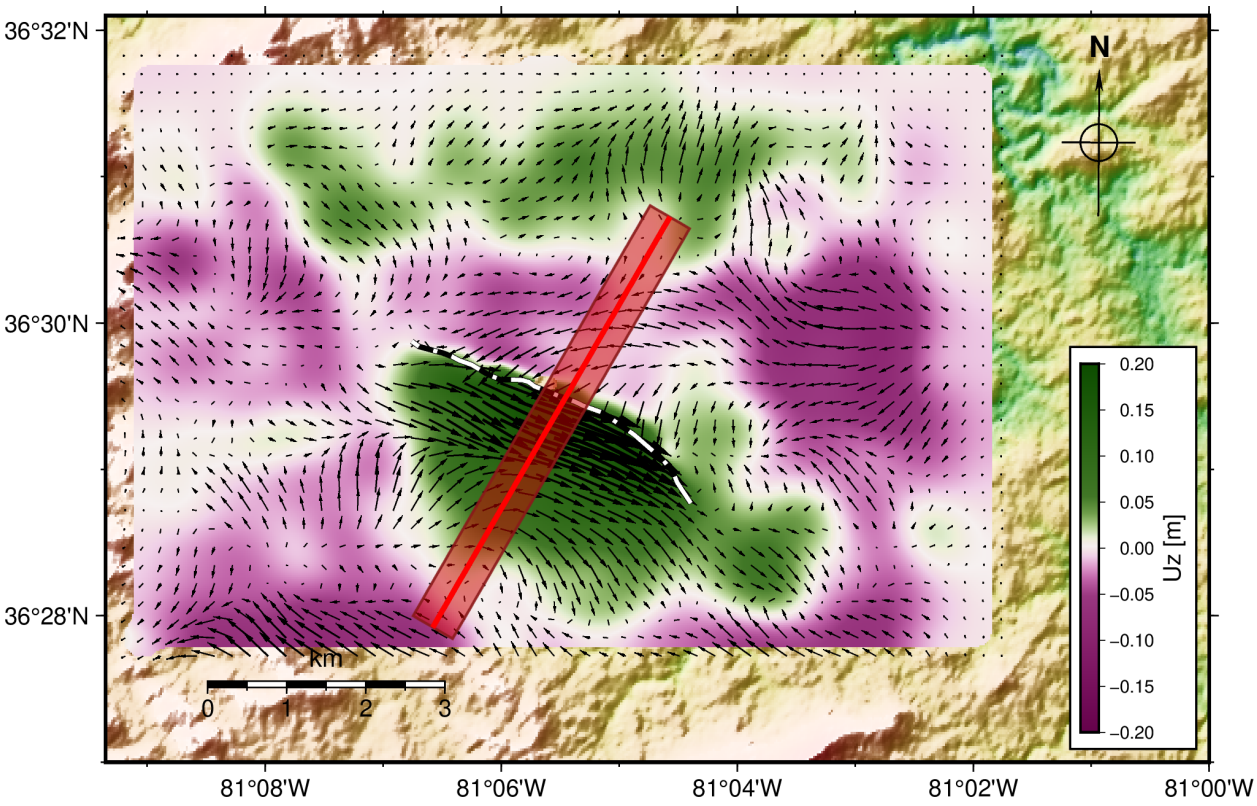


Figure 4.3: Fusion results for Sparta, 2020 earthquake. The red line is a transect across the surface rupture, the associated profiles are shown in fig #. The swath indicates the region of data to be projected onto the transect profiles.

former interferogram is from Wick and Chiu (2022) and the latter is from Szymanski *et al.* (2024), and the processing of each is fully described in those references. Szymanski *et al.* (2024) demonstrated that both of these interferograms were corrupted by errors resulting from the built environment, errors that were substantive enough to cause incorrect interpretation of the data and construction of a geophyiscally unreasonable coseismic slip model (see arguments in Szymanski *et al.* (2024) for further details). We do not remove the known spurious signals from the interferograms here, rather we use the full interferograms as a test Gentoo's ability to abate spurious signal through the assimilation of information from other more precise data sources.

We use 4841 and 3638 random samples of the ALOS-2 and Sentinel satellites, respectively (5% of the interferograms), and 4878 random samples of the LiDAR data (10% of the LiDAR data). As opposed to the MeiNong demonstration, the Sparta earthquake resulted in a surface break, which is clearly visible in both the interferograms and the LiDAR derived displacements (Wicks and Chiu, 2022; Szymanski *et al.*, 2024). To account for a latent deformation field with a spatial discontinuity in it, we use a the modified SE kernel described

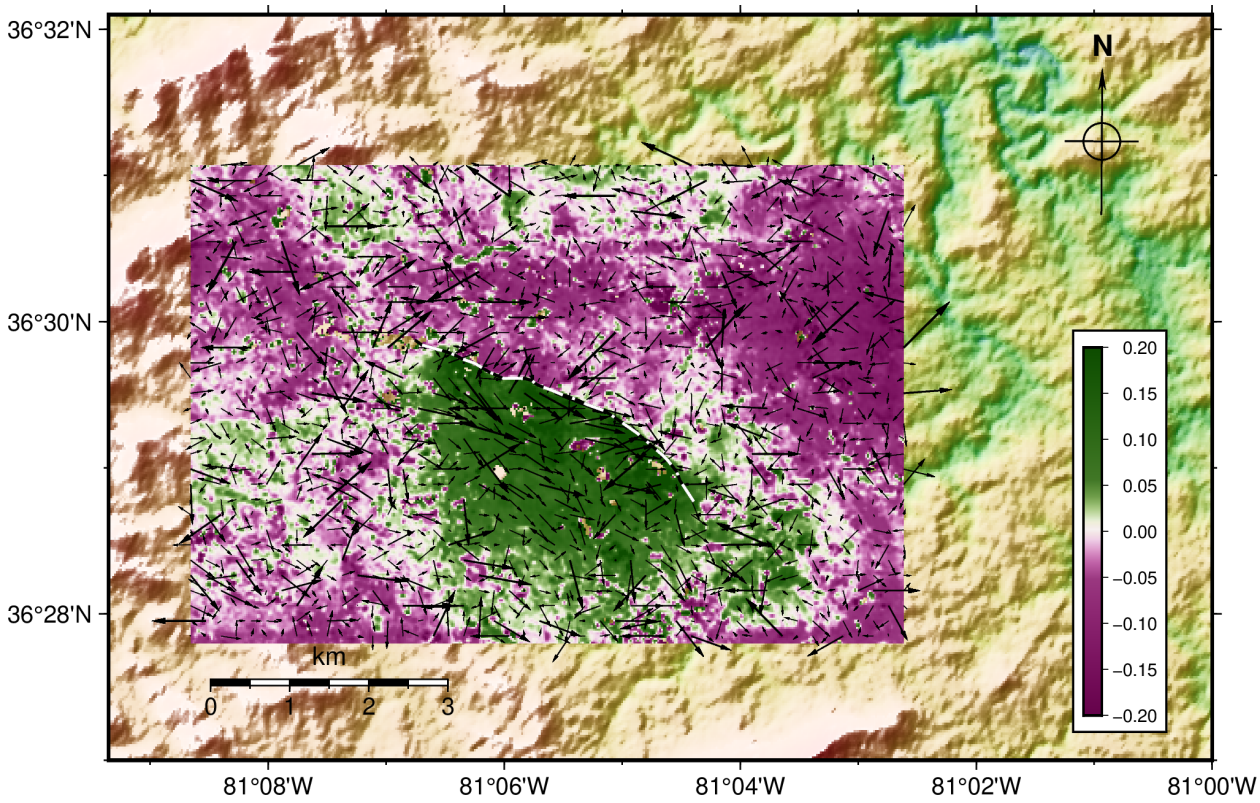


Figure 4.4: 3-D differential LiDAR observations for comparison to the fusion results for Sparta.

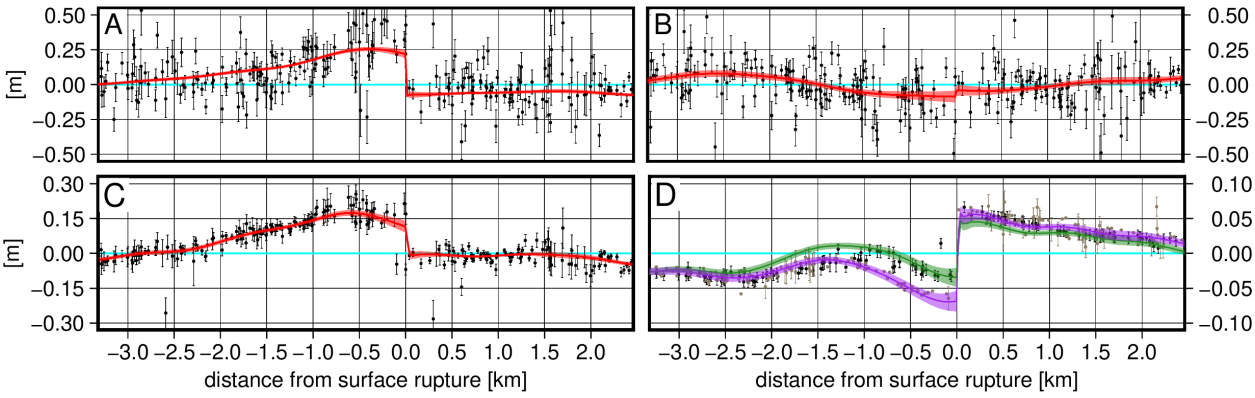


Figure 4.5: Fusion results with LiDAR and InSAR observations for transect shown in fig. #: profiles (A), (B), and (C) show 3-D differential LiDAR observations X, Y, and Z components, respectively, while (D) shows the S-1 and ALOS-2 observations. For profiles (A), (B), and (C) the scatter plots are the observation values with their associated uncertainties, the red line is the fusion result for each component, and the red shade is the 98% confidence interval for the fusion results. In profile (D) the black and brown scatter plots are the S-1 and ALOS-2 observations, respectively, and the purple and green lines are the S-1 and ALOS-2 fusion results as seen from the respective satellites.

in 4.2.2.2. We estimate the kernel hyper-parameters by minimized the negative log-marginal-likelihood with respect to the hyper-parameters, finding $\sigma_f^2 = 0.0012\text{m}^2$ and $l = 0.514$ km.

The resolved near-field deformation (Fig. 4.3) shows significant southeastward, fault-parallel motion on the southwest side of the surface rupture and moderate southwestward, fault-perpendicular motion on the northeast side of the surface rupture. Motion further from the fault to the southwest transitions to northeastward, fault-perpendicular motion. Vertical displacements are exclusively upward in the near-field to the southwest of the surface rupture with a more complex distribution of vertical motion to the northeast. On the northeast side of the surface rupture, motion is downwards at the northern terminal end of the rupture and transitions to upward motion at the southern terminal end. As in the MeiNong demonstration above, there is still spatially coherent signal farther from the fault, especially in the vertical component, that is not attributable to coseismic deformation; however, as noted above, InSAR is particularly prone to spatially coherent noise structures (*e.g.*, Tarayre and Massonnet, 1996; Massonnet and Feigl, 1998; Lohman and Simons, 2005), as is the differential LiDAR (*e.g.*, Glennie *et al.*, 2014; Lajoie *et al.*, 2019). Indeed, the prominent uplift north of the rupture, extending east-west, is dominated by the LiDAR derived vertical deformation field (Fig. 4.4).

The surface break in the Sparta earthquake is resolved using the discontinuous squared-exponential kernel. Figure 4.5 show transects of the fused field across the Sparta rupture,

along with the geodetic measurements. Panels (a)–(c) are the easting, northing, and vertical deformation compared to the LiDAR derived offsets, and panel (d) shows the fused results projected into the line-of-sight of either the Sentinel-1 or ALOS-2 satellites. The coseismic discontinuity is resolved clearly in the easting and northing componenets, with less offset in the northing component. This is consistent with the oblique thrust earthquake (the weighted average slip is 50°, but the near surface slip has a larger left-lateral component; Szymanski *et al.*, 2024).

There is appreciable reduction in uncertainty between the resolved deformation field and observations across all types. The most significant reduction of uncertainty is for the 3-D differential LiDAR horizontals, with moderate reduction in the Sentinel-1 LOS data, and a modest decrease for the 3-D differential LiDAR verticals and ALOS-2 LOS data (Fig. S4).

4.4 Discussion

4.4.1 Impact of Gentoo on signal clarity

As we have already touched on, an attractive characteristic of data fusion is the ability to leverage the strengths of the various input data types to offset weaknesses in others. This manifests as a reduction in the noise level of the resolved deformation field and the removal of spurious signal, if present. The latter effect requires that a majority of the input data types do not contain the spurious signal. The signal-to-noise ratio of the observations for the MeiNong earthquake is sufficiently high that it's fusion does not benefit as much from this particular effect. However, for the Sparta earthquake, we see both an impact on noise level and the errors caused by the built areas present near the surface rupture.

In particular, the horizontal components of the 3-D differential LiDAR have limited coherent signal in the horizontal components, which are largely composed of noise (2.2). When comparing the estimated field from 3-D differential LiDAR and our fusion, there is marked improvement in the coherence of the horizontal deformation. While both LiDAR and InSAR are most sensitive to vertical deformation, the InSAR provides sufficient constraints on the horizontal deformation to provide significant improvement in the noise level of the horizontal components of the resolved deformation field.

Both the Sentinel-1 and ALOS-2 interferograms for Sparta contain several areas of anomalous signal near the surface rupture that are especially prevalent in the ALOS-2 interferogram Szymanski *et al.* (2024). Wicks and Chiu (2022) argued this signal indicated subsidence to the southwest of the surface rupture in contradiction to other observations and this interpretation likely lead to the development of a questionable model for the causative fault

Szymanski *et al.* (2024). The resolved deformation field for Sparta, 2020 shows no evidence of subsidence to the southwest of the rupture, in fact we find uplift which is consistent with observations reported in Figueiredo (2022) and estimated models from Szymanski *et al.* (2024) and Pollitz (2023). This demonstrates our fusion methods ability to significantly reduce the presence of spurious signal, while improving the clarity and interpretability of the underlying deformation field.

4.4.2 Extensions and thoughts

We reiterate that Gentoo is not restricted to the geodetic types used in our demonstrations. Observations from other surveying techniques (*e.g.*, leveling data, borehole strain meters, structure-from-motion photogrammetry, offsets from optical images), can be assimilated in the fusion to estimate the underlying deformation field. That being said, the quality of results from Gentoo rely on how well data variances and covariances are accounted for. As mentioned in Section 4.3, there is an appreciable amount of spatially coherent signal in both the resolved fields for Sparta and MeiNong that is almost certainly the result of spatial coherent noise present in InSAR, as well as LiDAR for Sparta. Both instances would likely benefit from a more accurate accounting of the spatial covariances within the respective data types.

The combination of GNSS and InSAR observations with the inclusion of the time dimension is of particular interest since not only are the two modalities spatially complementary, they are temporally complementary as well. Continuous GNSS stations have a standard measurement frequency of approximately every 15 seconds, whereas SAR acquisitions are typically far less frequent. For example, Sentinel-1A/B has about a 21 day repeat-pass frequency. The complementary nature of their sensitivity to components of deformation, spatial distribution, and temporal frequency make their fusion extremely desirable. As Gaussian processes can readily be extended into the time dimension (*e.g.*, Hines and Hetland, 2017), and the fusion framework we have laid out can be extended to time varying deformation. However, the fact that interferograms represent the integrated deformation over the time between acquisitions, resulting that interferometric data is in a linear graph space (*e.g.*, Hetland *et al.*, 2012; Reinisch *et al.*, 2019), poses an interesting challenge.

4.4.3 Covariance models

Another potential avenue for improving fusion results would be to allow more flexibility in the covariance function used. For example, squared-exponential kernels can allow for anisotropy in the underlying field by using a different characteristic length scale for each

dimension. While a fusion could benefit from these added complexities they should be carefully considered for the same reasons as kernel selection. In the case of anisotropic SE kernel presented above, if the data is not oriented appropriately or the spatial extent of any potential anisotropy is limited, results may be degraded rather than improved. For example, take a strike-slip fault trending north-south. In this case it may be tempting to incorporate a longer characteristic length scale for the northings and a shorter one for the eastings. However, signal just beyond the terminal ends of the fault will likely be over(under)estimated and if there were any jogs or irregularities in the geometry of the fault trace similar issues would arise. Periodic kernels are also available which could be used to describe seasonal variations in a time-varying fusion. Kernels can also be combined through multiplication and addition allowing them to describe more complicated datasets that may be the result of multiple underlying processes (Williams and Rasmussen, 2006, Murphy, 2012).

While our modified SE kernel presented in 4.2.2.2 works well for data available for the Sparta earthquake, successfully capturing the surface rupture as intended, customizing kernels in this manner create degenerate functions that do not produce valid covariance matrices. As such, we tested the kernel with varying hyper-parameter values and it only remains positive semi-definite (a requirement for a valid, non-degenerate kernel) under certain conditions. Specifically, the characteristic length scale has a strong impact on whether the kernel produces valid covariance matrices. As the length scale increases ($l >$ 1.5 km for the Sparta data) the computed covariances matrices become non-PSD and produce a "ringing" in the resolved latent deformation fields. This is a documented issue (Duvenaud, 2014) for SE kernels when l is over-estimated that is likely exacerbated by the imposition of the discontinuity. However, within particular ranges, including the ones presented in this paper, the modified kernel remains valid and produces PSD covariance matrices.

4.4.4 scalability of the Gaussian process regression-based fusion

A downside of using Gaussian processes for regression is the computational cost of explicitly computing the posterior mean and covariance functions scaling as $\mathcal{O}(n^3)$ which can cause many problems to quickly become intractable as the number of observations increases. Coupling that with the use of Φ, which may contain coefficients that need to be learned, can increase the cost to a ceiling of $\mathcal{O}(n^3C^3)$. An example of a coefficient that may require learning would be one describing the connection between GRACE data and other observations for studying fluctuations in groundwater. Leh *et al.* (2005) propose the use of the *informative vector machine* (IVM) framework. The idea underpinning IVM is to construct a sparse approximation of the full posterior by using an "active" subset of the training subset.

This active subset is selected using information-theoretic criteria with the intent of retaining training samples that contain the most information about the underlying signal. We direct the interested reader to Leh *et al.* (2005) for the details of IVM implementation.

4.5 Conclusions

We introduce a Gaussian process regression based geodetic fusion methodology applicable to a wide range of geodetic observations. We demonstrate our fusion method for coseismic observations of the 2016 MeiNong, Taiwan and 2020 Sparta, NC, USA earthquakes. Using a formalism of a semi-latent factor model, our method makes use of multi-output Gaussian process regression to provide a framework in which to fuse multiple types of geodetic data, resulting in a single, multi-component deformation field at every point in the domain, complete with quantified uncertainties. Rather than using one modality of geodetic observations to correct another, or relying on an underlying physical model in which to combine data from multiple geodetic techniques, our method allows the data themselves to inform the resulting fused deformation field. The fusion method we introduce uses the strengths of one geodetic data set to bolster the weaknesses of another data type, through the transfer of information withing a statistically robust framework. The power of our methodology not only rests in it's ability to ingest a wide range of observational modalities and produce a single, three component deformation field, but also in it's ability to characterize robust uncertainties on that field. Our fusion methodology can be adapted to incorporate time-varying observations, generating a deformation field that spans both time and space that is defined across the entire domain. This approach offers unparalleled insights into transient geophysical phenomena.

CHAPTER 5

Conclusions

This dissertation underscores the challenges encountered with noisy and incomplete data, emphasizes the importance of recognizing these issues, and presents two strategies for addressing them. Each approach tackles the issues presented by problematic data from a different angle. Our application of GGFL and integration of distributed estimation into the search for fault geometry in Chapters 2 and 3 seek to enhance the robustness of coseismic slip models against data errors. Conversely, Gentoo (Chapter 4) aims to improve data quality directly through the data itself. The following sections provide a more detailed discussion of the effectiveness of each approach.

5.1 Evaluation of Contributions

5.1.1 Estimation Method for Coseismic Slip Modeling

In chapter 2, we invert the line-of-sight (LOS) displacements from two interferograms — the ALOS-2 interferogram from Wicks and Chiu (2022) and a Sentinel-1 interferogram — along with differential LiDAR data to analyze the coseismic slip of the Mw 5.1 Sparta, North Carolina, earthquake in 2020. This chapter emphasizes the robustness of our proposed estimation methods in handling poor-quality observations, particularly the low signal-to-noise ratio (SNR) in the InSAR and LiDAR data. For determining both the fault dip and the coseismic slip distribution, we use a Monte Carlo search to test various dip angles, inverting for the slip distribution via GGFL for each tested dip. Our analysis reveals that the slip from the Sparta earthquake was shallow and predominantly oblique, occurring on a fault trending northwest-southeast with a 50° southwest dip. This single-fault coseismic slip model contrasts with the two-fault plane model proposed by Wicks and Chiu (2022), which included one fault plane slipping aseismically with normal motion and another slipping seismically with reverse motion. We suggest that the two-fault plane solution resulted from anomalies in the interferograms due to mismatched resolutions between the DEM and InSAR

during processing and the influence of nearby built structures. Furthermore, our preferred coseismic slip model aligns with expectations based on the WSM (Heidbach et al., 2016, 2018). In that, if we assume that the MCS is coincident with Sh_{max} predicted by the WSM and the direction of fault slip is in the direction of maximum fault shear stress, the Sparta earthquake aligns with stress tensors that are characteristic of an Andersonian thrust regime.

Chapter 3 reevaluates the coseismic deformation recorded during the 2010 Jiashian and 2016 MeiNong earthquakes in southwestern Taiwan. In this chapter we develop coseismic slip models for both events using the same estimation methodology as Sparta. In contrast to Sparta, the advantages provided by our integrated search were better showcased here since we needed to estimate the full range of fault geometry parameters. In order to more fully explore the sample space, we assumed non-informative priors on all fault geometry parameters as well. Our Jiashian coseismic model is in general agreement with seismologically derived focal mechanisms and with the coseismic model proposed by Hsu *et al.* (2011). However, our analysis suggests a more northerly striking and shallower slip surface than those resolved in the focal mechanisms or previous models, which assumed a deep fault geometry. We show that these assumptions likely introduced biases into the final coseismic slip models. Moreover, constraining fault geometry parameters with an assumption of uniform slip can also lead to biases. Our final MeiNong model does not show systematic vertical residuals, indicating that aseismic processes such as triggered creep or off-fault volumetric deformation are not needed to explain the observed vertical coseismic offsets. The similarity in fault strikes and the proximity of inferred slip regions in our models suggest that both earthquakes occurred on a single fault structure, which dips eastward and steepens with depth.

Overall, both applications proved to be successful and provided coseismic slip models with greater explanatory power than other published models for the same events. This is particularly true for the Sparta earthquake, whereas the MeiNong earthquake still necessitates more geologic context but potentially simplifies the structure underlying southern Taiwan by placing two previously independent earthquakes on a single thrust fault. We argue that the success of our new estimation methodology lies in it's resiliency to data errors, inclusion of physical qualities of the earthquake under consideration, a reduction in superfluous model parameters, and more nuanced evaluation of candidate models through the use of GGFL within our integrated approach. While there is no precise threshold regarding earthquake magnitude, sample size, signal-to-noise ratio, etc., not all scenarios will necessitate using our proposed method to achieve satisfactory results. If data with minimal uncertainty is available and ample spatial coverage (*i.e.*, with data capturing all of the expected coseismic deformation from the earthquake), the additional computational effort may not be justified. However, even with ideal data conditions, our method will deliver results that are at least

comparable, if not superior, to those obtained from a conventional inversion.

5.1.2 Geodetic Data Fusion

In chapter 4 we present Gentoo, a novel geodetic fusion method using SLFM as it's foundation. The SLFM framework utilizes multi-output Gaussian process regression to merge diverse geodetic data types into a unified deformation field, complete with well-defined uncertainties for every point in the domain. Unlike traditional methods that rely on correcting one observation type with another or using an underlying physical model to combine different data sources, our approach leverages the data itself to construct and enhance the accuracy of the resolved deformation field. This enhanced accuracy is facilitated by the transfer of information within a statistically robust framework that exploits the strengths of one geodetic data set to address the weaknesses of another. In many ways the linear mixing matrix is the scaffolding of this framework, as it encodes the correlation structure of the underlying deformation and accounts for dependencies between different data types providing a critical advantage over other geodetic integration methods that treat data types as independent.

As a demonstration, we apply Gentoo to coseismic observations of coseismic surface deformation from the 2016 MeiNong, Taiwan and 2020 Sparta, NC, USA earthquakes. Each earthquake provided an opportunity to highlight different aspects of Gentoo. The application on the MeiNong event fused GNSS and InSAR data with a moderate signal-to-noise ratio, and emphasized Gentoo's ability to capitalize on the complementary nature of component-wise sensitivity and spatial coverage of the two modalities. We effectively mapped the coseismic deformation field, accurately capturing the near-field signal. However, there is some spurious signal, mainly in the vertical measurements of the far-field, likely due to spatially correlated noise in the InSAR data. Potential avenues for improving the accuracy of the far-field are explored in 5.2. Our application to the Sparta event fused 3-D differential LiDAR and InSAR from two different platforms. In this case, the signal-to-noise ratio was notably lower overall, and both interferograms — one from Sentinel-1 and the other from ALOS-2 — exhibited extensive regions of spurious signal. These challenges provided an opportunity to showcase the de-noising capabilities of Gentoo. Compounding the challenge, the coseismic slip from the Sparta earthquake reached the surface, resulting in a rupture trace that appeared as a step or discontinuity in both the InSAR line-of-sight measurements and the three-component field estimated by differential LiDAR. To address the surface rupture, we developed a specialized covariance function that effectively captured the discontinuity, preserving it in the resolved deformation field for Sparta. Again, the coseismic deformation field was effectively mapped, showing marked improvement when compared to the three component deformation

field estimated by LiDAR alone and reducing the large regions of anomalous signal present in the Sentinel-1 and ALOS-2 interferograms. As with the resolved deformation field from MeiNong, there is some suspect signal in the far-field related to spatially correlated noise from both InSAR and LiDAR in this case.

5.2 Future Work

Future research directions for the integrated estimation methodology include developing a more computationally efficient workflow, exploring its utility for larger earthquakes, and application to other deformation sources. Improvements in computational efficiency could potentially allow for the integration of all candidate fault geometries, as opposed to the two-step procedure used for MeiNong in which we reduced the prior using a uniform search before integration. The more interesting extensions are the later two. It would be interesting to see if the benefits provided by GGFL scale to larger magnitude events where the signal-to-noise ratio is typically much higher, or if the added computational burden is not worth it and a more traditional method would suffice. I would also like to test our estimation schemes effectiveness for estimating models for other sources, such as magma chambers.

The most exciting future direction for Gentoo is the inclusion of the time dimension to estimate and map transient geophysical signals. By incorporating time-varying signals, we can leverage both the spatial and temporal complementary aspects of geodetic observations, such as GNSS and InSAR. Providing a more detailed picture of ground motion through time has strong potential for advancing our ability to monitor and mitigate hazards related to earthquakes, landslides, and other tectonic processes. The inclusion of other, more exotic data types such as gravity recovery and climate experiment (GRACE) data as input stands to provide significant improvements in detecting seasonal variations in groundwater and monitor it's usage. Other key industrial applications include monitoring movements related to oil extraction, subsidence from tunneling and mining, and natural gas extraction. While significant societal benefits could be achieved, addressing this challenge also has scientific value. Many fields within Earth and environmental sciences use geodetic data to refine their models. Disciplines such as seismology, geomorphology, and geohydrology stand to gain from enhancements in the quality of data products derived from geodetic observations.

APPENDIX A

Supplementary Material for Chapter 2

A.1 Additional InSAR figures and coseismic slip models

Figure A.1 shows a Google Earth image of the area of the Sparta earthquake (Google, 2020), highlighting several industrial parks which we argue led to anomalies in the InSAR interferograms. Figure A.2 depicts the samples of the interferograms that were inverted. Figure A.3 shows misfit as a function of fault dip. Figures A.4, A.5, A.6, and A.7 are the coseismic slip models, along with the simulated and residuals interferograms and LiDAR components, for models CSM-FULL, CSM-S1, CSM-LiDAR, and CSM-JOINT respectively.

A.2 Estimating coseismic offset at GNSS site NCSR

The GNSS time series for NCSR is available from the Nevada Geodetic Laboratory (Blewitt *et al.*, 2018) (24 hour final solution in NAM reference frame). We estimate the coseismic offsets from the east and north components by fitting the following function, after Dong *et al.* (2002), to the times series of each component

$$\begin{aligned} u_j(t) =& m_0^j + m_1^j t + m_2^j t^2 + \\ & m_3^j sin(2\pi t/y) + m_4^j cos(2\pi t/y) + m_5^j sin(4\pi t/y) + m_6^j cos(4\pi t/y) + \\ & m_7^j H(t - t_{\text{sparta}}) + m_8^j H(t - t_1), \end{aligned} \tag{A.1}$$

where j is either the east or north positions. Time, t, is modified Julian date, y is either 365 or 366 days depending on whether t is in a leap year or not, t_{sparta} is the day of the Sparta earthquake, and t_1 is motivated by a prominent offset in the east component time series (Fig. A.8A).

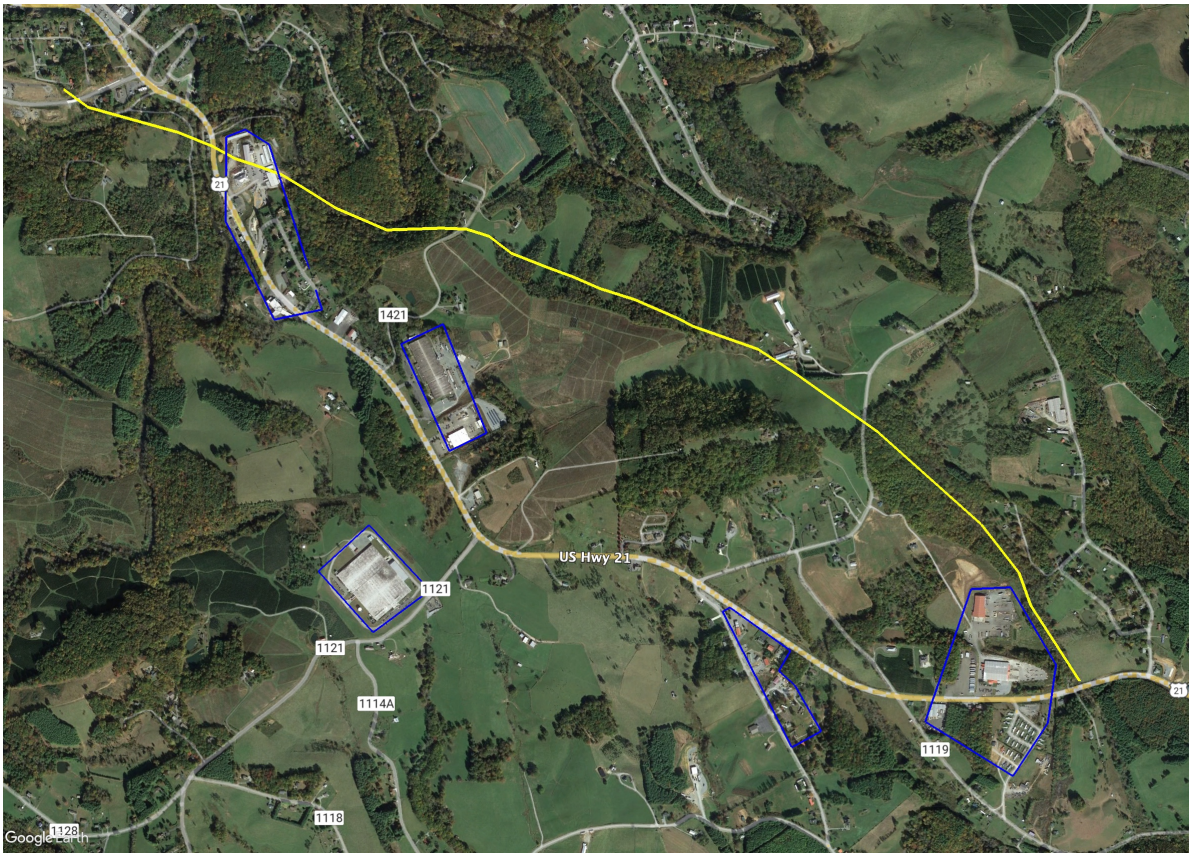


Figure A.1: Google Earth view of the region around the Sparta earthquake (Google, ©2020 CNES / Astrium, Maxar Technologies), with the mapped surface rupture (yellow line) and outlines of prominent industrial parks (blue polygons).

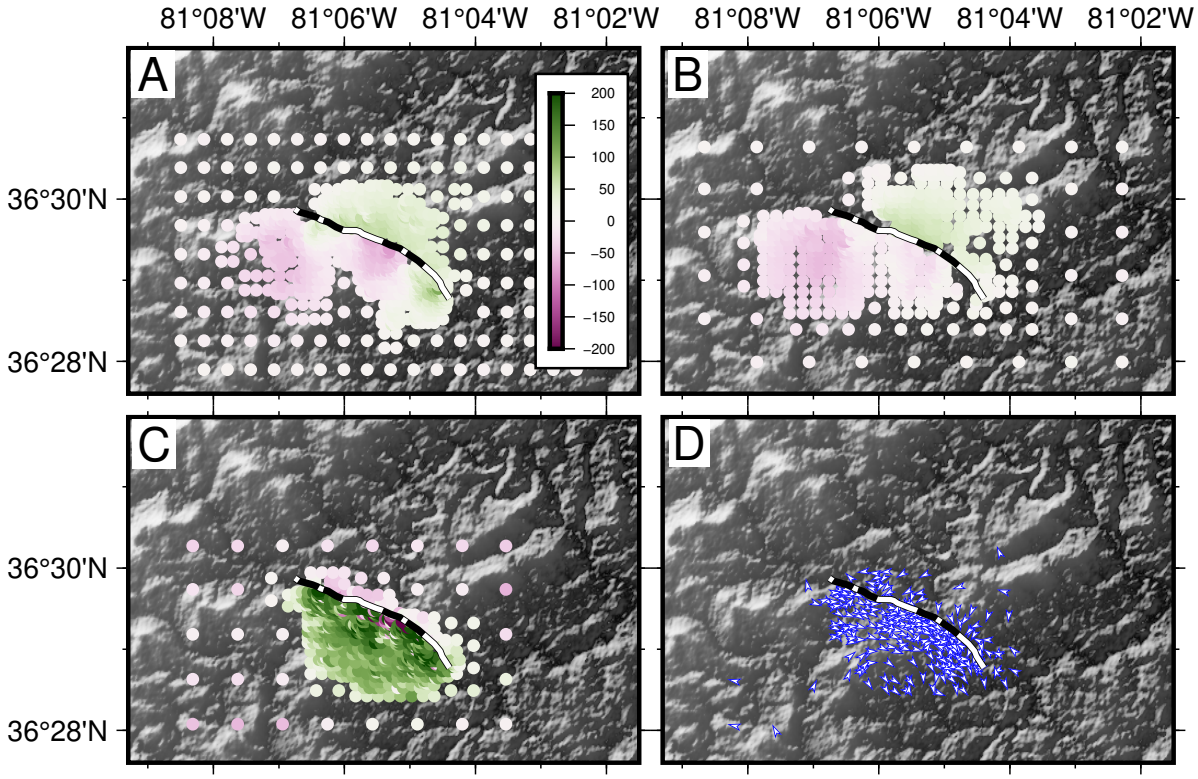


Figure A.2: Samples of the ALOS-2 (A) and S-1 (B) interferograms, and LiDAR verticals (C) and horizontals (D) selected for inversion, with cross indicating the hypocenter, and dashed line indicating the field mapped surface rupture (Figueiredo et al., 2022).

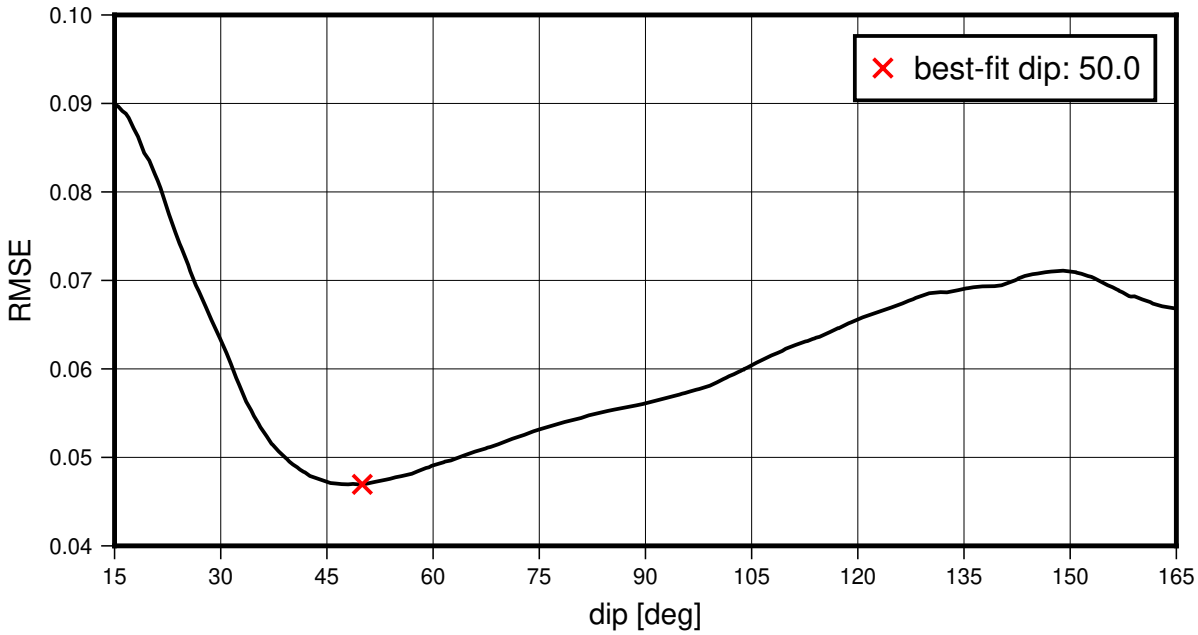


Figure A.3: Total mistfit to the ALOS-2 and S-1 interferograms, and LiDAR, with the data corresponding to the industrial parks masked, as a function of the fault dip. Dips $> 90°$ are northeast dipping faults.

We limit the data inverted to four years prior to the earthquake and up to 02 Feb 2024. The data over this duration shows no clear curvature, and thus the quadratic term is not needed. Nevertheless, we include it for completeness (both components resolve m_2 on the order of 10^{-10} mm/day^2). For simplicity, we estimate the model parameters using a unweighted least squares, without including the data covariance matrix. The coseismic offsets, represented by the terms m_7, are not used to constrain the coseismic slip model, and as discussed in the main text the data from NCSR is questionable due to the fact that the station is located on a building that was damaged in the earthquake. The fits to the GNSS time series are shown in Fig. A.8, and the Sparta coseismic offsets are $m_7^e = 7.8$ mm and $m_7^n = 11.1$ mm.

A.3 Stress drop

We calculate average static stress drop, $\overline{\Delta\sigma}$, for all coseismic slip models using the relation

$$\overline{\Delta\sigma} = C\frac{M_0}{A^{3/2}}$$

where C is a geometric constant and A is the area of the rupture domain (*e.g.*, Scholz, 2019; Brune, 1970; Noda *et al.*, 2013). Here A is determined by first identifying the set of

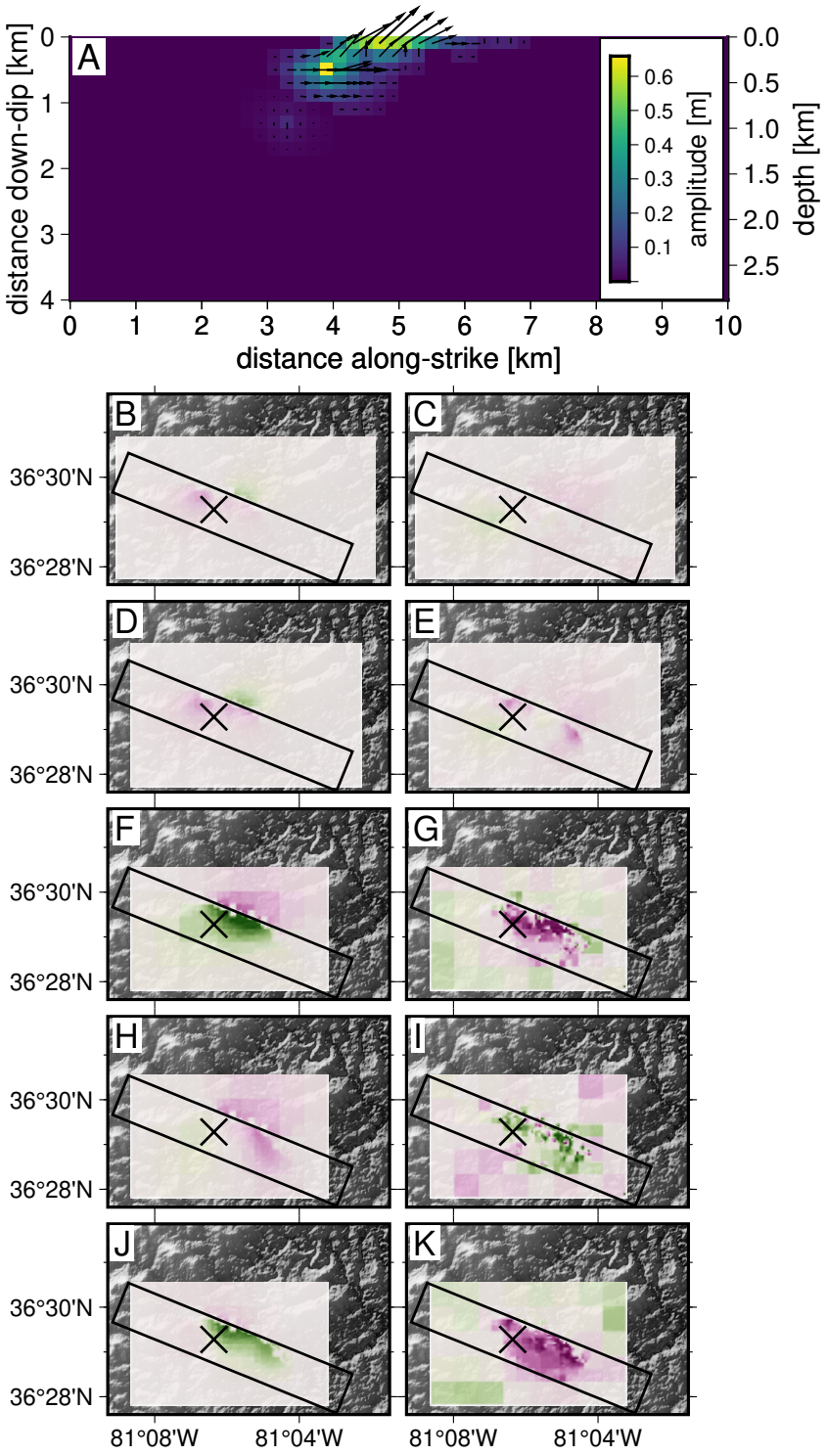


Figure A.4: (A) Slip distribution in CSM-S1, with black arrows indicating the slip vector on each subfault, and colors indicating the magnitude of slip. Synthetics and residuals from CSM-FULL for S-1 (B & C), ALOS-2 (D & E), and LiDAR components X, Y, and Z (F)-(K), respectively. Colors in panels (C)-(K) follow colorbar in panel (B). Cross indicates the hypocenter, blue polygons outline prominent industrial parks, and black rectangle is the surface projection of the fault.

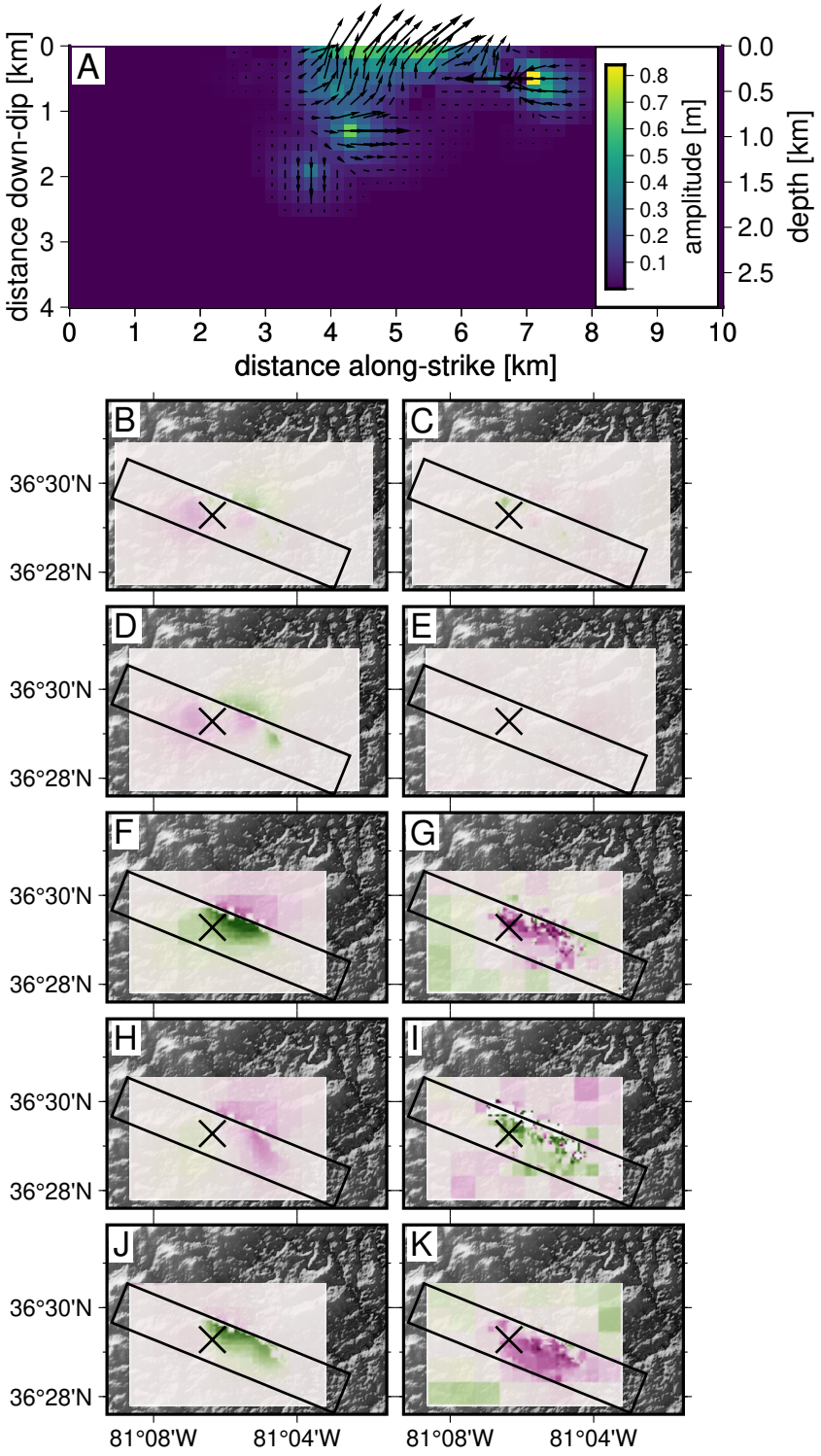


Figure A.5: (A) Slip distribution in CSM-FULL, with synthetics and residuals from CSM-S1 for S-1 (B & C), ALOS-2 (D & E), and LiDAR components X, Y, and Z (F)-(K), respectively. Colors in panels (C)-(K) follow colorbar in panel (B), all other symbols are as in Fig. S4.

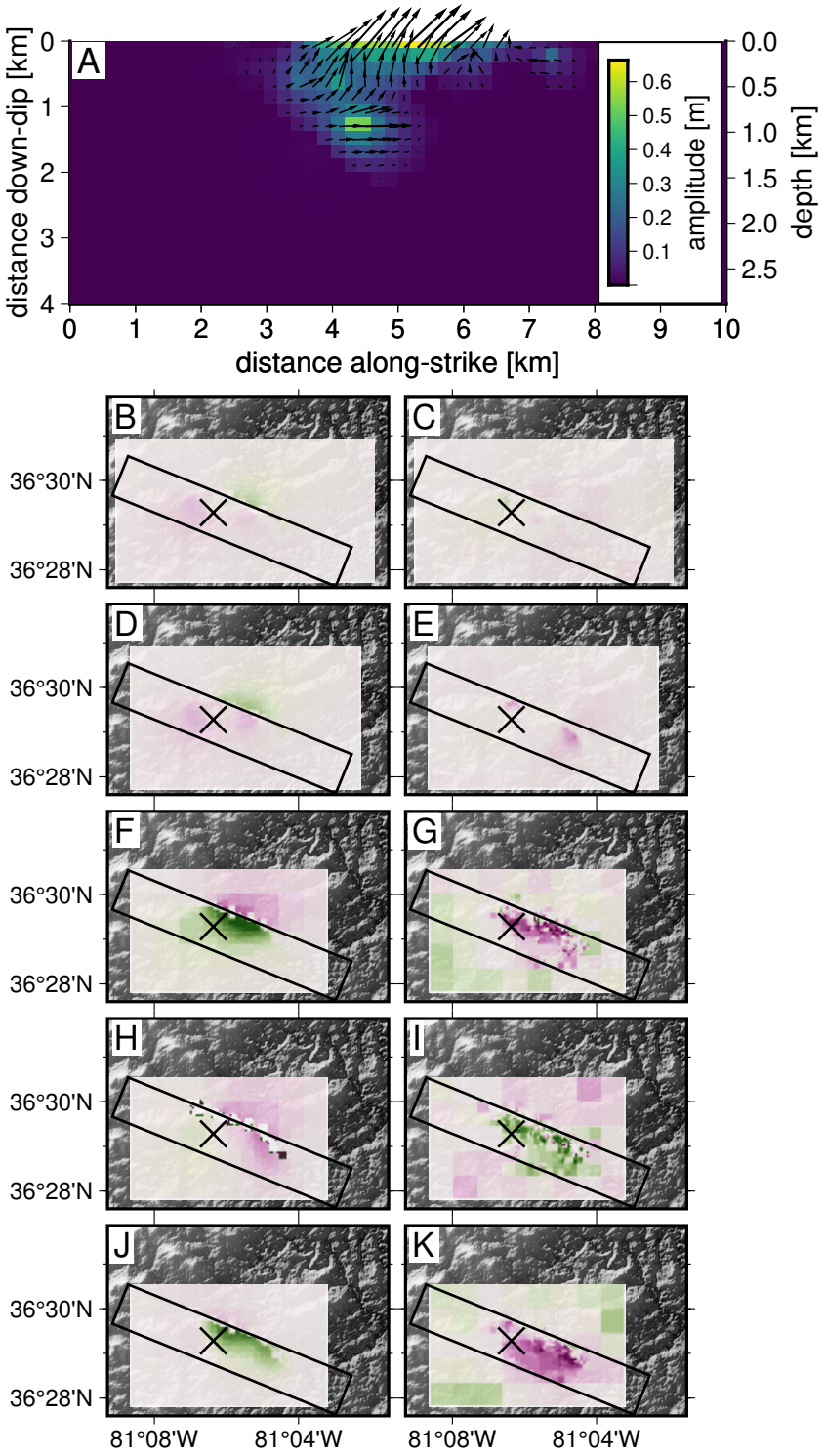


Figure A.6: (A) Slip distribution in CSM-DAR, with synthetics and residuals from CSM-DAR for S-1 (B & C), ALOS-2 (D & E), and LiDAR components X, Y, and Z (F)-(K), respectively. Colors in panels (C)-(K) follow colorbar in panel (B), all other symbols are as in Fig. S4.

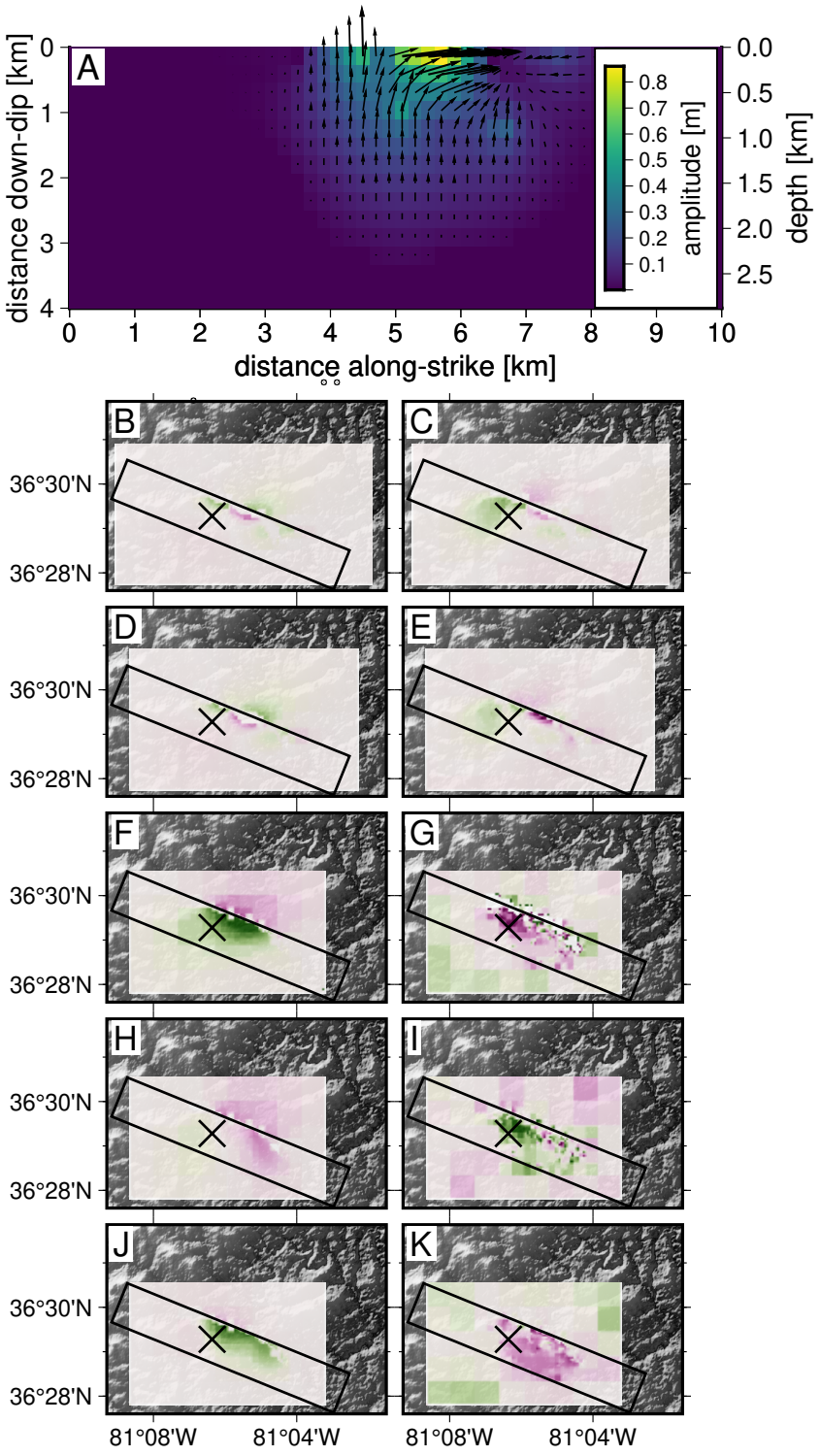


Figure A.7: (A) Slip distribution determined from the LiDAR ICP differencing, with black arrows indicating the slip vector on each subfault, and colors indicating the magnitude of slip. Synthetics and residuals from CSM-LiDAR for S-1 (B & C), ALOS-2 (D & E), and LiDAR components X, Y, and Z (F)-(K), respectively. Colors in panels (C)-(K) follow colorbar in panel (B), all other symbols are as in Fig. S4.

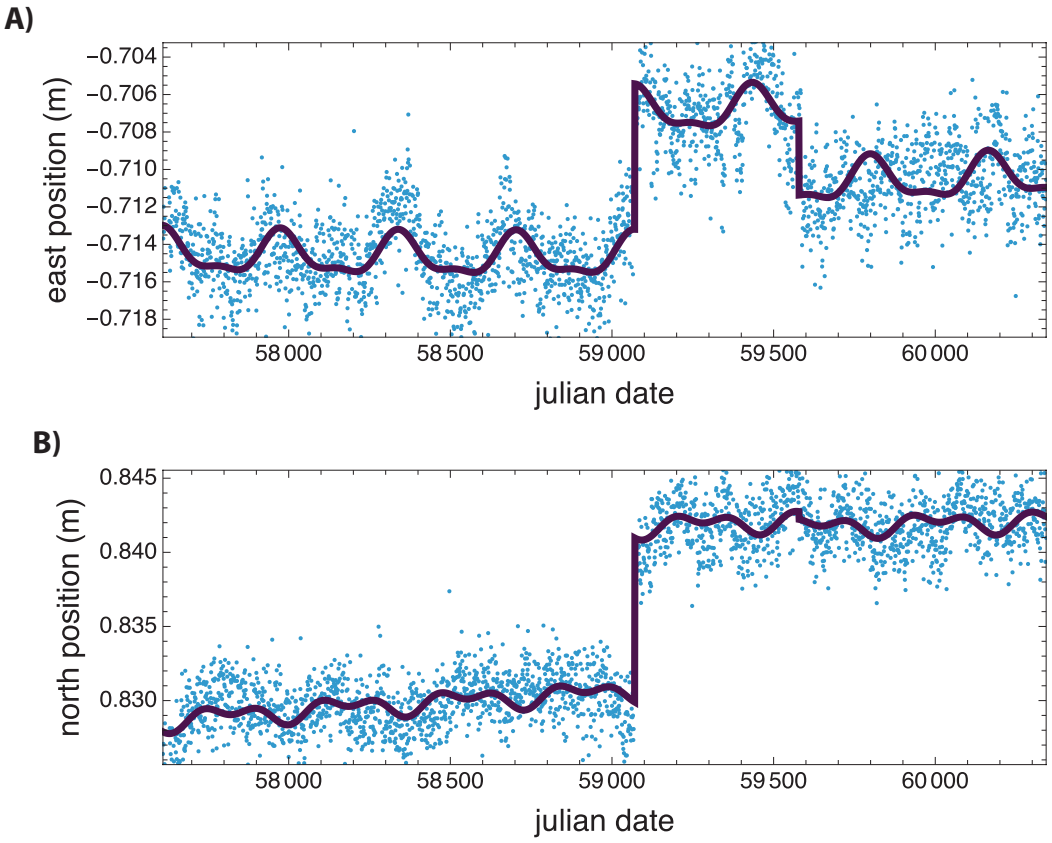


Figure A.8: GNSS time series from station NCSR, from the Nevada Geodetic Laboratory (Blewitt *et al.*, 2018), with the best fit model used to estimate the Sparta coseismic offsets (panels A and B are the east and north components, respectively).

patches, $\mathcal{P}$, containing slip exceeding a given fraction, a, of the maximum estimated slip,

$$\mathcal{P} = \{p \,|\, |\mathbf{\Delta u}(p)| \;\geq\; a \cdot max(|\mathbf{\Delta u}|)\}$$

(*e.g.*, Noda *et al.*, 2013). Then A can be found by taking the product of the size of $\mathcal{P}$ and patch size,

$$A = |\mathcal{P}| dx\, dy$$

where dx and dy are the patch dimensions. Here we treat the rupture as a rectangular crack with a roughly equal aspect ratio resulting in a value of 2.53 for C and we retain patches with slip greater than or equal to 10% of maximum slip. The estimated average static stress drop for CSM-M is 8.1 MPa; average static stress drops for all models range from 7.3 - 12.4 MPa and can be found on table 2.1. Our estimations align with stress drop estimates for eastern tectonic earthquakes having a 20 - 50% fractional stress drop (Huang *et al.*, 2017).

A.4 Comparison of CSM-JOINT to World Stress Map

The trend of $\mathrm{Sh_{max}}$ from the World Stress Map (WSM; Heidbach *et al.*, 2016, 2018) at 36.4°N and 81.0°W, roughly 11 km from the USGS determined epicenter, is 111° (taken from the 250 km search radius model, constrained with 15 stress indicators). $\mathrm{Sh_{max}}$ is the direction of the most compressive stress that is within a horizontal plane, assuming that one of the components of the principal stresses is vertically oriented, yielding an Andersonian-like stress regime. Assuming that $\mathrm{Sh_{max}}$ indicates the orientation of the most compressive principal stress, MCS (*i.e.*, that MCS is not dipping), and that the magnitudes of the intermediate and least compressive stresses, ICS and LCS, respectively, are equal, then the predicted direction of maximum shear stress resolved on the fault plane of CSM-JOINT, λ_τ, is 53.7° (Fig. S5b in the main text) – this angle does not depend on the absolute magnitude of the MCS (McKenzie, 1969) or on the relative magnitude of MCS to LCS (*e.g.*, Walbert and Hetland, 2022). Assuming that if that when the fault coseismically slipped, it did so, on average, in the direction of the maximum fault shear stress (the so-called Wallace-Bott assumption; Bott, 1959), this direction compares favorably to, the average rake of 48° in CSM-JOINT.

Parameterizing the relative magnitude of ICS to those of MCS and LCS as

$$\delta = \frac{\sigma_\mathrm{I} - \sigma_\mathrm{L}}{\sigma_\mathrm{M} + \sigma_\mathrm{L}}, \tag{A.2}$$

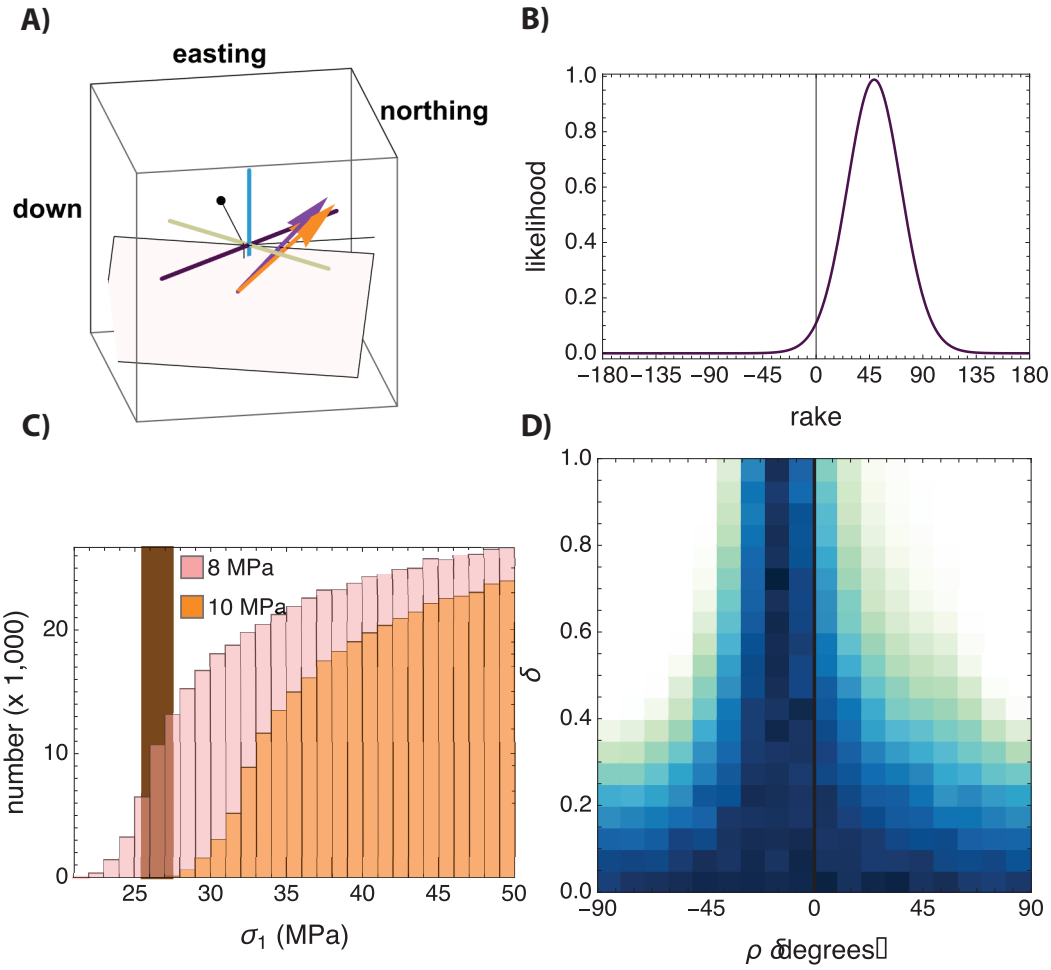


Figure A.9: (A) von Mises PDF used as the likelihood function in the stress estimation. (B) Marginal posterior PDF of σ_{M}, assuming that $\tau_{\max}$ is greater than 8 MPa (pink) or 10 MPa (orange). Brown field indicates a range of lithostatic stress at 1 km, corresponding to densities from 2600–2800 kg/m^3. (C) Posterior PDF of ρ and δ assuming $\tau_{\max} \geq 6$ or 10 MPa.

where σ_X is the magnitude of the X principal stress, we find that for $\delta = 0$ (*i.e.*, the magnitudes of ICS and LCS are equal), $\lambda_\tau = 52.6°$. At the other extreme, when $\delta = 1$ (*i.e.*, the magnitudes of MCS and ICS are equal, assuming vertical LCS), $\lambda_\tau = 74.9°$, with λ_τ varying linear between these extremes of δ. Exploring the background stresses that are compatible with CSM-JOINT in more detail, we follow the analysis of Walbert and Hetland (2022), but modified so that MCS is always oriented along Sh_{max} from the WSM. We additionally constrain the analysis so that only background stresses accepted in the posterior solution are those with a maximum fault shear stress, τ_{max} at least as large as large as 8 MPa, approximately the stress drop for CSM-JOINT. The analysis of Walbert and Hetland (2022) is Bayesian, and an uncertainty on the fault rake needs to be posited, which we take to be given by a von Mises probability density function, PDF, with a concentration parameter of 9.9 (Fig. A.9a), for which the range from pure reverse to pure strike-slip rake defines a 98% confidence interval. The analysis results in samples of a posterior PDF describing stresses parameterized by the maximum MCS, σ_M, an angle describing how far off vertical LCS is, ρ, and δ.

By adding the constraint that stress models are only considered likely if they produce $\tau_{max} \geq 8$ MPa, we are able to get a lower bound on σ_M (Fig. A.9b). σ_M represents the total stress prior to the earthquake. At 1 km depth, the approximate hypocentral depth of the Saint Luis University focal mechanism, for densities from 2600–2800 kg/m^3, the lithostatic stress in 25.5–27.5 MPa (Fig. A.9b). Stress models with σ_M below lithostatic correspond to horizontal non-lithostatic tension, and do not make sense. However, if the constraint on τ_{max} is raised to 10 MPa, then the histogram of σ_M is shifted about 10 MPa larger (Fig. A.9b). The posterior indicates that when $\rho \approx 15°$ (*i.e.*, with LCS 15° off of vertical), δ is unconstrained (Fig. A.9c). Alternatively for $\delta \lessapprox 0.25$, then ρ is relatively unconstrained (Fig. A.9c). In stress tensors with low δ, the magnitudes of ICS and LCS are close to eachother, and hence stress tensors that describe an Andersonian strike-slip stress regime (*i.e.*, $\rho = \pm 90°$) are only slightly different from an Andersonian thrust regime.

APPENDIX B

Supplementary Material for Chapter 3

B.1 Additional Figures

Here we present several auxiliary figures that give additional insight into our discussion in the main text. In Figure S1, we show histograms of the magnitudes of horizontal and vertical GNSS offsets for the 2010 Jiashian and 2016 MeiNong earthquakes. While the vertical offsets in the MeiNong earthquake were larger than those in the Jiashian earthquake, the ratio between vertical and horizontal offsets in both earthquakes follow simmilar distributions (*c.f.*, Figs. B.1c and f).

Figures B.2–B.4 are additional information regarding the estimation for the the coseismic models of the two earthquakes. Figure B.2 show histograms of the estimated fault area, slip magnitude, and associated moment magnitude, from the best fitting 20,000 models found in the initial search asssuming uniform fault slip. Figure B.3 show the distribution of centroid depth for all of the 10,000 models resulting in the secondary integrated search. Centroid depth is calculated as the weighted average depth of the subfault centers, weighting by the slip magnitude in that subfault. The centroid depth of the coseismic models within 10% of the best fitting model χ^2 is also shown in Figure B.3, indicating that models with centroid depths at the shallower end were favored in the integrated search the initial uniform, particularly for the MeiNong earthquake.

Figures B.4 and B.5 show the residuals of the best fit coseismic models for each earthquake. Figure B.5 shows the GNSS residuals of the best fit coseismic models of both earthquakes, with the predictions shown along with the observations in Figure 3.9 of the main text. Figure B.6 shows the residuals between predictions of the best fit MeiNong model and the InSAR observations. Figure B.6 is rendered by showing the LOS residual value at the center point of each of the quadtree decimations, excluding the far-field for clarity, while in Figures 3.3 and 3.4 of the main text, the synthetic interferograms are rendered at the full resolution of the interferograms. The LOS measurements from the interferograms associated with Figures

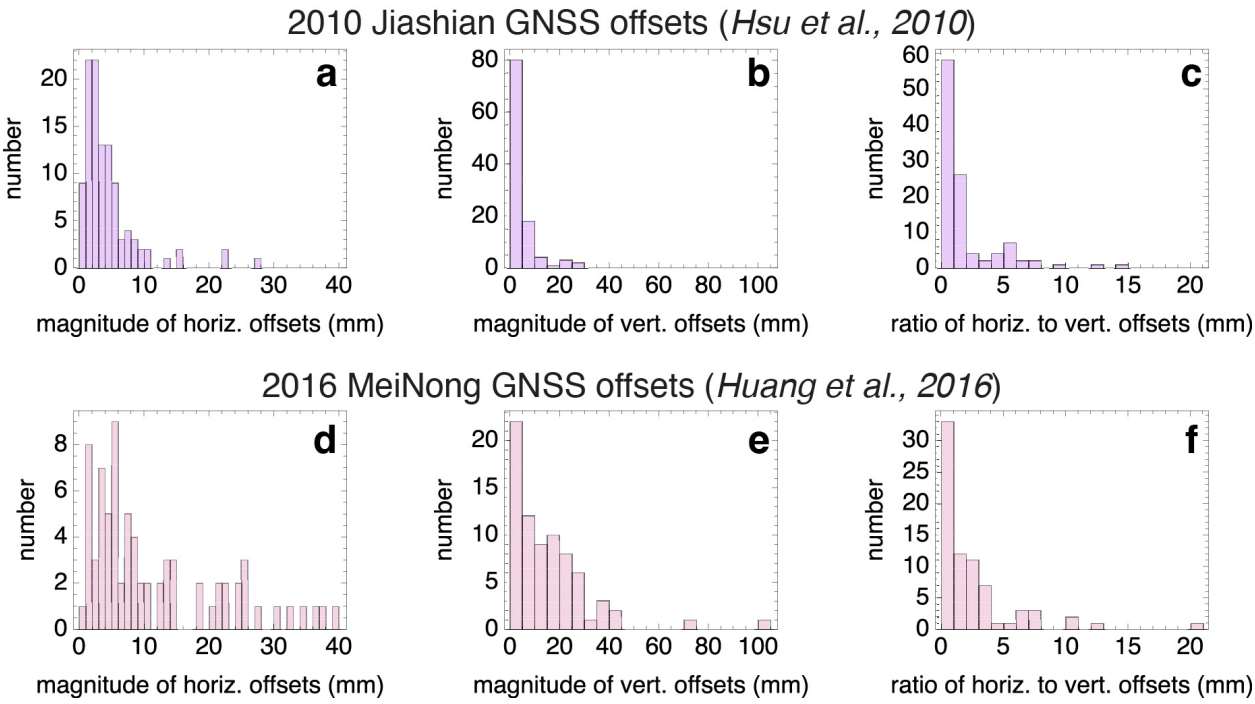


Figure B.1: Histograms of the horizontal (**a** and **d**) or vertical (**b** and **e**) coseismic offsets in the Jiashian (Hsu *et al.*, 2011) and MeiNong (Huang *et al.*, 2016) data. Panels **c** and **f** show the histograms of the ratio of the horizontal to vertical deformation inferred at each station.

B.5a and B.5c were inverted for the cosiemsic model, which those in Figures B.6b and B.6c are just used for testing of the resulting model.

Figure B.6 shows the GCMT double couple mechanism along with the double couple of the best fitting Jiashian coseismic model found in either the initial uniform search or the secondary integrated search. Figure B.4 is a complement of Figure 10 in the main text, which is for the MeiNong earthquake. The double couple of the coseismic models is defined by the fault strike and dip, along with the weighted average slip rake (average of the slip rakes in each subfault, weighted by the magnitude of inferred slip in the subfaults).

Figures B.7 and B.8 show the predicted coseismic surface offsets for a trial MeiNong coseismic model that has a mechanism (*i.e.*, fault strike, dip, and weighted average strike) and centroid depth closest to the GCMT focal mechanism (using the northeastward dipping nodal plane). The strike, dip, and weighted average rake of the alternate model are -83°, 20°, and 20°, while the strike, dip, and rake of the GCMT nodal plane is -81°, 22°, and 21°. The centroid depth of this alternative coseimic model, 16.3 km, is comparable to the GCMT centroid depth of 17.3 km, and is deeper than the centroid depth of the best fitting MeiNong model (10.1 km). For reference, Figure B.7 also shows the predicted GNSS offsets, and their residuals, for the best fitting MeiNong model (see also Figs. 3.9c and 3.9d of the main test).

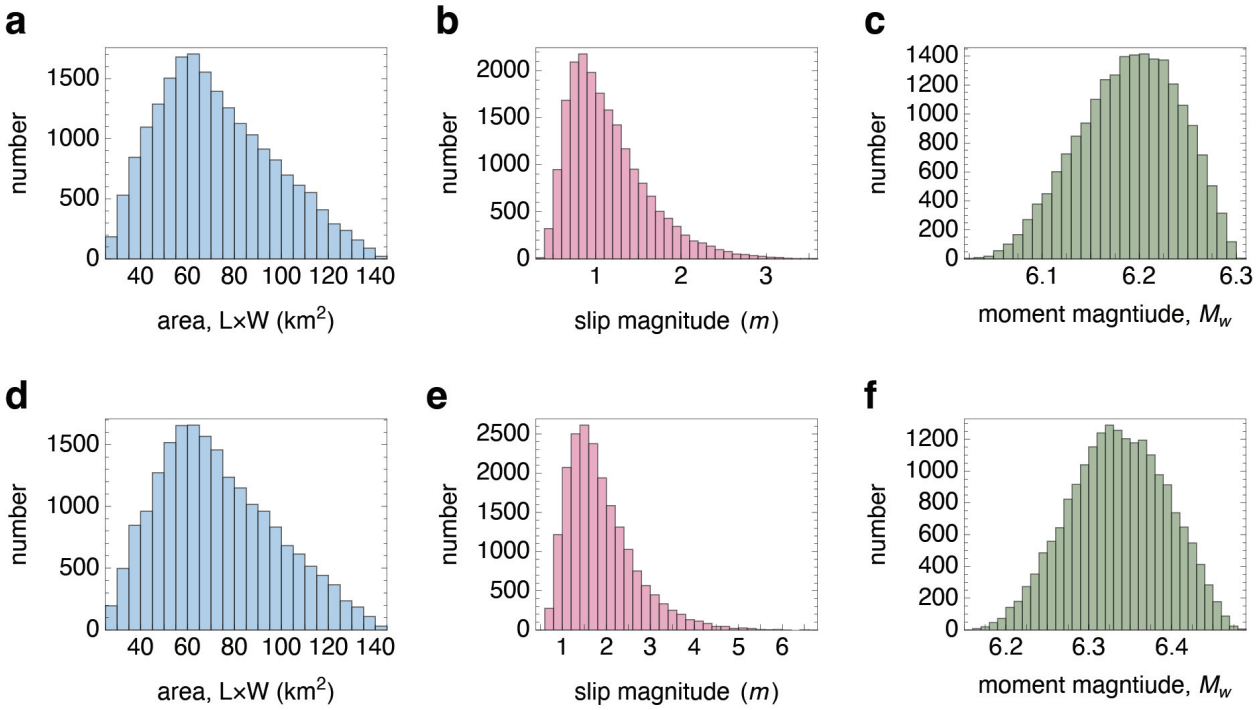


Figure B.2: The fault dimension ($L \times W$; **a** and **d**), slip magnitude (**b** and **e**, and associated moment magnitude (assuming shear modulus of 30 GPa; **c** and **f**) of the best fitting 20,000 models determined in the initial search for the Jiashian (**a**–**c**) and MeiNong (**d**–**f**) earthquakes.

Figure B.9 shows the number of aftershocks on each day including and following the MeiNong earthquake. The aftershocks are from Hsu *et al.*, 2020 and are grouped in one of three clusters shown in Figure 3.12 of the main text (Figs. B.9a, b, and d; clusters are based on those proposed by Hsu *et al.*, 2020, modified to demarcate between above or below the inferred fault surface), or in both of the two clusters proximal to the inferred slip surface of the MeiNong earthquake (Fig. B.9c). For each grouping, an Omori-Utsu aftershock decay, of the form

$$n(t) = \frac{k}{(t+c)^p}, \tag{B.1}$$

where n is number of aftershocks per day t (*e.g.*, Davidson *et al.*, 2015), is shown for reference. The parameters k, c, and p for each were adjusted so that the Omori-Utsu decay most closely follows the aftershock activity, and while the decay models shown are the result of 100,000 trials of random parameters, they are presented merely for reference.

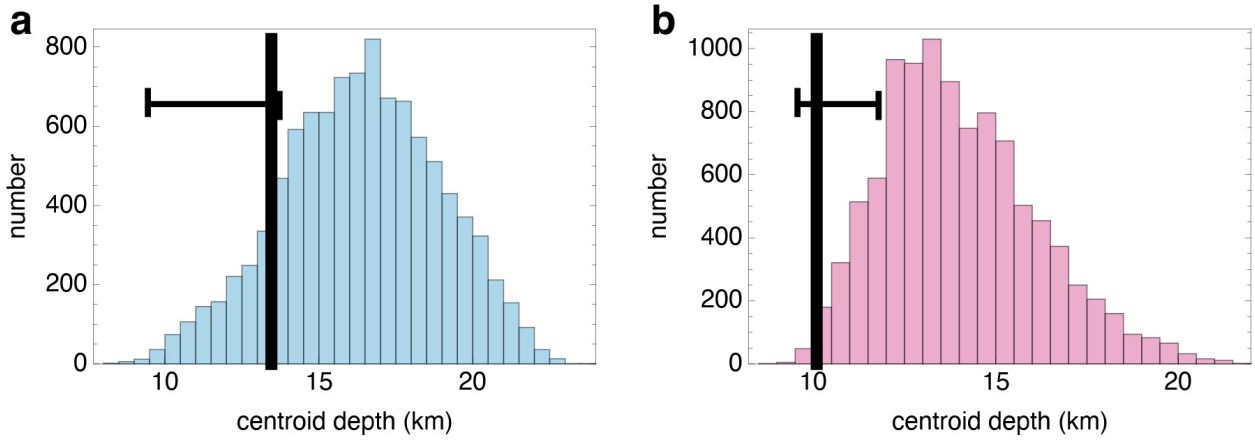


Figure B.3: Centroid depth inferred for all 10,000 trial fault planes in the integrated search of the Jiashian (**a**) or MeiNong (**b**) coseismic slip models. Whiskers indicate the range of centroid depths of the models with χ^2 within the best fit of each coseismic slip model (38 and 107 models for the Jiashian and MeiNong coseismic slip models, respectively).

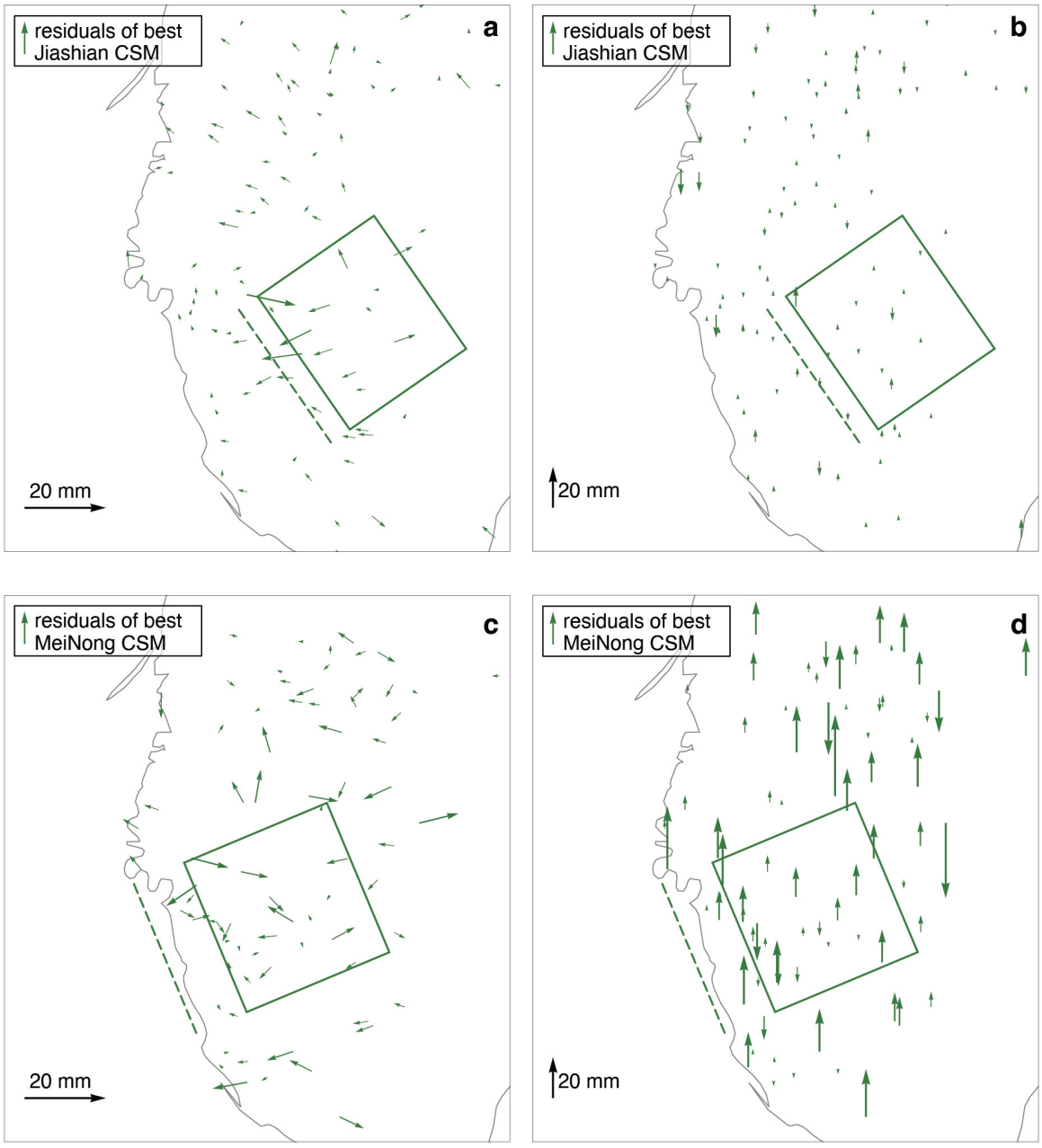


Figure B.4: Residuals between observed and predicted horizontal (**a** and **c**) and vertical (**b** and **d**) for the best coseismic slip model determined of the Jiashian (**a** and **b**) and MeiNong (**c** and **d**) earthquakes. The observed GNSS solutions are shown in black and are from Hsu *et al.*, 2011 (Jiashian; **a** and **b**) or Huang *et al.*, 2016 (MeiNong; **c** and **d**). Green rectangle is the surface projection of the fault planes and green dashed line is the projection of the top of the fault along the constant fault dip.

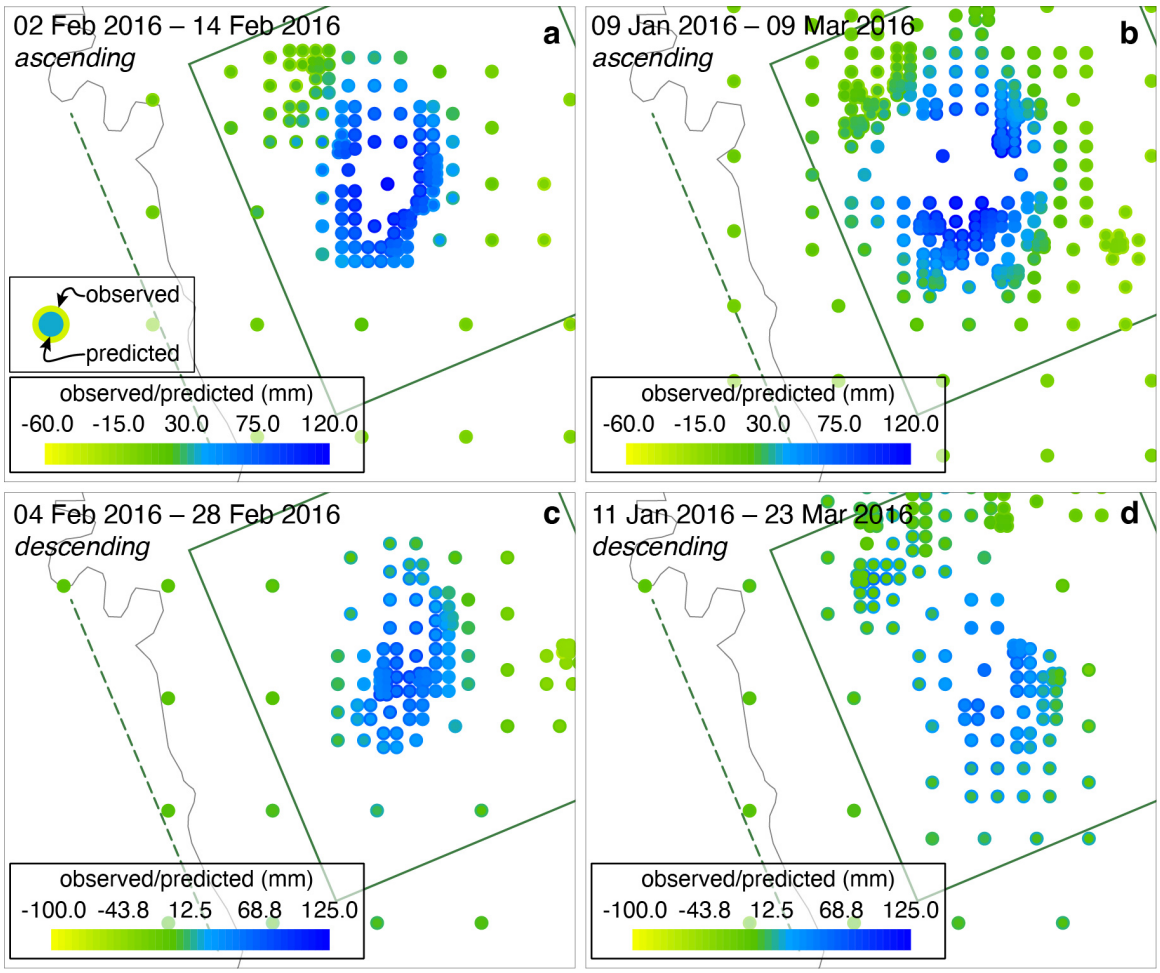


Figure B.5: Observed and predicted LOS offsets at the quadtree sample points for the four interferograms capturing coseismic deformation of the MeiNong earthquake. The predicted LOS offsets are from the coseismic model with the lowest χ^2, where the interferograms in panels (**a**) and (**c**) were inverted to determine the model while the interferograms in panels (**b**) and (**d**) were only used to calculate the χ^2 of that model. Green rectangles indicate the surface projection of the fault plane, and green dashed line is the projection of the top of the fault plane to the surface.

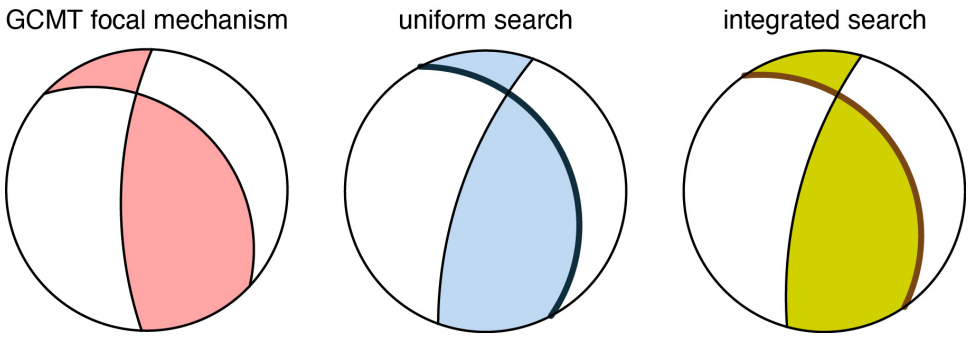


Figure B.6: The GCMT focal mechanism of the Jiashian earthquake compared to the focal mechanisms for the best model found from the initial search assuming uniform slip and from the integrated search (the slip surface is highlighted).

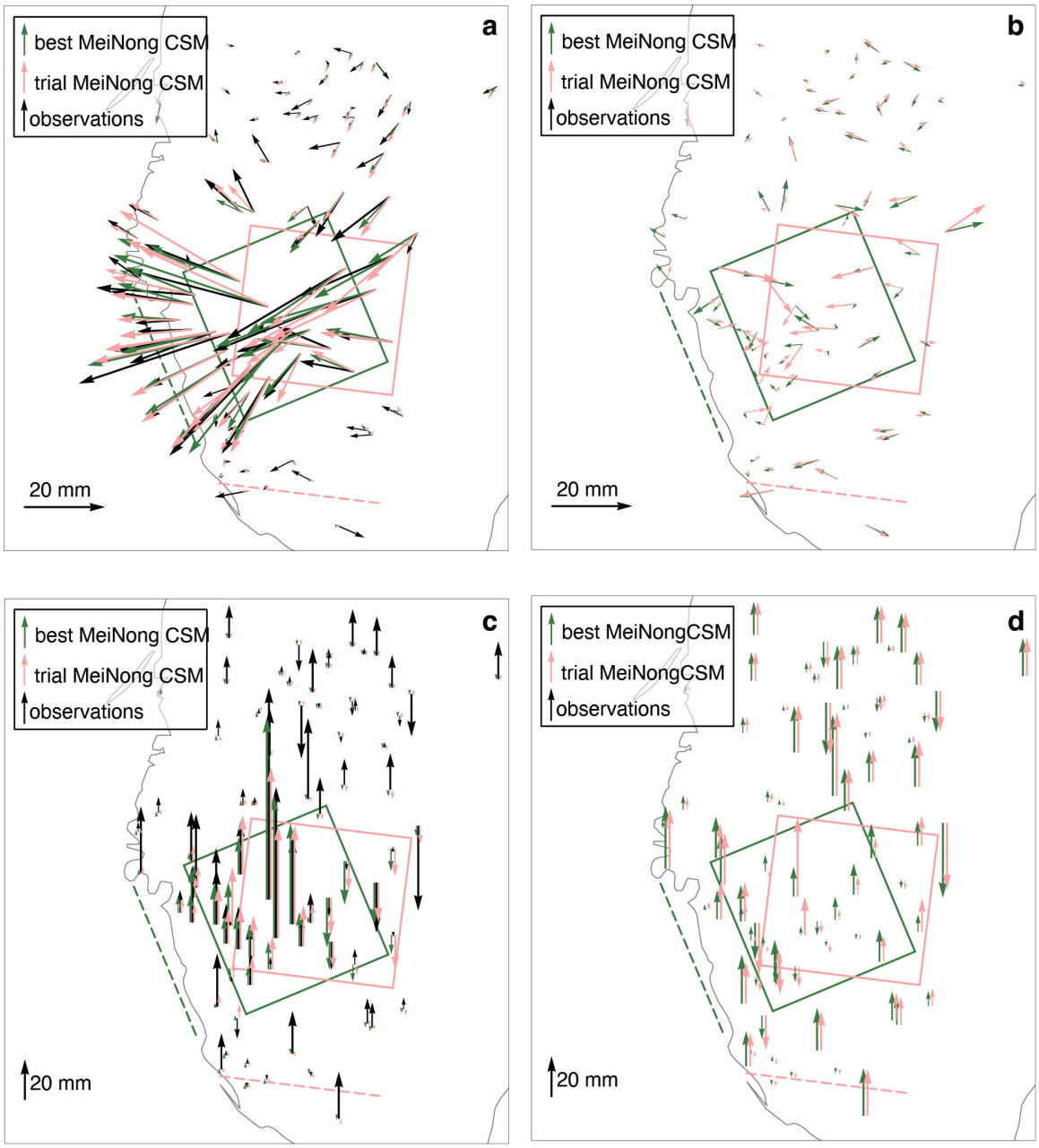


Figure B.7: Observed GNSS offsets of MeiNong coseismic deformation (black) along with the offsets predicted by either the best fit coseismic model (green, as in Fig. 9 of the main text) or an alternative model (pink). Panels (**a**) and (**b**) are the horizontal predictions and residuals, respectively, while panels (**c**) and (**d**) are the vertical predictions and residuals, respectively. Vectors showing the model vertical displacements are slightly offset from the observed for clarity. The alternative model has a strike, dip, and average weighted rake of -83°, 20° 20° and has a centroid depth of 16.3 km (depth to the top of the fault plane is 10.2 km). Rectangle is the surface projection of the fault plane in the best fit (green) or alternative (pink) model, and dashed lines are the updip projection of the top of the fault plane.

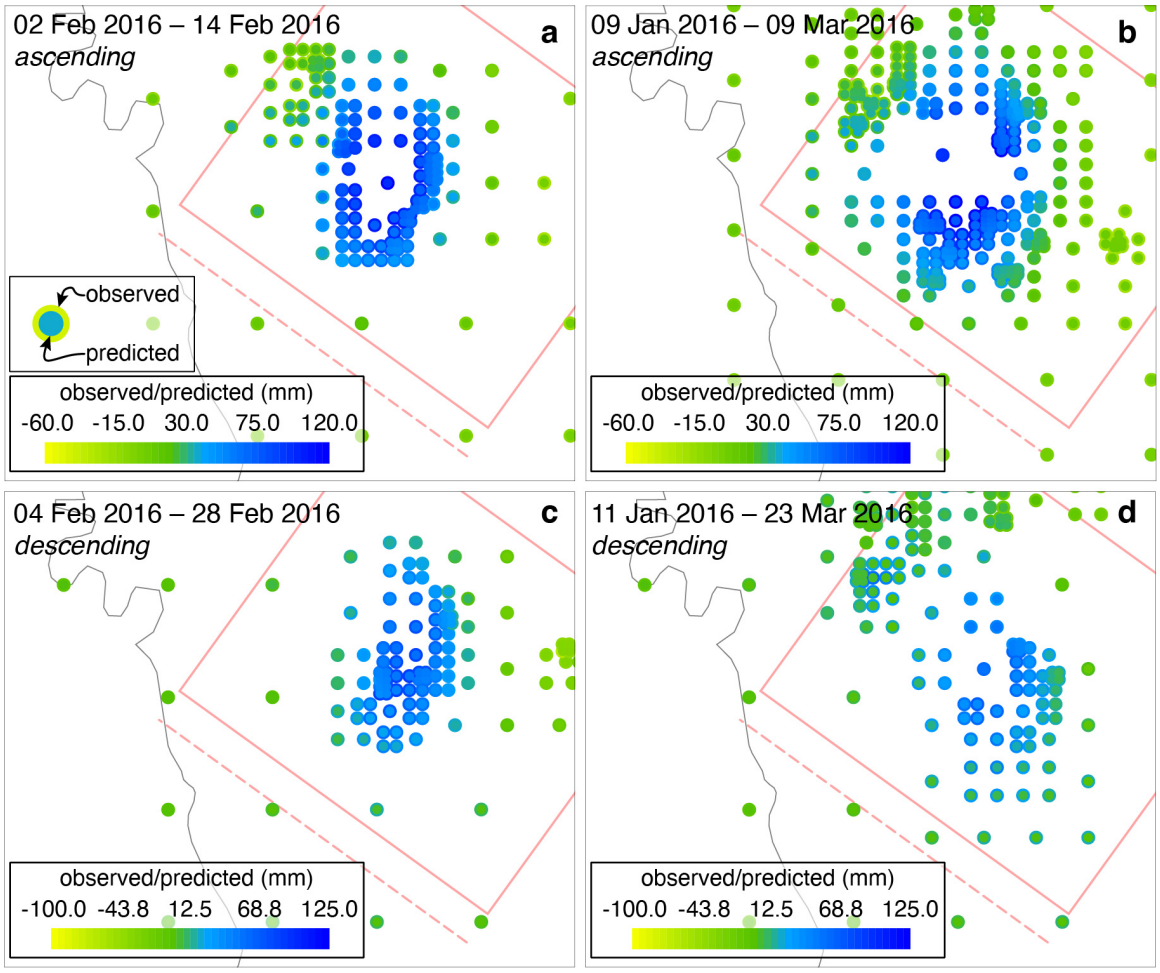


Figure B.8: Observed and predicted LOS offsets at the quadtree sample points for the four interferograms capturing coseismic deformation of the MeiNong earthquake. The predicted LOS offsets are from Fig. B.6 and caption is as in Fig. B.4.

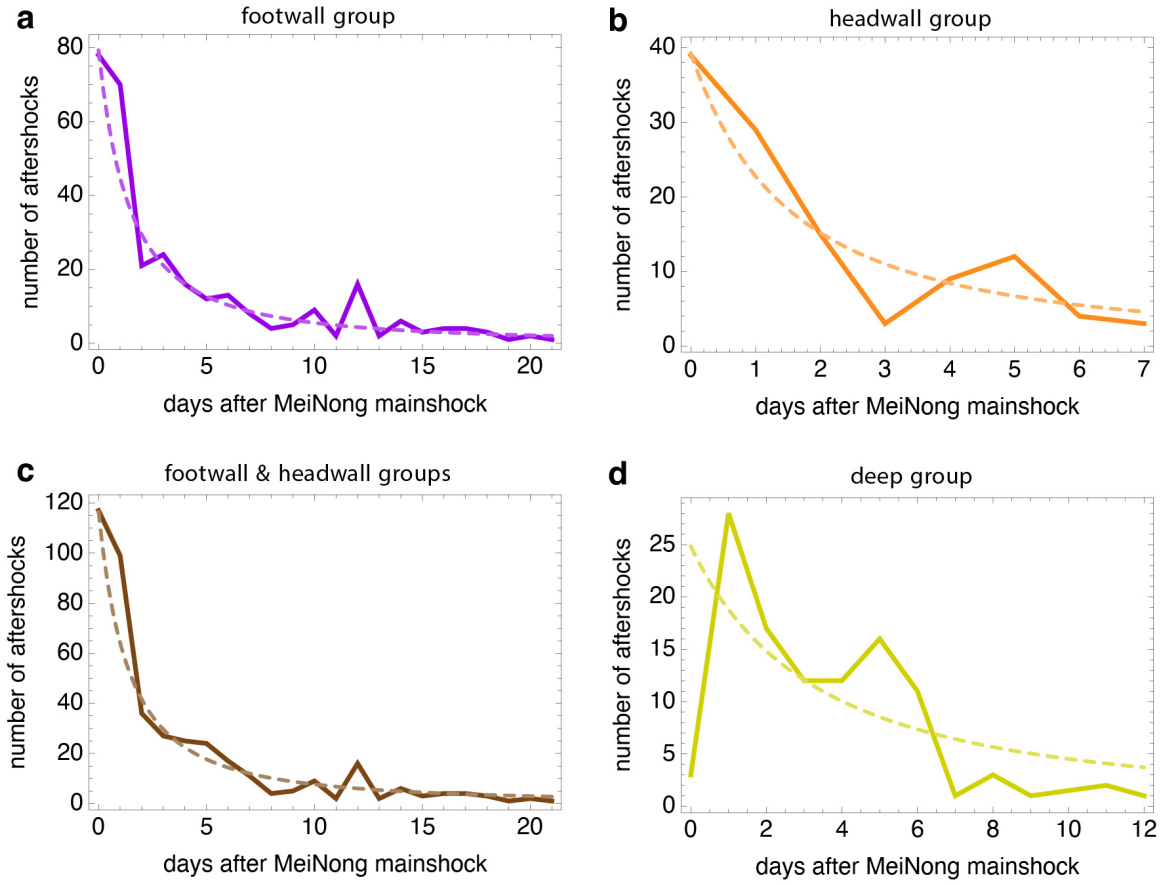


Figure B.9: The number of aftershocks per day following the MeiNong earthquake (data from Hsu *et al.*, 2020), for aftershocks in either one of the groups defined in Fig. 3.12, or in both of the groups associated with the main slip patch we infer in the MeiNong earthquake. The dashed lines are reference Omori-Utsu aftershock decays (*e.g.,* Utsu *et al.*, 1995; Davidson *et al.*, 2015).

APPENDIX C

Supplementary Material for Chapter 4

C.1 Covariance Analysis

When fusing the different data types the question of how the different modalities influence the output covariance naturally arises. To investigate this we will consider a single GNSS observation and a single InSAR observation at different locations, and plug them into the latent factor model.

At a GNSS coordinate ($\bar{x}_G$) we observe displacements ($\mathbf{u}_i$)

$$\mathbf{u}(\bar{x}_G) = \begin{bmatrix} u_x(\bar{x}_G) \\ u_y(\bar{x}_G) \\ u_z(\bar{x}_G) \end{bmatrix} + \begin{bmatrix} \epsilon_x \\ \epsilon_y \\ \epsilon_z \end{bmatrix} \tag{C.1}$$

where $\epsilon_i \sim \mathcal{N}(0, \sigma_i^2)$ and are considered independent here. At a InSAR ground coordinate ($\bar{x}_I$) we observe a LOS range change (ρ)

$$\rho(\bar{x}_I) = \mathbf{r}_{LOS}^T(\bar{x}_I) \begin{bmatrix} u_x(\bar{x}_I) \\ u_y(\bar{x}_I) \\ u_z(\bar{x}_I) \end{bmatrix} + \epsilon_r \tag{C.2}$$

where $\epsilon_r \sim \mathcal{N}(0, \sigma_r^2)$ and is independent of ϵ_i's, $\mathbf{r}_{LOS}^T = (r_x, r_y, r_z) = (\sin\theta\sin\delta, \sin\theta\cos\delta, \cos\theta)$ where θ is LOS incidence angle and δ is LOS bearing.

The mean and prior covariance for the above scenario are given by

$$\mathbf{m}(\bar{x}) = [u_x(\bar{x}_G),\ u_y(\bar{x}_G),\ u_z(\bar{x}_G),\ \rho(\bar{x}_I),\ u_x^*(\bar{x}_G),\ u_y^*(\bar{x}_G),\ u_z^*(\bar{x}_G)]^T \tag{C.3}$$

and

$$\mathbf{K} = \left[\begin{array}{cc|c} K_{GG} & K_{GI} & K_{GG^*} \\ K_{IG} & K_{II} & K_{IG^*} \\ \hline K_{G^*G} & K_{G^*I} & K_{G^*G^*} \end{array}\right] \tag{C.4}$$

The posterior mean and covariance are given by

$$\begin{bmatrix} u_x^*(\bar{x}_G) \\ u_y^*(\bar{x}_G) \\ u_z^*(\bar{x}_G) \end{bmatrix} = [K_{GG^*}\ K_{G^*I}] \left[\begin{bmatrix} K_{GG} & K_{GI} \\ K_{IG} & K_{II} \end{bmatrix} + \begin{bmatrix} \sigma_x^2 & & & \\ & \sigma_y^2 & & \\ & & \sigma_z^2 & \\ & & & \sigma_r^2 \end{bmatrix} \right]^{-1} \begin{matrix} u_x(\bar{x}_G) \\ u_y(\bar{x}_G) \\ u_z(\bar{x}_G) \\ \rho(\bar{x}_I) \end{matrix} \tag{C.5}$$

and

$$K^* = K_{G^*G^*} - [K_{GG^*}\ K_{G^*I}] \left[\begin{bmatrix} K_{GG} & K_{GI} \\ K_{IG} & K_{II} \end{bmatrix} + \begin{bmatrix} \sigma_x^2 & & & \\ & \sigma_y^2 & & \\ & & \sigma_z^2 & \\ & & & \sigma_r^2 \end{bmatrix} \right]^{-1} \begin{bmatrix} K_{GG^*} \\ K_{IG^*} \end{bmatrix} \tag{C.6}$$

Defining each sub-matrix assuming that $u_x(\bar{x}_G)$, $u_y(\bar{x}_G)$, and $u_z(\bar{x}_G)$ uncorrelated,

$$K_{GG} = \begin{bmatrix} k_x(\bar{x}_G, \bar{x}_G) & 0 & 0 \\ 0 & k_y(\bar{x}_G, \bar{x}_G) & 0 \\ 0 & 0 & k_z(\bar{x}_G, \bar{x}_G) \end{bmatrix} \tag{C.7}$$

$$K_{GI} = \begin{bmatrix} r_x(\bar{x}_I)k_x(\bar{x}_G, \bar{x}_I) \\ r_y(\bar{x}_I)k_y(\bar{x}_G, \bar{x}_I) \\ r_z(\bar{x}_I)k_z(\bar{x}_G, \bar{x}_I) \end{bmatrix} \tag{C.8}$$

$$K_{IG} = \begin{bmatrix} r_x(\bar{x}_I)k_x(\bar{x}_I, \bar{x}_G) & r_y(\bar{x}_I)k_y(\bar{x}_I, \bar{x}_G) & r_z(\bar{x}_I)k_z(\bar{x}_I, \bar{x}_G) \end{bmatrix} \tag{C.9}$$

$$K_{II} = r_x^2(\bar{x}_I)k_x(\bar{x}_I, \bar{x}_I) + r_y^2(\bar{x}_I)k_y(\bar{x}_I, \bar{x}_I) + r_z^2(\bar{x}_I)k_z(\bar{x}_I, \bar{x}_I) \tag{C.10}$$

$$K_{G^*G^*} = K_{GG} = K_{G^*G} = K_{GG^*} \tag{C.11}$$

$$K_{G^*I} = K_{GI} \tag{C.12}$$

$$K_{IG^*} = K_{IG} \tag{C.13}$$

Therefore the solution for the posterior covariance becomes,

$$K^* = K_{GG} - [K_{GG}\, K_{GI}] \begin{bmatrix} K_{GG} + \begin{matrix} \sigma_x^2 & & \\ & \sigma_y^2 & \\ & & \sigma_z^2 \end{matrix} & K_{GI} \\ K_{IG} & K_{II} + \sigma_r^2 \end{bmatrix}^{-1} \begin{bmatrix} K_{GG} \\ K_{IG} \end{bmatrix} \tag{C.14}$$

We will refer to the inverse of the prior covariance as K^{-1}, in other words

$$K^{-1} = \begin{bmatrix} K_{GG} + \begin{matrix} \sigma_x^2 & & \\ & \sigma_y^2 & \\ & & \sigma_z^2 \end{matrix} & K_{GI} \\ K_{IG} & K_{II} + \sigma_r^2 \end{bmatrix}^{-1} \tag{C.15}$$

We can solve K^{-1} using the Schur complement:
First define,

$$C_r = K_{II} - K_{IG} K_{GG}^{-1} K_{GI} \tag{C.16}$$

Noting that for a valid kernel,

$$k_i(\bar{x}_I, \bar{x}_G) = k_i(\bar{x}_G, \bar{x}_I) \tag{C.17}$$

making,

$$\begin{aligned} K_{GI} K_{GG}^{-1} K_{IG} \quad = \quad & \left[k_x(\bar{x}_G, \bar{x}_G) + \sigma_x^2\right]^{-1} r_x^2(\bar{x}_I) k_x^2(\bar{x}_I, \bar{x}_G) \\ & + \left[k_y(\bar{x}_G, \bar{x}_G) + \sigma_y^2\right]^{-1} r_y^2(\bar{x}_I) k_y^2(\bar{x}_I, \bar{x}_G) \\ & + \left[k_z(\bar{x}_G, \bar{x}_G) + \sigma_z^2\right]^{-1} r_z^2(\bar{x}_I) k_z^2(\bar{x}_I, \bar{x}_G) \end{aligned}$$

therefore,

$$C_r = \sum_i^{x,y,z} r_i^2(\bar{x}_I) \left(k_i(\bar{x}_I, \bar{x}_I) - \frac{k_i^2(\bar{x}_I, \bar{x}_G)}{k_i^2(\bar{x}_G, \bar{x}_G) + \sigma_i^2} \right) + \sigma_r^2 \tag{C.18}$$

Finally giving,

$$K^{-1} = \begin{bmatrix} K_{GG}^{-1} + K_{GG}^{-1} K_{GI} C_r^{-1} K_{IG} K_{GG}^{-1} & -K_{GG}^{-1} K_{GI} C_r^{-1} \\ -C_r^{-1} K_{IG} K_{GG}^{-1} & C_r^{-1} \end{bmatrix} \tag{C.19}$$

For simplicity we consider only the squared-exponential (SE) kernel function for the re-

mainder of this analysis, we also use unit signal variance recognizing that the signal variance would only act as a scale factor. Noting that C_r^{-1} is a scalar and,

$$K_{GG}^{-1} = \begin{bmatrix} (1+\sigma_x^2)^{-1} & 0 & 0 \\ 0 & (1+\sigma_y^2)^{-1} & 0 \\ 0 & 0 & (1+\sigma_z^2)^{-1} \end{bmatrix} \tag{C.20}$$

$$K_{II} = \sum_i^{x,y,z} r_i^2 \tag{C.21}$$

we have,

$$K^* = I - K_{GG}^{-1} - C_r^{-1} K_{GG}^{-1} C_x K_{GI} K_{IG} C_x K_{GG}^{-1} \tag{C.22}$$

Recognizing $I - K_{GG}^{-1}$ has diagonal terms $1 - \frac{1}{1+\sigma_i^2} = \frac{\sigma_i^2}{1+\sigma_i^2}$ then,

$$K^* = \begin{bmatrix} \frac{\sigma_x^2}{1+\sigma_x^2} & & \\ & \frac{\sigma_y^2}{1+\sigma_y^2} & \\ & & \frac{\sigma_z^2}{1+\sigma_z^2} \end{bmatrix} - C_r^{-1} \begin{bmatrix} \frac{\sigma_x^2}{1+\sigma_x^2} & & \\ & \frac{\sigma_y^2}{1+\sigma_y^2} & \\ & & \frac{\sigma_z^2}{1+\sigma_z^2} \end{bmatrix} K_{GI} K_{IG} \begin{bmatrix} \frac{\sigma_x^2}{1+\sigma_x^2} & & \\ & \frac{\sigma_y^2}{1+\sigma_y^2} & \\ & & \frac{\sigma_z^2}{1+\sigma_z^2} \end{bmatrix} \tag{C.23}$$

where,

$$K_{GI} K_{IG} = \begin{bmatrix} r_x^2 k^2 x(\bar{x}_I, \bar{x}_G) & & \\ r_y(\bar{x}_I) r_x(\bar{x}_I) k_y(\bar{x}_I, \bar{x}_G) k_x(\bar{x}_I, \bar{x}_G) & & \\ r_z(\bar{x}_I) r_x(\bar{x}_I) k_z(\bar{x}_I, \bar{x}_G) k_x(\bar{x}_I, \bar{x}_G) & & \end{bmatrix}$$
$$\begin{bmatrix} r_x(\bar{x}_I) r_y(\bar{x}_I) k_x(\bar{x}_I, \bar{x}_G) k_y(\bar{x}_I, \bar{x}_G) & r_x(\bar{x}_I) r_z(\bar{x}_I) k_x(\bar{x}_I, \bar{x}_G) k_z(\bar{x}_I, \bar{x}_G) \\ r_y^2 k^2 y(\bar{x}_I, \bar{x}_G) & r_y(\bar{x}_I) r_z(\bar{x}_I) k_y(\bar{x}_I, \bar{x}_G) k_z(\bar{x}_I, \bar{x}_G) \\ r_z(\bar{x}_I) r_y(\bar{x}_I) k_z(\bar{x}_I, \bar{x}_G) k_y(\bar{x}_I, \bar{x}_G) & r_z^2 k^2 z(\bar{x}_I, \bar{x}_G) \end{bmatrix} \tag{C.24}$$

Defining $\Delta i = \frac{\sigma_i^2}{1+\sigma_i^2}$, then $C_r^{-1} K_{GG}^{-1} C_x K_{GI} K_{IG} C_x K_{GG}^{-1} = P$ can have it's elements given by,

$$P_{ij} = r_i(\bar{x}_I) r_j(\bar{x}_I) k_i(\bar{x}_I, \bar{x}_I) k_j(\bar{x}_I, \bar{x}_I) \Delta i \Delta j C_r^{-1} \tag{C.25}$$

where $i, j \in \{x, y, z\}$. Following this, the diagonal elements of K^* are

$$K_{ii}^* = \Delta i - \Delta i^2 C_r^{-1} r_i^2(\bar{x}_I) K_I^2(\bar{x}_I, \bar{x}_G) \tag{C.26}$$

where,

$$C_r = \sum_{i}^{x,y,z} r_i^2(\bar{x}_I) \left(1 - \frac{k_i(\bar{x}_I, \bar{x}_G)}{1 + \sigma_i^2}\right) + \sigma_r^2 \tag{C.27}$$

From the above we can see that variance/covariance reductions are solely dependent on the look angles for the SE radial basis functions describing uncorrelated Gaussian processes when two locations are correlated.

C.2 Additional Figures

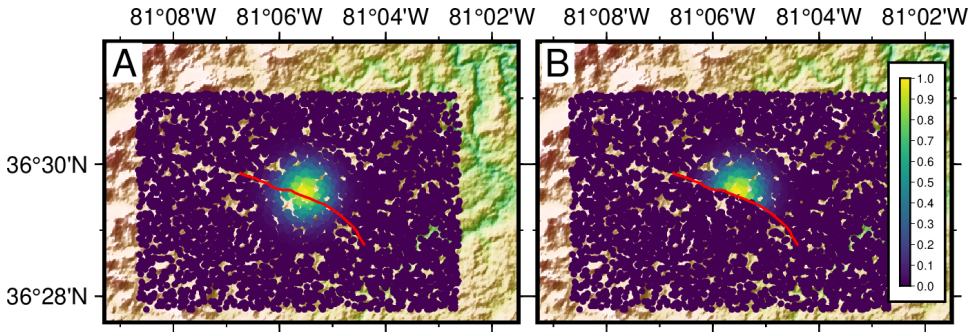


Figure S1: Correlation of random sample locations with near-surface rupture location, the red line is the mapped surface rupture, and the color bar is shared. Panel (A) shows correlation between locations calculated using an unmodified squared-exponential kernel. Panel (B) shows correlation between locations calculated using the modified squared-exponential designed to accommodate the discontinuity created by the surface rupture.

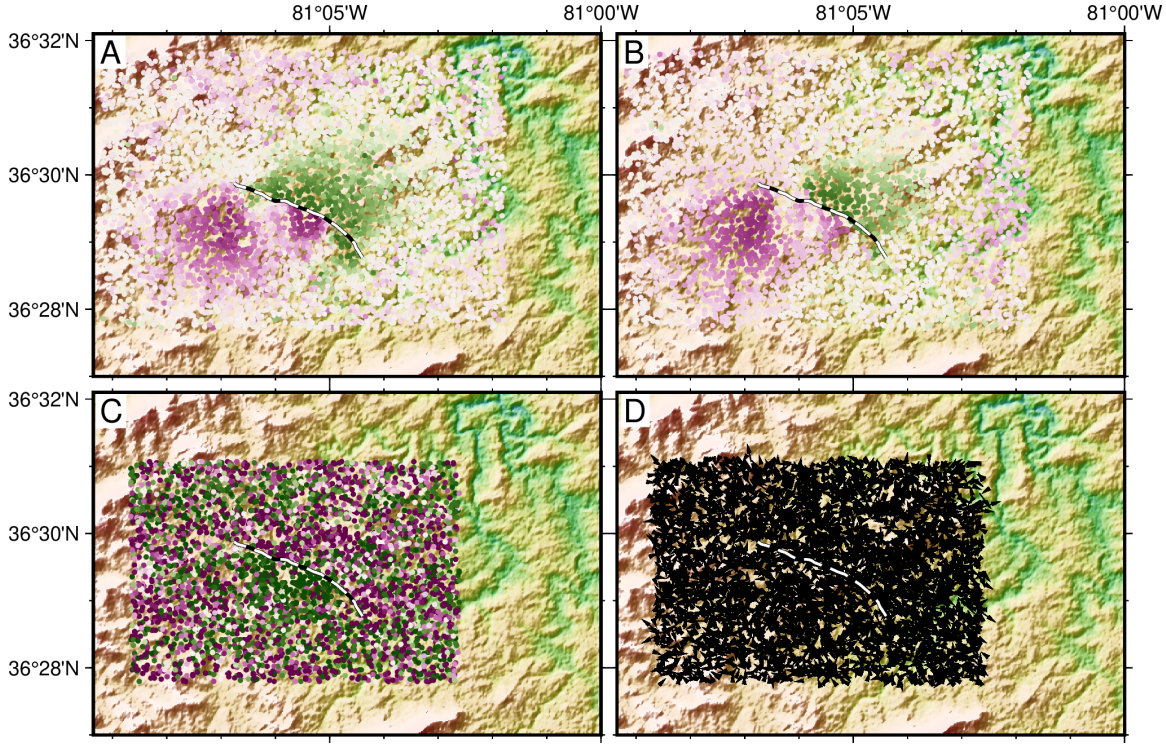


Figure S2: Uniform random sampling used for Sparta 2020, earthquake data fusion. Panel (A) shows samples from Sentinel-1 interferogram, panel (B) shows samples from the ALOS-2 interferogram, and panels (C) and (D) shows samples from 3-D differential LiDAR vertical and horizontal components, respectively. All 3-D differential LiDAR samples are collocated.

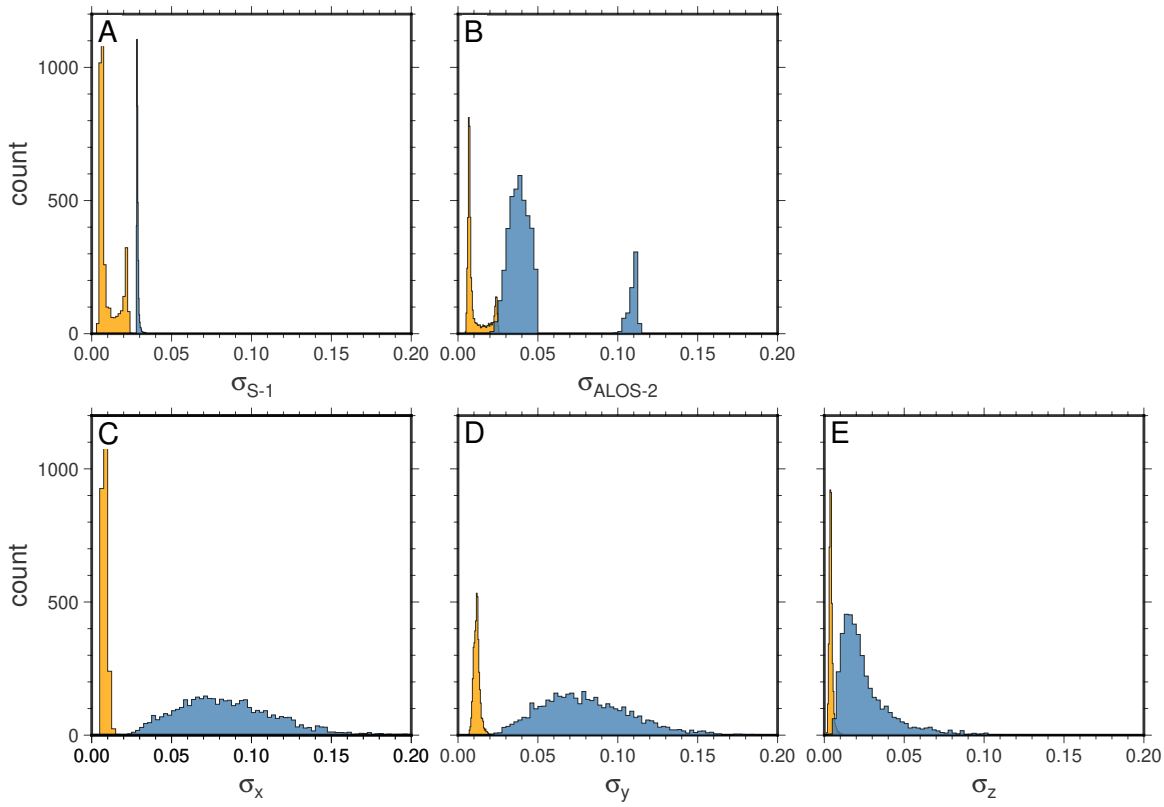


Figure S3: Histograms of Sparta data uncertainties (blue) prior to fusion by Gentoo and uncertainties for the posterior samples (orange) at the same locations. Panels: (A) S-1 (B) ALOS-2 (C) LiDAR-x (D) LiDAR-y (E) LiDAR-z

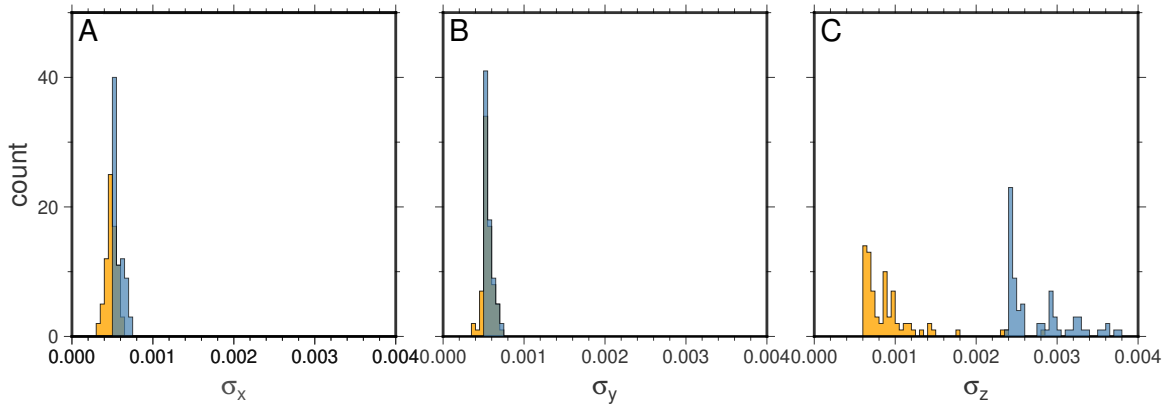


Figure S4: Histograms of MeiNong data uncertainties (blue) prior to fusion by Gentoo and uncertainties for the posterior samples (orange) at the same locations. Panels: (A) GNSS-x (B) GNSS-y (C) GNSS-z

BIBLIOGRAPHY

Anderson, E. M. (1905). The dynamics of faulting. *Transactions of the Edinburgh Geological Society*, 8(3):387–402.

Bányai, L., Szűcs, E., and Wesztergom, V. (2017). Geometric features of los data derived by sar psi technologies and the three-dimensional data fusion. *Acta Geodaetica et Geophysica*, 52:421–436.

Bekaert, D., Hooper, A., and Wright, T. (2015). A spatially variable power law tropospheric correction technique for insar data. *Journal of Geophysical Research: Solid Earth*, 120(2):1345–1356.

Belot, G. (2015). Down to earth underdetermination. *Philosophy and Phenomenological Research*, 91(2):456–464.

Besl, P. J. and McKay, N. D. (1992). Method for registration of 3-d shapes. In *Sensor fusion IV: control paradigms and data structures*, volume 1611, pages 586–606. Spie.

Bessel, F. W. and Baeyer, J. J. (1838). *Gradmessung in Ostpreußen und ihre Verbindung mit preußischen und russischen Dreiecksketten*. Gedruckt in der Druckerei der Königlichen Akademie der Wissenschaften 1838 ....

Blewitt, G., Hammond, W. C., and Kreemer, C. (2018). Harnessing the gps data explosion for interdisciplinary science. *Eos*, 99.

Boche, H., Caire, G., Calderbank, R., Kutyniok, G., Mathar, R., and Petersen, P. (2019). *Compressed Sensing and Its Applications: Third International MATHEON Conference 2017*. Birkhäuser.

Bollinger, G. and Wheeler, R. L. (1983). The giles county, virginia, seismic zone. *Science*, 219(4588):1063–1065.

Bott, M. H. P. (1959). The mechanics of oblique slip faulting. *Geological magazine*, 96(2):109–117.

Boyd, S. and Vandenberghe, L. (2004). *Convex optimization*. Cambridge university press.

Brune, J. N. (1970). Tectonic stress and the spectra of seismic shear waves from earthquakes. *Journal of geophysical research*, 75(26):4997–5009.

Cattin, R., Briole, P., Lyon-Caen, H., Bernard, P., and Pinettes, P. (1999). Effects of superficial layers on coseismic displacements for a dip-slip fault and geophysical implications. *Geophysical Journal International*, 137(1):149–158.

Cavalié, O., Doin, M.-P., Lasserre, C., and Briole, P. (2007). Ground motion measurement in the lake mead area, nevada, by differential synthetic aperture radar interferometry time series analysis: Probing the lithosphere rheological structure. *Journal of Geophysical Research: Solid Earth*, 112(B3).

Chen, C. W. and Zebker, H. A. (2002). Phase unwrapping for large sar interferograms: Statistical segmentation and generalized network models. *IEEE Transactions on Geoscience and Remote Sensing*, 40(8):1709–1719.

Chen, X., Kim, S., Lin, Q., Carbonell, J. G., and Xing, E. P. (2010). Graph-structured multi-task regression and an efficient optimization method for general fused lasso. *arXiv preprint arXiv:1005.3579*.

Chen, Y. and Medioni, G. (1992). Object modelling by registration of multiple range images. *Image and vision computing*, 10(3):145–155.

Chiang, P.-H., Hsu, Y.-J., and Chang, W.-L. (2016). Fault modeling of the 2012 wutai, taiwan earthquake and its tectonic implications. *Tectonophysics*, 666:66–75.

Clarke, P., Paradissis, D., Briole, P., England, P., Parsons, B., Billiris, H., Veis, G., and Ruegg, J.-C. (1997). Geodetic investigation of the 13 may 1995 kozani-grevena (greece) earthquake. *Geophysical Research Letters*, 24(6):707–710.

Crow, P., Benham, S., Devereux, B. J., and Amable, G. S. (2007). Woodland vegetation and its implications for archaeological survey using lidar. *Forestry*, 80(3):241–252.

Davidsen, J., Gu, C., and Baiesi, M. (2015). Generalized omori–utsu law for aftershock sequences in southern california. *Geophysical Journal International*, 201(2):965–978.

Delacourt, C., Briole, P., and Achache, J. (1998). Tropospheric corrections of sar interferograms with strong topography. application to etna. *Geophysical Research Letters*, 25(15):2849–2852.

Delouis, B., Giardini, D., Lundgren, P., and Salichon, J. (2002). Joint inversion of insar, gps, teleseismic, and strong-motion data for the spatial and temporal distribution of earthquake slip: Application to the 1999 izmit mainshock. *Bulletin of the Seismological Society of America*, 92(1):278–299.

Dong, D., Fang, P., Bock, Y., Cheng, M., and Miyazaki, S. (2002). Anatomy of apparent seasonal variations from gps-derived site position time series. *Journal of Geophysical Research: Solid Earth*, 107(B4):ETG–9.

Donoho, D. L. (2006). For most large underdetermined systems of equations, the minimal l1-norm near-solution approximates the sparest near-solution. *Communications on Pure and Applied Mathematics*, 59:0907–0934.

Duvenaud, D. (2014). *Automatic model construction with Gaussian processes*. PhD thesis, University of Cambridge.

Emardson, T., Simons, M., and Webb, F. (2003). Neutral atmospheric delay in interferometric synthetic aperture radar applications: Statistical description and mitigation. *Journal of Geophysical Research: Solid Earth*, 108(B5).

Evans, E. L. and Meade, B. J. (2012). Geodetic imaging of coseismic slip and postseismic afterslip: Sparsity promoting methods applied to the great tohoku earthquake. *Geophysical Research Letters*, 39(11).

Feng, G., Hetland, E. A., Ding, X., Li, Z., and Zhang, L. (2010). Coseismic fault slip of the 2008 mw 7.9 wenchuan earthquake estimated from insar and gps measurements. *Geophysical research letters*, 37(1).

Field, E. H., Arrowsmith, R. J., Biasi, G. P., Bird, P., Dawson, T. E., Felzer, K. R., Jackson, D. D., Johnson, K. M., Jordan, T. H., Madden, C., et al. (2014). Uniform california earthquake rupture forecast, version 3 (ucerf3)—the time-independent model. *Bulletin of the Seismological Society of America*, 104(3):1122–1180.

Figueiredo, P., Owen, L., Hill, J., Merschat, A., Scheip, C., Stewart, K. G., Carter, M., Wooten, R., Wegmann, K., Bohnenstiehl, D., Cattanach, B., Douglas, T. J., Szymanski, E., Witt., A., Horton, S. P., and Thompson, G. W. (2022). The mw 5.1, 9 august 2020, sparta earthquake, north carolina: The first documented seismic surface rupture in the eastern united states. *GSA Today*, 32:4–11.

Gamba, P., Dell Acqua, F., and Houshmand, B. (2002). Srtm data characterization in urban areas. *International Archives of Photogrammetry Remote Sensing and Spatial Information Sciences*, 34(3/B):55–58.

Gao, H., Liao, M., and Feng, G. (2021). An improved quadtree sampling method for insar seismic deformation inversion. *Remote Sensing*, 13(9):1678.

Glennie, C. L., Hinojosa-Corona, A., Nissen, E., Kusari, A., Oskin, M. E., Arrowsmith, J. R., and Borsa, A. (2014). Optimization of legacy lidar data sets for measuring near-field earthquake displacements. *Geophysical Research Letters*, 41(10):3494–3501.

Goldstein, R. M. and Werner, C. L. (1998). Radar interferogram filtering for geophysical applications. *Geophysical research letters*, 25(21):4035–4038.

Google (2020). Maps data: Google, ©2020 cnes / astrium, maxar technologies.

Gourmelen, N. and Amelung, F. (2005). Towards a continental scale deformation map of the western basin and range from insar. In *AGU Fall Meeting Abstracts*, volume 2005, pages G51C–0845.

Gudmundsson, S., Sigmundsson, F., and Carstensen, J. M. (2002). Three-dimensional surface motion maps estimated from combined interferometric synthetic aperture radar and gps data. *Journal of Geophysical Research: Solid Earth*, 107(B10):ETG–13.

Guglielmino, F., Bignami, C., Bonforte, A., Briole, P., Obrizzo, F., Puglisi, G., Stramondo, S., and Wegmüller, U. (2011). Analysis of satellite and in situ ground deformation data integrated by the sistem approach: The april 3, 2010 earthquake along the pernicana fault (mt. etna-italy) case study. *Earth and Planetary Science Letters*, 312(3-4):327–336.

Hammond, W. C., Burgette, R. J., Johnson, K. M., and Blewitt, G. (2018). Uplift of the western transverse ranges and ventura area of southern california: A four-technique geodetic study combining gps, insar, leveling, and tide gauges. *Journal of Geophysical Research: Solid Earth*, 123(1):836–858.

Hansen, P. (1999). The l-curve and its use in the numerical treatment of inverse problems.

Hanssen, R. F. (2001). *Radar Interferometry: Data Interpretation and Error Analysis*. Kluwer Academic Publishers.

Hayford, J. F. (1909). *Geodesy: The Figure of the Earth and Isostasy from Measurements in the United States*. Number 82. US Government Printing Office.

He, P., Hetland, E. A., Wang, Q., Ding, K., Wen, Y., and Zou, R. (2017). Coseismic slip in the 2016 mw 7.8 ecuador earthquake imaged from sentinel-1a radar interferometry. *Seismological Research Letters*, 88(2A):277–286.

He, P., Wen, Y., Xu, C., and Chen, Y. (2019). Complete three-dimensional near-field surface displacements from imaging geodesy techniques applied to the 2016 kumamoto earthquake. *Remote Sensing of Environment*, 232:111321.

Hearn, E. H. and Bürgmann, R. (2005). The effect of elastic layering on inversions of gps data for coseismic slip and resulting stress changes: Strike-slip earthquakes. *Bulletin of the Seismological Society of America*, 95(5):1637–1653.

Heidbach, O., Tingay, M., Barth, A., Reinecker, J., Kurfeß, D., and Müller, B. (2010). Global crustal stress pattern based on the world stress map database release 2008. *Tectonophysics*, 482(1-4):3–15.

Heidbach, O. and Ziegler, M. (2018). Smoothed global stress maps based on the world stress maps database release 2016.

Helmert, F. R. (1880). *Die mathematischen und physikalischen Theorien der höheren Geodäsie (pt: As Teorias Matemáticas e Físicas da Geodésia Superior), 1ª parte*. Leipzig.

Helmert, F. R. (1884). *Die mathematischen und physikalischen Theorieen der höheren Geodäsie*, volume 2. BG Teubner.

Herring, T. A., Melbourne, T. I., Murray, M. H., Floyd, M. A., Szeliga, W. M., King, R. W., Phillips, D. A., Puskas, C. M., Santillan, M., and Wang, L. (2016). Plate boundary observatory and related networks: Gps data analysis methods and geodetic products. *Reviews of Geophysics*, 54(4):759–808.

Hill, J., Cattanach, B., Douglas, T., Figueiredo, P., Kirby, E., Korte, D., Lynn, A., Merschat, A., Owen, L., Scheip, C., Stewart, K., Wells, S., and Wooten, R. (2020). 2020, surface rupture of the little river fault in response to the august 9, 2020 mw 5.1 earthquake near sparta, north carolina. In *2020 Southern California Earthquake Center Annual Meeting, contribution 10742*.

Hines, T. and Hetland, E. (2018). Revealing transient strain in geodetic data with gaussian process regression. *Geophysical Journal International*, 212(3):2116–2130.

Hsu, Y.-F., Huang, H.-H., Huang, M.-H., Tsai, V., Chuang, R., Feng, K.-F., and Lin, S.-H. (2020). Evidence for fluid migration during the 2016 meinong, taiwan, aftershock sequence. *Journal of Geophysical Research: Solid Earth*, 125(9):e2020JB019994.

Hsu, Y.-J., Yu, S.-B., Kuo, L.-C., Tsai, Y.-C., and Chen, H.-Y. (2011). Coseismic deformation of the 2010 jiashian, taiwan earthquake and implications for fault activities in southwestern taiwan. *Tectonophysics*, 502(3-4):328–335.

Huang, H.-H., Yih-Min, W., Ting-Li, L., Wei-An, C., Shyu, J. B. H., Chung-Han, C., and Chang, C.-H. (2011). The preliminary study of the 4 march 2010 mw 6.3 jiasian, taiwan earthquake sequence. *TAO: Terrestrial, Atmospheric and Oceanic Sciences*, 22(3):2.

Huang, M.-H., Tung, H., Fielding, E. J., Huang, H.-H., Liang, C., Huang, C., and Hu, J.-C. (2016). Multiple fault slip triggered above the 2016 mw 6.4 meinong earthquake in taiwan. *Geophysical Research Letters*, 43(14):7459–7467.

Huang, Y., Ellsworth, W. L., and Beroza, G. C. (2017). Stress drops of induced and tectonic earthquakes in the central united states are indistinguishable. *Science advances*, 3(8):e1700772.

Jónsson, S., Zebker, H., Segall, P., and Amelung, F. (2002). Fault slip distribution of the 1999 m w 7.1 hector mine, california, earthquake, estimated from satellite radar and gps measurements. *Bulletin of the Seismological Society of America*, 92(4):1377–1389.

Lajoie, L. J., Nissen, E., Johnson, K. L., Arrowsmith, J. R., Glennie, C. L., Hinojosa-Corona, A., and Oskin, M. E. (2019). Extent of low-angle normal slip in the 2010 el mayor-cucapah (mexico) earthquake from differential lidar. *Journal of Geophysical Research: Solid Earth*, 124(1):943–956.

Langer, L., Ragon, T., Sladen, A., and Tromp, J. (2020). Impact of topography on earthquake static slip estimates. *Tectonophysics*, 791:228566.

Lawson, A. C. (1906). Report of the state earthquake investigation commission. *The California earthquake of April 18*, 1:1–451.

Lee, S.-J., Mozziconacci, L., Liang, W.-T., Hsu, Y.-J., Huang, W.-G., and Huang, B.-S. (2013). Source complexity of the 4 march 2010 jiashian, taiwan, earthquake determined by joint inversion of teleseismic and near field data. *Journal of Asian Earth Sciences*, 64:14–26.

Lee, S.-J., Yeh, T.-Y., Huang, H.-H., and Lin, C.-H. (2015). Numerical earthquake models of the 2013 nantou, taiwan, earthquake series: Characteristics of source rupture processes, strong ground motions and their tectonic implication. *Journal of Asian Earth Sciences*, 111:365–372.

Li, Z., Fielding, E., Cross, P., and Preusker, R. (2009). Advanced insar atmospheric correction: Meris/modis combination and stacked water vapour models. *International Journal of Remote Sensing*, 30(13):3343–3363.

Liang, H., Xu, W., Ding, X., Zhang, L., and Wu, S. (2021). Urban sensing with spaceborne interferometric synthetic aperture radar. In *Urban Informatics*, pages 345–365. Springer.

Lin, Y.-n. N., Kositsky, A. P., and Avouac, J.-P. (2010). Pcaim joint inversion of insar and ground-based geodetic time series: Application to monitoring magmatic inflation beneath the long valley caldera. *Geophysical Research Letters*, 37(23).

Lohman, R. and Simons, M. (2005). Locations of selected small earthquakes in the zagros mountains. *Geochemistry, Geophysics, Geosystems*, 6(3).

Lundgren, P., Hetland, E. A., Liu, Z., and Fielding, E. J. (2009). Southern san andreas-san jacinto fault system slip rates estimated from earthquake cycle models constrained by gps and interferometric synthetic aperture radar observations. *Journal of Geophysical Research: Solid Earth*, 114(B2).

Massonnet, D. and Feigl, K. L. (1998). Radar interferometry and its application to changes in the earth's surface. *Reviews of geophysics*, 36(4):441–500.

Miller, K. (1970). Least squares methods for ill-posed problems with a prescribed bound. *SIAM Journal of Mathematical Analysis*, 1.

Minson, S., Simons, M., and Beck, J. (2013). Bayesian inversion for finite fault earthquake source models i—theory and algorithm. *Geophysical Journal International*, 194(3):1701–1726.

Misra, P., Avtar, R., and Takeuchi, W. (2018). Comparison of digital building height models extracted from aw3d, tandem-x, aster, and srtm digital surface models over yangon city. *Remote Sensing*, 10(12):2008.

Mogi, K. (1958). Relations between the eruptions of various volcanoes and the deformations of the ground surfaces around them. *Bulletin of the Earthquake Research Institute*, 36:99–134.

Muller, C., del Potro, R., Biggs, J., Gottsmann, J., Ebmeier, S. K., Guillaume, S., Cattin, P.-H., and Van der Laat, R. (2014). Integrated velocity field from ground and satellite geodetic techniques: application to Arenal volcano. *Geophysical Journal International*, 200(2):863–879.

Murphy, K. P. (2012). *Machine Learning: A Probabilistic Perspective*. MIT press.

Murray, K. D., Bekaert, D. P., and Lohman, R. B. (2019). Tropospheric corrections for insar: Statistical assessments and applications to the central united states and mexico. *Remote Sensing of Environment*, 232:111326.

Nissen, E., Krishnan, A. K., Arrowsmith, J. R., and Saripalli, S. (2012). Three-dimensional surface displacements and rotations from differencing pre-and post-earthquake lidar point clouds. *Geophysical Research Letters*, 39(16).

NOAA National Centers for Environmental Information (2023). National geophysical data center / world data service (ngdc/wds): Ncei/wds global significant earthquake database. doi:10.7289/V5TD9V7K. Accessed: 23 May 2023.

Noda, H., Lapusta, N., and Kanamori, H. (2013). Comparison of average stress drop measures for ruptures with heterogeneous stress change and implications for earthquake physics. *Geophysical Journal International*, 193(3):1691–1712.

Okada, Y. (1985). Surface deformation due to shear and tensile faults in a half-space. *Bulletin of the Seismological Society of America*, 75:1135–1154.

Okada, Y. (1992). Internal deformation due to shear and tensile faults in a half-space. *Bulletin of the seismological society of America*, 82(2):1018–1040.

Peltzer, G., Crampé, F., Hensley, S., and Rosen, P. (2001). Transient strain accumulation and fault interaction in the eastern california shear zone. *Geology*, 29(11):975–978.

Plafker, G. (1965). Tectonic deformation associated with the 1964 alaska earthquake: The earthquake of 27 march 1964 resulted in observable crustal deformation of unprecedented areal extent. *Science*, 148(3678):1675–1687.

Pollitz, F. F. (2023). Shallow fault slip of the 2020 m 5.1 sparta, north carolina, earthquake. *Seismological Research Letters*, 94(6):2831–2839.

Powell, C. A., Bollinger, G., Chapman, M. C., Sibol, M. S., Johnston, A. C., and Wheeler, R. L. (1994). A seismotectonic model for the 300-kilometer-long eastern tennessee seismic zone. *Science*, 264(5159):686–688.

Pritchard, M., Ji, C., and Simons, M. (2006). Distribution of slip from 11 mw¿ 6 earthquakes in the northern chile subduction zone. *Journal of Geophysical Research: Solid Earth*, 111(B10).

Qiu, D., Wang, Y., Zhang, Y., Tong, Y., Liang, H., Ding, K.-l., Wan, S., and Wang, J. (2023). Settlement monitoring data fusion approach for high-speed railways based on gnss and insar. *Journal of Applied Remote Sensing*, 17(3):034507–034507.

Qu, C., Zuo, R., Shan, X., Hu, J.-c., and Zhang, G. (2017). Coseismic deformation of the 2016 taiwan mw6. 3 earthquake using insar data and source slip inversion. *Journal of Asian Earth Sciences*, 148:96–104.

Ragon, T. and Simons, M. (2021). Accounting for uncertain 3-d elastic structure in fault slip estimates. *Geophysical Journal International*, 224(2):1404–1421.

Rau, R.-J., Wen, Y.-Y., Ching, K.-E., Hsieh, M.-C., Lo, Y.-T., Chiu, C.-Y., and Hashimoto, M. (2022). Origin of coseismic anelastic deformation during the 2016 mw 6.4 meinong earthquake, taiwan. *Tectonophysics*, 836:229428.

Reid, H. F. (1910). The mechanism of the earthquake, the california earthquake of april 18, 1906. *Report of the Research Senatorial Commission, Carnegie Institution, Washington, DC*, 2:16–18.

Reinisch, E. C., Cardiff, M., Akerley, J., Warren, I., and Feigl, K. L. (2019). Spatio–temporal analysis of deformation at san emidio geothermal field, nevada, usa between 1992 and 2010. *Remote Sensing*, 11(16):1935.

Reutebuch, S. E., McGaughey, R. J., Andersen, H.-E., and Carson, W. W. (2003). Accuracy of a high-resolution lidar terrain model under a conifer forest canopy. *Canadian journal of remote sensing*, 29(5):527–535.

Rusu, R. B., Marton, Z. C., Blodow, N., Dolha, M., and Beetz, M. (2008). Towards 3d point cloud based object maps for household environments. *Robotics and Autonomous Systems*, 56(11):927–941.

Samsonov, S. and Tiampo, K. (2006). Analytical optimization of a dinsar and gps dataset for derivation of three-dimensional surface motion. *IEEE Geoscience and Remote Sensing Letters*, 3(1):107–111.

Samsonov, S., Tiampo, K., Rundle, J., and Li, Z. (2007). Application of dinsar-gps optimization for derivation of fine-scale surface motion maps of southern california. *IEEE Transactions on Geoscience and Remote Sensing*, 45(2):512–521.

Samsonov, S. V., Tiampo, K. F., and Rundle, J. B. (2008). Application of dinsar-gps optimization for derivation of three-dimensional surface motion of the southern california region along the san andreas fault. *Computers & Geosciences*, 34(5):503–514.

Sandwell, D., Mellors, R., Tong, X., Wei, M., and Wessel, P. (2011). Open radar interferometry software for mapping surface deformation.

Sauer, S., Ferro-Famil, L., Reigber, A., and Pottier, E. (2011). Three-dimensional imaging and scattering mechanism estimation over urban scenes using dual-baseline polarimetric insar observations at l-band. *IEEE Transactions on Geoscience and Remote Sensing*, 49(11):4616–4629.

Savage, J. (1998). Displacement field for an edge dislocation in a layered half-space. *Journal of Geophysical Research: Solid Earth*, 103(B2):2439–2446.

Scholz, C. H. (2019). *The mechanics of earthquakes and faulting*. Cambridge university press.

Scott, C. (2020). Icp_topo_diff_matlab.

Scott, C., Champenois, J., Klinger, Y., Nissen, E., Maruyama, T., Chiba, T., and Arrowsmith, R. (2019). The 2016 m7 kumamoto, japan, earthquake slip field derived from a joint inversion of differential lidar topography, optical correlation, and insar surface displacements. *Geophysical Research Letters*, 46(12):6341–6351.

Scott, C., Phan, M., Nandigam, V., Crosby, C., and Arrowsmith, J. R. (2021). Measuring change at earth's surface: On-demand vertical and three-dimensional topographic differencing implemented in opentopography. *Geosphere*, 17(4):1318–1332.

Scott, C. P., Arrowsmith, J. R., Nissen, E., Lajoie, L., Maruyama, T., and Chiba, T. (2018). The m7 2016 kumamoto, japan, earthquake: 3-d deformation along the fault and within the damage zone constrained from differential lidar topography. *Journal of Geophysical Research: Solid Earth*, 123(7):6138–6155.

Shen, Z.-K. and Liu, Z. (2020). Integration of gps and insar data for resolving 3-dimensional crustal deformation. *Earth and Space Science*, 7(4):e2019EA001036.

Shirzaei, M. and Walter, T. R. (2011). Estimating the effect of satellite orbital error using wavelet-based robust regression applied to insar deformation data. *IEEE transactions on geoscience and remote sensing*, 49(11):4600–4605.

Silver, P. G., Bock, Y., Agnew, D. C., Henyey, T., Linde, A. T., McEvilly, T. V., Minster, J.-B., Romanowicz, B. A., Sachs, I., Smith, R. B., et al. (1999). A plate boundary observatory. *IRIS Newsl., XVI*, 2(3):7–9.

Simons, M., Fialko, Y., and Rivera, L. (2002). Coseismic deformation from the 1999 m w 7.1 hector mine, california, earthquake as inferred from insar and gps observations. *Bulletin of the Seismological Society of America*, 92(4):1390–1402.

Simons, M. and Rosen, P. (2007). Interferometric synthetic aperture radar geodesy. *Geodesy*, 3:391–446.

Singh, S. J. (1970). Static deformation of a multilayered half-space by internal sources. *Journal of Geophysical Research*, 75(17):3257–3263.

Stein, S. and Liu, M. (2009). Long aftershock sequences within continents and implications for earthquake hazard assessment. *Nature*, 462(7269):87–89.

Steketee, J. (1958). On volterra's dislocations in a semi-infinite elastic medium. *Canadian Journal of Physics*, 36(2):192–205.

Szymanski, E. D., Hetland, E. A., and Figueiredo, P. M. (2024). Imaging left-lateral and reverse near-surface slip of the 2020 m w 5.1 sparta, north carolina, earthquake. *Bulletin of the Seismological Society of America*, 114(4):1870–1883.

Tarantola, A. (2005). *Inverse Problem Theory: and Methods for Model Parameter Estimation*. Society for Industrial and Applied Mathematics.

Tarayre, H. and Massonnet, D. (1996). Atmospheric propagation heterogeneities revealed by ers-1 interferometry. *Geophysical Research Letters*, 23(9):989–992.

Teh, Y. W., Seeger, M., and Jordan, M. I. (2005). Semiparametric latent factor models. In *International Workshop on Artificial Intelligence and Statistics*, pages 333–340. PMLR.

Thomas, M. and Joy, A. T. (2006). *Elements of information theory*. Wiley-Interscience.

Tibshirani, R. (1996). Regression shrinkage and selection via the lasso. *Journal of the Royal Statistical Society*, 58:267–288.

Tibshirani, R., Saunders, M., Rosset, S., Zhu, J., and Knight, K. (2005). Sparsity and smoothness via the fused lasso. *Journal of the Royal Statistical Society: Series B (Statistical Methodology)*, 67(1):91–108.

Tikhonov, A. N., Goncharsky, A. V., Stepanov, V. V., Yagola, A. G., Tikhonov, A., Goncharsky, A., Stepanov, V., and Yagola, A. (1995). *Numerical methods for the approximate solution of ill-posed problems on compact sets*. Springer.

Tong, X., Sandwell, D., and Smith-Konter, B. (2013). High-resolution interseismic velocity data along the san andreas fault from gps and insar. *Journal of Geophysical Research: Solid Earth*, 118(1):369–389.

Torge, W., Müller, J., and Pail, R. (2023). *Geodesy*. De Gruyter Oldenbourg, Berlin, Boston.

Utsu, T., Ogata, Y., et al. (1995). The centenary of the omori formula for a decay law of aftershock activity. *Journal of Physics of the Earth*, 43(1):1–33.

Véga, C., Renaud, J.-P., Durrieu, S., and Bouvier, M. (2016). On the interest of penetration depth, canopy area and volume metrics to improve lidar-based models of forest parameters. *Remote Sensing of Environment*, 175:32–42.

Walbert, O. L. and Hetland, E. A. (2022). Bayesian inference of seismogenic stress for the 2016 m w 7.8 kaikōura, new zealand, earthquake. *Bulletin of the Seismological Society of America*, 112(4):1894–1907.

Wang, H. and Wright, T. (2012). Satellite geodetic imaging reveals internal deformation of western tibet. *Geophysical Research Letters*, 39(7).

Wegener, A. (1912). Die herausbildung der grossformen der erdrinde (kontinente und ozeane), auf geophysikalischer grundlage. *Petermanns Geographische Mitteilungen*, 63:185–195.

Wen, S., Yeh, Y.-L., Chang, Y.-Z., and Chen, C.-H. (2017). The seismogenic process of the 2016 meinong earthquake, southwest taiwan. *Terr. Atmos. Ocean. Sci*, 28:651–662.

Wessel, P., Luis, J. F., Uieda, L. a., Scharroo, R., Wobbe, F., Smith, W. H., and Tian, D. (2019). The generic mapping tools version 6. *Geochemistry, Geophysics, Geosystems*, 20(11):5556–5564.

Wicks, C. W. and Chiu, J.-M. (2022). Surface rupture on a secondary fault associated with the 8 august 2020 mw 5.1 sparta north carolina earthquake. *The Seismic Record*, 2:59–67.

Williams, C. K. and Rasmussen, C. E. (2006). *Gaussian processes for machine learning*, volume 2. MIT press Cambridge, MA.

Xu, B., Li, Z.-w., Wang, Q.-j., Jiang, M., Zhu, J.-j., and Ding, X.-l. (2014). A refined strategy for removing composite errors of sar interferogram. *IEEE Geoscience and Remote Sensing Letters*, 11.

Xu, Z., Li, H.-C., Shi, Q., Wang, H., Wei, M., Shi, J., and Shao, Y. (2019). Effect analysis and spectral weighting optimization of sidelobe reduction on sar image understanding. *IEEE Journal of Selected Topics in Applied Earth Observations and Remote Sensing*, 12(9):3434–3444.

Yi, D.-C., Chuang, R. Y., Chung, L.-H., Lin, C.-W., and Rau, R.-J. (2023). Surface deformation induced by the 2016 meinong earthquake and its implications to active folds. *Terrestrial, Atmospheric and Oceanic Sciences*, 34(1):21.

Yoshioka, S. (2001). Coseismic slip distribution of the 1999 chi-chi, taiwan, earthquake deduced from inversion analysis of gps data. *Bulletin of the Seismological Society of America*, 91(5):1182–1189.